

# Towards an Understanding of the Correlations in Jet Substructure

Report of BOOST2013, hosted by the University of Arizona, 12<sup>th</sup>-16<sup>th</sup> of August 2013.

D. Adams<sup>1</sup>, A. Arce<sup>2</sup>, L. Asquith<sup>3</sup>, M. Backovic<sup>4</sup>, T. Barillari<sup>5</sup>, P. Berta<sup>6</sup>,  
D. Bertolini<sup>2</sup>, A. Buckley<sup>8</sup>, J. Butterworth<sup>9</sup>, R. C. Camacho Toro<sup>10</sup>, J. Caudron<sup>9</sup>,  
Y.-T. Chien<sup>11</sup>, J. Cogan<sup>12</sup>, B. Cooper<sup>9</sup>, D. Curtin<sup>17</sup>, C. Debenedetti<sup>18</sup>, J. Dolen<sup>9</sup>,  
M. Eklund<sup>22</sup>, S. El Hedri<sup>22</sup>, S. D. Ellis<sup>22</sup>, T. Embry<sup>22</sup>, D. Ferencek<sup>23</sup>, J. Ferrando<sup>24</sup>,  
S. Fleischmann<sup>16</sup>, M. Freytsis<sup>25</sup>, M. Giulini<sup>21</sup>, Z. Han<sup>27</sup>, D. Hare<sup>4</sup>, P. Harris<sup>4</sup>,  
A. Hinzmann<sup>4</sup>, R. Hoing<sup>4</sup>, A. Hornig<sup>22</sup>, M. Jankowiak<sup>4</sup>, K. Johns<sup>28</sup>, G. Kasieczka<sup>23</sup>,  
T. Knight<sup>24</sup>, G. Kasieczka<sup>29</sup>, R. Kogler<sup>30</sup>, W. Lampl<sup>4</sup>, A. J. Larkoski<sup>4</sup>,  
C. Lee<sup>31</sup>, R. Leone<sup>31</sup>, P. Loch<sup>31</sup>, D. Lopez Mateos<sup>27</sup>, H. K. Lou<sup>27</sup>, M. Low<sup>27</sup>,  
P. Maksimovic<sup>32</sup>, I. Marchesini<sup>32</sup>, S. Marzani<sup>32</sup>, L. Masetti<sup>33</sup>, R. McCarthy<sup>32</sup>,  
S. Menke<sup>32</sup>, D. W. Miller<sup>35</sup>, K. Mishra<sup>36</sup>, B. Nachman<sup>32</sup>, P. Nef<sup>4</sup>, F. T. O'Grady<sup>24</sup>,  
A. Ovcharova<sup>23</sup>, A. Picazio<sup>37</sup>, C. Pollard<sup>38</sup>, B. Potter Landua<sup>29</sup>, C. Potter<sup>29</sup>,  
S. Rappoccio<sup>39</sup>, J. Rojo<sup>48</sup>, J. Rutherford<sup>40</sup>, G. P. Salam<sup>10,11</sup>, J. Schabinger<sup>23</sup>,  
A. Schwartzman<sup>4</sup>, M. D. Schwartz<sup>27</sup>, B. Shuve<sup>43</sup>, P. Sinervo<sup>44</sup>, D. Soper<sup>45</sup>,  
D. E. Sosa Corral<sup>45</sup>, M. Spannowsky<sup>32</sup>, E. Strauss<sup>34</sup>, M. Swiatkowski<sup>4</sup>, J. Thaler<sup>34</sup>,  
C. Thomas<sup>34</sup>, E. Thompson<sup>1</sup>, N. V. Tran<sup>36</sup>, J. Tseng<sup>36</sup>, E. Usai<sup>36</sup>, L. Valery<sup>36</sup>,  
J. Veatch<sup>23</sup>, M. Vos<sup>23</sup>, W. Waalewijn<sup>4</sup>, and C. Young<sup>47</sup>

<sup>1</sup> Columbia University, Nevis Laboratory, Irvington, NY 10533, USA

<sup>2</sup> Duke University, Durham, NC 27708, USA

<sup>3</sup> Argonne National Laboratory, Lemont, IL 60439, USA

<sup>4</sup> SLAC National Accelerator Laboratory, Menlo Park, CA 94025, USA

<sup>5</sup> Deutsches Elektronen-Synchrotron, DESY, D-15738 Zeuthen, Germany

<sup>6</sup> Cornell University, Ithaca, NY 14853, USA

<sup>7</sup> Lund University, Lund, SE 22100, Sweden

<sup>8</sup> University of Edinburgh, EH9 3JZ, UK

<sup>9</sup> University College London, WC1E 6BT, UK

<sup>10</sup> LPTHE, UPMC Univ. Paris 6 and CNRS UMR 7589, Paris, France

<sup>11</sup> CERN, CH-1211 Geneva 23, Switzerland

<sup>12</sup> CAFPE and U. of Granada, Granada, E-18071, Spain

<sup>13</sup> McGill University, Montreal, Quebec H3A 2T8, Canada

<sup>14</sup> Iowa State University, Ames, Iowa 50011, USA

<sup>15</sup> Rutgers University, Piscataway, NJ 08854, USA

<sup>16</sup> Bergische Universitaet Wuppertal, Wuppertal, D-42097, Germany

<sup>17</sup> YITP, Stony Brook University, Stony Brook, NY 11794-3840, USA

<sup>18</sup> University of Manchester, Manchester, M13 9PL, UK

<sup>19</sup> UNESP - Universidade Estadual Paulista, Sao Paulo, 01140-070, Brazil

<sup>20</sup> INFN and University of Naples, IT80216, Italy

<sup>21</sup> University of Geneva, CH-1211 Geneva 4, Switzerland

<sup>22</sup> University of Washington, Seattle, WA 98195, USA

<sup>23</sup> Instituto de Física Corpuscular, IFIC/CSIC-UVEG, E-46071 Valencia, Spain

<sup>24</sup> University of Glasgow, Glasgow, G12 8QQ, UK

<sup>25</sup> Berkeley National Laboratory, University of California, Berkeley, CA 94720, USA

<sup>26</sup> Universidad de Buenos Aires, AR-1428, Argentina

<sup>27</sup> Harvard University, Cambridge, MA 02138, USA

<sup>28</sup> Weizmann Institute, 76100 Rehovot, Israel

<sup>29</sup> Universitaet Hamburg, DE-22761, Germany

<sup>30</sup> Universitaet Heidelberg, DE-69117, Germany

<sup>31</sup> University of Arizona, Tucson, AZ 85719, USA

<sup>32</sup> IPPP, University of Durham, Durham, DH1 3LE, UK

<sup>33</sup> Universitaet Mainz, DE 55099, Germany

<sup>34</sup> MIT, Cambridge, MA 02139, USA

<sup>35</sup> University of Chicago, IL 60637, USA

<sup>36</sup> Fermi National Accelerator Laboratory, Batavia, IL 60510, USA

<sup>37</sup> Indiana University, Bloomington, IN 47405, USA

<sup>38</sup> University of California, Davis, CA 95616, USA

<sup>39</sup> Johns Hopkins University, Baltimore, MD 21218, USA

<sup>40</sup> INFN and University of Pisa, Pisa, IT-56127, Italy

<sup>41</sup> Texas A & M University, College Station, TX 77843, USA

<sup>42</sup> INFN and University of Calabria, Rende, IT-87036, Italy

<sup>43</sup> Brown University, Richmond, RI 02912, USA

<sup>44</sup> Yale University, New Haven, CT 06511, USA

<sup>45</sup> CEA Saclay, Gif-sur-Yvette, FR-91191, France

<sup>46</sup> University of Illinois, Chicago, IL 60607, USA

<sup>47</sup> University of California, Berkeley, CA 94720, USA

**Abstract** Abstract for BOOST2013 report

**Keywords** boosted objects · jet substructure · beyond-the-Standard-Model physics searches · Large Hadron Collider

## 1 Introduction

The characteristic feature of collisions at the LHC is a center-of-mass energy, 7 TeV in 2010 and 2011, of 8 TeV in 2012, and near 14 TeV with the start of the second phase of operation in 2015, that is large compared to even the heaviest of the known particles. Thus these particles (and also previously unknown ones) will often be produced at the LHC with substantial boosts. As a result, when decaying hadronically, these particles will not be observed as multiple jets in the detector, but rather as a single hadronic jet with distinctive internal substructure. This realization has led to a new era of sophistication in our understanding of both standard QCD jets and jets containing the decay of a heavy particle, with an array of new jet observables and detection techniques introduced and studies. To allow the efficient sharing of results from these jet substructure studies a series of BOOST Workshops have been held on a yearly basis: SLAC (2009, [?]), Oxford University (2010, [?]), Princeton University (2011, [?]), IFIC Valencia (2012 [?]), University of Arizona (2013 [?]), and, most recently, University College London (2014 [?]). After each of these meetings Working Groups have functioned during the following year to generate reports highlighting the most interesting new results, including studies of ever maturing details. Previous BOOST reports can be found at [?,?,?].

The following report from BOOST 2013 thus views the study and implementation of jet substructure techniques as a fairly mature field. The report attempts to focus on the question of the correlations between the plethora of observables that have been developed and employed, and their dependence on the underlying jet parameters, especially the jet radius  $R$  and jet  $p_T$ . The report is organized as follows: NEED TO GENERATE AN OUTLINE OF THE REPORT - ESPECIALLY AS I UNDERSTAND IT MYSELF.

## 2 Monte Carlo Samples and Event Selection

### 2.1 Quark/gluon and $W$ tagging

Samples were generated at  $\sqrt{s} = 8$  TeV for QCD dijets, and for  $W^+W^-$  pairs produced in the decay of

a (pseudo) scalar resonance and decaying hadronically. The QCD events were split into subsamples of  $gg$  and  $q\bar{q}$  events, allowing for tests of discrimination of hadronic  $W$  bosons, quarks, and gluons.

Individual  $gg$  and  $q\bar{q}$  samples were produced at leading order (LO) using MADGRAPH5, while  $W^+W^-$  samples were generated using the JHU GENERATOR to allow for separation of longitudinal and transverse polarizations. Both were generated using CTEQ6L1 PDFs[REF]. The samples were produced in exclusive  $p_T$  bins of width 100 GeV, with the slicing parameter chosen to be the  $p_T$  of any final state parton or  $W$  at LO. At the parton-level the  $p_T$  bins investigated were 300-400 GeV, 500-600 GeV and 1.0-1.1 TeV. Since no matching was performed, a cut on any parton was equivalent. The samples were then all showered through PYTHIA8 (version 8.176) using the default tune 4C.

The showered events were clustered with FASTJET 3.03[REF] using the anti- $k_T$  algorithm[REF] with jet radii of  $R = 0.4, 0.8, 1.2$ . In both signal and background, an upper and lower cut on the leading jet  $p_T$  is applied after showering/clustering, to ensure similar  $p_T$  spectra for signal and background in each  $p_T$  bin. The bins in leading jet  $p_T$  that are investigated in the  $W$ -tagging and  $q/g$  tagging studies are 300-400 GeV, 500-600 GeV, 1.0-1.1 TeV. The distribution of the leading jet  $p_T$  for the  $gg$  and  $WW$  samples in the 300-400 GeV parton  $p_T$  slice prior to the requirement on the leading jet  $p_T$  is shown in Figure 11, for the  $R=0.8$  and  $R=1.2$  anti- $k_T$  jet radii considered in this  $p_T$  slice. Figures 12 and 13 show the equivalent leading jet  $p_T$  distributions for the jet radii considered in the 500-600 GeV and 1.0 - 1.1 TeV slices respectively.

### 2.2 Top tagging

Samples were generated at  $\sqrt{s} = 14$  TeV. Standard Model dijet and top pair samples were produced with SHERPA 2.0.0[REF], with matrix elements of up to two extra partons matched to the shower. The top samples included only hadronic decays and were generated in exclusive  $p_T$  bins of width 100 GeV, taking as slicing parameter the maximum of the top/anti-top  $p_T$ . The QCD samples were generated with a cut on the leading parton-level jet  $p_T$ , where parton-level jets are clustered with the anti- $k_t$  algorithm and jet radii of  $R = 0.4, 0.8, 1.2$ . The matching scale is selected to be  $Q_{\text{cut}} = 40, 60, 80$  GeV for the  $p_{T\text{min}} = 600, 1000$ , and 1500 GeV bins, respectively.

The analysis again relies on FASTJET 3.0.3 for jet clustering and calculation of jet substructure observables, and an upper and lower  $p_T$  cut are applied to each sample to ensure similar  $p_T$  spectra in each bin.

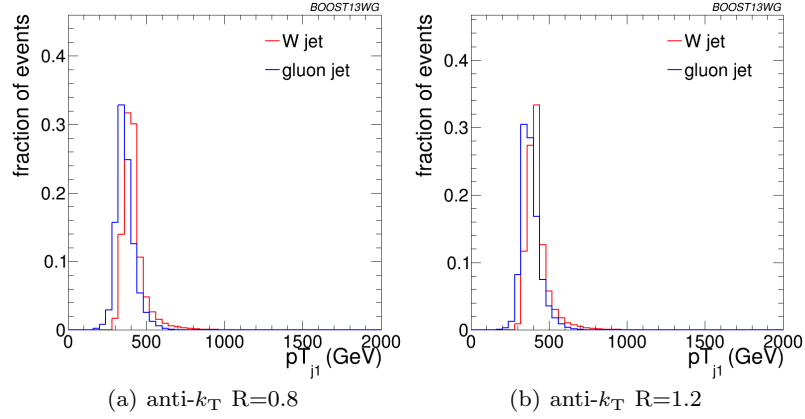


**Fig. 1** Comparisons of the leading jet  $p_T$  spectrum of the  $gg$  background to the  $WW$  signal in the  $p_T$  300-400 GeV parton  $p_T$  slice using the different  $\text{anti-}k_T$  jet distance parameters explored in this  $p_T$  bin. These distributions are formed prior to the 300-400 GeV leading jet  $p_T$  requirement.

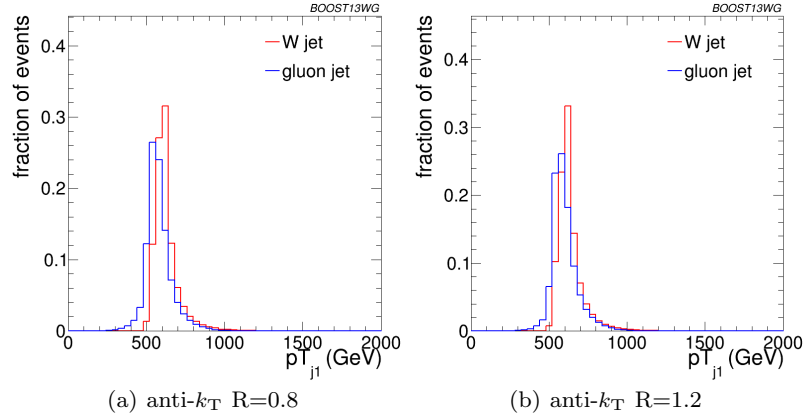


**Fig. 2** Comparisons of the leading jet  $p_T$  spectrum of the  $gg$  background to the  $WW$  signal in the  $p_T$  500-600 GeV parton  $p_T$  slice using the different  $\text{anti-}k_T$  jet distance parameters explored in this  $p_T$  bin. These distributions are formed prior to the 500-600 GeV leading jet  $p_T$  requirement.

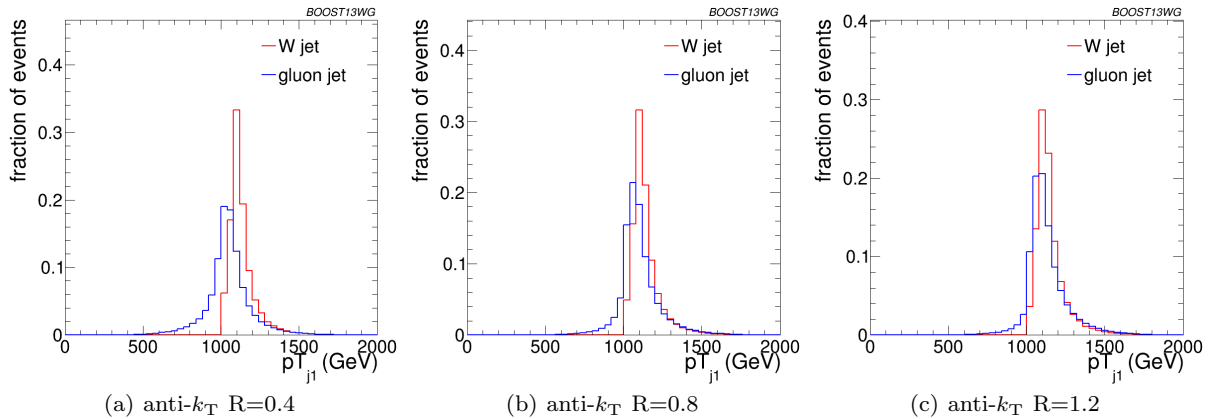


**Fig. 3** Comparisons of the leading jet  $p_T$  spectrum of the  $gg$  background to the  $WW$  signal in the  $p_T$  1.0-1.1 TeV parton  $p_T$  slice using the different  $\text{anti-}k_T$  jet distance parameters explored in this  $p_T$  bin. These distributions are formed prior to the 500-600 GeV leading jet  $p_T$  requirement.

The bins in leading jet  $p_T$  that are investigated for top tagging are 600-700 GeV, 1-1.1 TeV, and 1.5-1.6 TeV. **ED: What jet algorithm is used to define the bins?**

The Qjets method uses statistical analysis of the resulting distributions to extract more information from the jet than can be found in the usual cluster sequence. We use  $\alpha = 0.1$  and 25 trees per event for all the studies presented here.

### 3 Jet Algorithms and Substructure Observables

In this section, we define the jet algorithms and observables used in our analysis. Over the course of our study, we considered a larger set of observables, but for the final analysis, we eliminated redundant observables for presentation purposes. In Sections 3.1, 3.2, 3.3 and 3.4 we first describe the various jet algorithms, groomers, taggers and other substructure variables used in these studies, and then in Section 3.5 list which observables are considered in each section of this report, and the exact settings of the parameters used.

#### 3.1 Jet Clustering Algorithms

**Jet clustering:** Jets were clustered using sequential jet clustering algorithms[REF]. Final state particles  $i, j$  are assigned a mutual distance  $d_{ij}$  and a distance to the beam,  $d_{iB}$ . The particle pair with smallest  $d_{ij}$  are recombined and the algorithm repeated until the smallest distance is instead the distance to the beam,  $d_{iB}$ , in which case  $i$  is set aside and labelled as a jet. The distance metrics are defined as

$$d_{ij} = \min(p_{Ti}^{2\gamma}, p_{Tj}^{2\gamma}) \frac{\Delta R_{ij}^2}{R^2}, \quad (1)$$

$$d_{iB} = p_{Ti}^{2\gamma}, \quad (2)$$

where  $\Delta R_{ij}^2 = (\Delta\eta)^2 + (\Delta\phi)^2$ . In this analysis, we use the anti- $k_t$  algorithm ( $\gamma = -1$ ), the Cambridge/Aachen (C/A) algorithm ( $\gamma = 0$ )[REF], and the  $k_t$  algorithm ( $\gamma = 1$ )[REF], each of which has varying sensitivity to soft radiation in defining the jet.

**Qjets:** We also perform non-deterministic jet clustering[REF]. Instead of always clustering the particle pair with smallest distance  $d_{ij}$ , the pair selected for combination is chosen probabilistically according to a measure

$$P_{ij} \propto e^{-\alpha (d_{ij} - d_{\min})/d_{\min}}, \quad (3)$$

where  $d_{\min}$  is the minimum distance for the usual jet clustering algorithm at a particular step. This leads to a different cluster sequence for the jet each time the Qjet algorithm is used, and consequently different substructure properties. The parameter  $\alpha$  is called the rigidity and is used to control how sharply peaked the probability distribution is around the usual, deterministic value.

#### 3.2 Jet Grooming Algorithms

**Pruning:** Given a jet, re-cluster the constituents using the C/A algorithm. At each step, proceed with the merger as usual unless both

$$\frac{\min(p_{Ti}, p_{Tj})}{p_{Tij}} < z_{\text{cut}} \quad \text{and} \quad \Delta R_{ij} > \frac{2m_j}{p_{Tj}} R_{\text{cut}}, \quad (4)$$

in which case the merger is vetoed and the softer branch discarded. The default parameters used for pruning[REF] in this study are  $z_{\text{cut}} = 0.1$  and  $R_{\text{cut}} = 0.5$ . One advantage of pruning is that the thresholds used to veto soft, wide-angle radiation scale with the jet kinematics, and so the algorithm is expected to perform comparably over a wide range of momenta.

**Trimming:** Given a jet, re-cluster the constituents into subjets of radius  $R_{\text{trim}}$  with the  $k_t$  algorithm. Discard all subjets  $i$  with

$$p_{Ti} < f_{\text{cut}} p_{TJ}. \quad (5)$$

The default parameters used for trimming[REF] in this study are  $R_{\text{trim}} = 0.2$  and  $f_{\text{cut}} = 0.03$ .

**Filtering:[REF]** Given a jet, re-cluster the constituents into subjets of radius  $R_{\text{filt}}$  with the C/A algorithm. Redefine the jet to consist of only the hardest  $N$  subjets, where  $N$  is determined by the final state topology and is typically one more than the number of hard prongs in the resonance decay (to include the leading final-state gluon emission). **ED: Do we actually use filtering as described here anywhere?**

**Soft drop:** Given a jet, re-cluster all of the constituents using the C/A algorithm. Iteratively undo the last stage of the C/A clustering from  $j$  into subjets  $j_1, j_2$ . If

$$\frac{\min(p_{T1}, p_{T2})}{p_{T1} + p_{T2}} < z_{\text{cut}} \left( \frac{\Delta R_{12}}{R} \right)^\beta, \quad (6)$$

discard the softer subjet and repeat. Otherwise, take  $j$  to be the final soft-drop jet[REF]. Soft drop has two input parameters, the angular exponent  $\beta$  and the soft-drop scale  $z_{\text{cut}}$ , with default value  $z_{\text{cut}} = 0.1$ . **ED: Soft-drop actually functions as a tagger when  $\beta = -1$**

### 3.3 Jet Tagging Algorithms

**Modified Mass Drop Tagger:** Given a jet, re-cluster all of the constituents using the C/A algorithm. Iteratively undo the last stage of the C/A clustering from  $j_{214}$  into subjects  $j_1, j_2$  with  $m_{j_1} > m_{j_2}$ . If either

$$m_{j_1} > \mu m_j \text{ or } \frac{\min(p_{T1}^2, p_{T2}^2)}{m_j^2} \Delta R_{12}^2 < y_{\text{cut}}, \quad (7)$$

then discard the branch with the smaller transverse mass  $m_T = \sqrt{m_i^2 + p_{Ti}^2}$ , and re-define  $j$  as the branch with the larger transverse mass. Otherwise, the jet is tagged. If de-clustering continues until only one branch remains, the jet is untagged. In this study we use by default  $\mu = 1.0$  and  $y_{\text{cut}} = 0.1$ .

**Johns Hopkins Tagger:** Re-cluster the jet using the C/A algorithm. The jet is iteratively de-clustered, and at each step the softer prong is discarded if its  $p_T$  is less than  $\delta_p p_{T\text{jet}}$ . This continues until both prongs are harder than the  $p_T$  threshold, both prongs are softer than the  $p_T$  threshold, or if they are too close ( $|\Delta\eta_{ij}| + |\Delta\phi_{ij}| < \delta_R$ ); the jet is rejected if either of the latter conditions apply. If both are harder than the  $p_T$  threshold, the same procedure is applied to each: this results in 2, 3, or 4 subjects. If there exist 3 or 4 subjects, then the jet is accepted: the top candidate is the sum of the subjects, and  $W$  candidate is the pair of subjects closest to the  $W$  mass. The output of the tagger is  $m_t, m_W$  and  $\theta_h$ , a helicity angle defined as the angle, measured in the rest frame of the  $W$  candidate, between the top direction and one of the  $W$  decay products.

**HEPTopTagger:** Re-cluster the jet using the C/A algorithm. The jet is iteratively de-clustered, and at each step the softer prong is discarded if  $m_1/m_{12} > \mu$  (there is not a significant mass drop). Otherwise, both prongs are kept. This continues until a prong has a mass  $m_i < m$ , at which point it is added to the list of subjects. Filter the jet using  $R_{\text{filt}} = \min(0.3, \Delta R_{ij})$ , keeping the five hardest subjects (where  $\Delta R_{ij}$  is the distance between the two hardest subjects). Select the three subjects whose invariant mass is closest to  $m_t$ . The output of the tagger is  $m_t, m_W$ , and  $\theta_h$ , a helicity angle defined as the angle, measured in the rest frame of the  $W$  candidate, between the top direction and one of the  $W$  decay products.

**Top Tagging with Pruning:** For comparison with the other top taggers, we add a  $W$  reconstruction step to the trimming algorithm described above. A  $W$  candidate is found as follows: if there are two subjects, the highest-mass subject is the  $W$  candidate (because the

$W$  prongs end up clustered in the same subject); if there are three subjects, the two subjects with the smallest invariant mass comprise the  $W$  candidate. In the case of only one subject, no  $W$  is reconstructed.

**Top Tagging with Trimming:** For comparison with the other top taggers, we add a  $W$  reconstruction step to the trimming algorithm described above. A  $W$  candidate is found as follows: if there are two subjects, the highest-mass subject is the  $W$  candidate (because the  $W$  prongs end up clustered in the same subject); if there are three subjects, the two subjects with the smallest invariant mass comprise the  $W$  candidate. In the case of only one subject, no  $W$  is reconstructed.

### 3.4 Other Jet Substructure Observables

**Qjet mass volatility:** As described above, Qjet algorithms re-cluster the same jet non-deterministically to obtain a collection of interpretations of the jet. For each jet interpretation, the pruned jet mass is computed with the default pruning parameters. The mass volatility,  $\Gamma_{\text{Qjet}}$ , is defined as

$$\Gamma_{\text{Qjet}} = \frac{\sqrt{\langle m_J^2 \rangle - \langle m_J \rangle^2}}{\langle m_J \rangle}, \quad (8)$$

where averages are computed over the Qjet interpretations.

**$N$ -subjettiness:**  $N$ -subjettiness[REF] quantifies how well the radiation in the jet is aligned along  $N$  directions. To compute  $N$ -subjettiness,  $\tau_N^{(\beta)}$ , one must first identify  $N$  axes within the jet. Then,

$$\tau_N = \frac{1}{d_0} \sum_i p_{Ti} \min(\Delta R_{1i}^\beta, \dots, \Delta R_{Ni}^\beta), \quad (9)$$

where distances are between particles  $i$  in the jet and the axes,

$$d_0 = \sum_i p_{Ti} R^\beta \quad (10)$$

and  $R$  is the jet clustering radius. The exponent  $\beta$  is a free parameter. There is also some choice in how the axes used to compute  $N$ -subjettiness are determined. The optimal configuration of axes is the one that minimizes  $N$ -subjettiness; recently, it was shown that the “winner-takes-all” axes can be easily computed and have superior performance compared to other minimization techniques[REF]. **ED: Do we use WTA? Otherwise why do we mention this?**

A more powerful discriminant is often the ratio,

$$\tau_{N,N-1} \equiv \frac{\tau_N}{\tau_{N-1}}. \quad (11)$$

While this is not an infrared-collinear (IRC) safe observable, it is calculable[REF] and can be made IRC safe with a loose lower cut on  $\tau_{N-1}$ .

**Energy correlation functions:** The transverse momentum version of the energy correlation functions are defined as[REF]:

$$\text{ECF}(N, \beta) = \sum_{i_1 < i_2 < \dots < i_N \in j} \left( \prod_{a=1}^N p_{Ti_a} \right) \left( \prod_{b=1}^{N-1} \prod_{c=b+1}^N \Delta R_{i_b i_c} \right)^\beta \quad (12)$$

where  $i$  is a particle inside the jet. It is preferable to work in terms of dimensionless quantities, particularly the energy correlation function double ratio:

$$C_N^{(\beta)} = \frac{\text{ECF}(N+1, \beta) \text{ECF}(N-1, \beta)}{\text{ECF}(N, \beta)^2}. \quad (13)$$

This observable measures higher-order radiation from leading-order substructure.

### 3.5 Observables for Each Analysis

#### Quark/gluon discrimination:

- The ungroomed jet mass,  $m$ .
- 1-subjettiness,  $\tau_1^\beta$  with  $\beta = 1, 2$ . The  $N$ -subjettiness axes are computed using one-pass  $k_t$  axis optimization.
- 1-point energy correlation functions,  $C_1^{(\beta)}$  with  $\beta = 1, 2$ .
- The pruned Qjet mass volatility,  $\Gamma_{\text{Qjet}}$ .
- The number of constituents ( $N_{\text{constits}}$ ).

#### W vs. gluon discrimination:

- The ungroomed, trimmed ( $m_{\text{trim}}$ ), and pruned ( $m_{\text{pruned}}$ ) jet masses.
- The mass output from the modified mass drop tagger ( $m_{\text{mmdt}}$ ).
- The soft drop mass with  $\beta = -1, 2$  ( $m_{\text{sd}}$ ).
- 2-point energy correlation function ratio  $C_2^{(\beta=1)}$  (we also studied  $\beta = 2$  but did not show its results because it showed poor discrimination power).
- $N$ -subjettiness ratio  $\tau_2/\tau_1$  with  $\beta = 1$  and with axes computed using one-pass  $k_t$  axis optimization (we also studied  $\beta = 2$  but did not show its results because it showed poor discrimination power).
- The pruned Qjet mass volatility.

#### Top vs. QCD discrimination:

- The ungroomed jet mass.
- The HEPTopTagger and the Johns Hopkins tagger.

- Trimming and grooming supplemented with W candidate identification.
- $N$ -subjettiness ratios  $\tau_2/\tau_1$  and  $\tau_3/\tau_2$  with  $\beta = 1$  and the “winner-takes-all” axes.
- 2-point energy correlation function ratios  $C_2^{\beta=1}$  and  $C_3^{\beta=1}$ .
- The pruned Qjet mass volatility.

### Multivariate Analysis Techniques

Multivariate techniques are used to combine variables into an optimal discriminant. In all cases variables are combined using a boosted decision tree (BDT) as implemented in the TMVA package [?]. We use the BDT implementation including gradient boost. An example of the BDT settings are as follows:

- NTrees=1000
- BoostType=Grad
- Shrinkage=0.1
- UseBaggedGrad=F
- nCuts=10000
- MaxDepth=3
- UseYesNoLeaf=F
- nEventsMin=200

Exact parameter values are chosen to best reduce the effect of overtraining.

### 5 Quark-Gluon Discrimination

In this section, we examine the differences between quark- and gluon-initiated jets in terms of substructure variables, and to determine to what extent these variables are correlated. Along the way, we provide some theoretical understanding of these observations. The motivation for these studies comes not only from the desire to “tag” a jet as originating from a quark or gluon, but also to improve our understanding of the quark and gluon components of the QCD background relative to boosted resonances. While recent studies have suggested that quark/gluon tagging efficiencies depend highly on the Monte Carlo generator used, we are more interested in understanding the scaling performance with  $p_T$  and  $R$ , and the correlations between observables, which are expected to be treated consistently within a single shower scheme. (*BS: How about this?*)

#### 5.1 Methodology

These studies use the  $qq$  and  $gg$  samples, described previously in Section 2. Jets are reconstructed using the

anti- $k_T$  algorithm with radius parameters of 0.4, 0.8 and 1.2, and have various jet grooming approaches applied as described in Section 3.4. Only leading and subleading jets in each sample are used.

Figure 4 shows a comparison of the  $p_T$  and  $\eta$  distributions of the quark and gluon samples with  $p_T = 500 - 600$  GeV. The differences in the  $p_T$  distributions can be attributed to different out-of-cone radiation patterns for quark and gluons (*BS: Is this just due to an increased likelihood of hard ISR/FSR for  $gg$  states due to the larger QCD charge?*), while the different  $\eta$  distributions are related to the different parton distribution functions initiating  $qq$  and  $gg$  production. The qualitative features of the  $\eta$  distributions do not change as the  $R$  parameter is changed. As the  $p_T$  increases, the  $\eta$  distributions peak more strongly near zero, as expected. Differences in the  $p_T$  distributions between the leading and sub-leading (and quark and gluon-induced) jets become smaller as the  $R$  parameter is increased, as expected from the physics behind these differences, outlined above.

## 5.2 Single Variable Discrimination

*(BS: Do we want to organize this section similar to for top tagging, where we first discuss the performance of each observable at fixed  $R/p_T$ , and then discuss the variations? It's a little mixed right now.)*

Figure 5 shows the mass of jets in the quark and gluon samples when using different groomers, and Figure 6 shows similar comparisons for different substructure variables. Jets built with the anti- $k_T$  algorithm with  $R=0.8$  and with  $p_T = 500 - 650$  GeV are used. Qualitatively, the application of grooming shifts the mass distributions towards lower values as expected. No clear gain in discrimination can be seen, and for certain grooming parameters, such as the use of soft drop with  $\beta = -1$  a clear loss in discrimination power is observed; this is because the soft-drop condition for  $\beta = -1$  discards collinear radiation, and the differences between quarks and gluons are manifest in the collinear structure (spin, splitting functions, etc.). Few variations are observed as the radius parameter of the jet reconstruction is increased in the two highest  $p_T$  bins. However, for the  $300 - 400$  GeV bin, the use of small- $R$  jets produces a shift in the mass distributions towards lower values, so that large- $R$  jet masses are more stable with  $p_T$  and small- $R$  jet masses are smaller at low- $p_T$  as expected from the spatial constraints imposed by the  $R$  parameter. These statements are explored more quantitatively later in this section.

Among the different substructure variables explored,  $n_{\text{constituents}}$  provides the highest separation power, followed

by  $C_1^{\beta=0}$  and  $C_1^{\beta=1}$  as was also found by the CMS and ATLAS Collaborations [add citations]. The evolution of some of these distributions with  $p_T$  and  $R$  is less trivial than for the jet masses. In particular, changing the  $R$  parameter at high  $p_T$  changes significantly the  $C_a^\beta$  for  $\beta > 0$  and the  $n_{\text{constituents}}$  distributions, while leaving all other distributions qualitatively unchanged. This is illustrated in Figure 7 for  $\beta = 0$  and  $\beta = 1$  using  $a = 1$  in both cases for jets with  $p_T = 1 - 1.2$  TeV. The shift towards lower values with changing  $R$  is evident for the  $C_1^{\beta=1}$  distributions, while the stability of  $C_1^{\beta=0}$  can also be observed. These features are present in all  $p_T$  bins studied, but are even more pronounced for lower  $p_T$  bins. The shape of the Q-jet volatility distribution shows some non-trivial shape that deserves some explanation. Two peaks are observed, one at low volatility values and one at mid-volatility. These peaks are generated by two somewhat distinct populations. The high volatility peak arises from jets that get their mass primarily from soft (and sometimes wide-angle) emissions. The removal of some of the constituents when building Q-jets thus changes the mass significantly, increasing the volatility. The lower volatility peak corresponds to jets for which mass is generated by a hard emission, which makes the fraction of Q-jets that change the mass significantly to be smaller. Since the probability of a hard emission is proportional to the color charge (squared), the volatility peak is higher for gluon jets by about the color factor  $C_A/C_F$ .

To more quantitatively study the power of each observable as a discriminator for quark/gluon tagging, Receiver Operating Characteristic (ROC) curves are built by scanning each distribution and plotting the background efficiency (to select gluon jets) vs. the signal efficiency (to select quark jets). Figure 8 shows these ROC curves for all of the variables shown in Figure 6 and the ungroomed mass, representing the best performing mass variable, for jets of  $p_T = 300 - 400$  GeV. In addition, the ROC curve for the tagger built from a BDT combining all the variables. The details of how the BDT is constructed are explained in Section 4.

Clearly,  $n_{\text{constituents}}$  is the best performing variable for all  $R$ s, even though  $C_1^{\beta=0}$  is close, particularly for  $R=0.8$ . Most other variables have similar performance, except the Q-jet volatility, which shows significantly worse discrimination (this may be due to our choice of rigidity  $\alpha = 0.1$ , while other studies suggest that a smaller value, such as  $\alpha = 0.01$ , produces better results). The combination of all variables shows somewhat better discrimination. The overall discriminating power decreases with increasing  $R$  (*BS: Do we understand if this is due to increased contamination from UE, or if this is an actual physical effect?*), and the features discussed for this

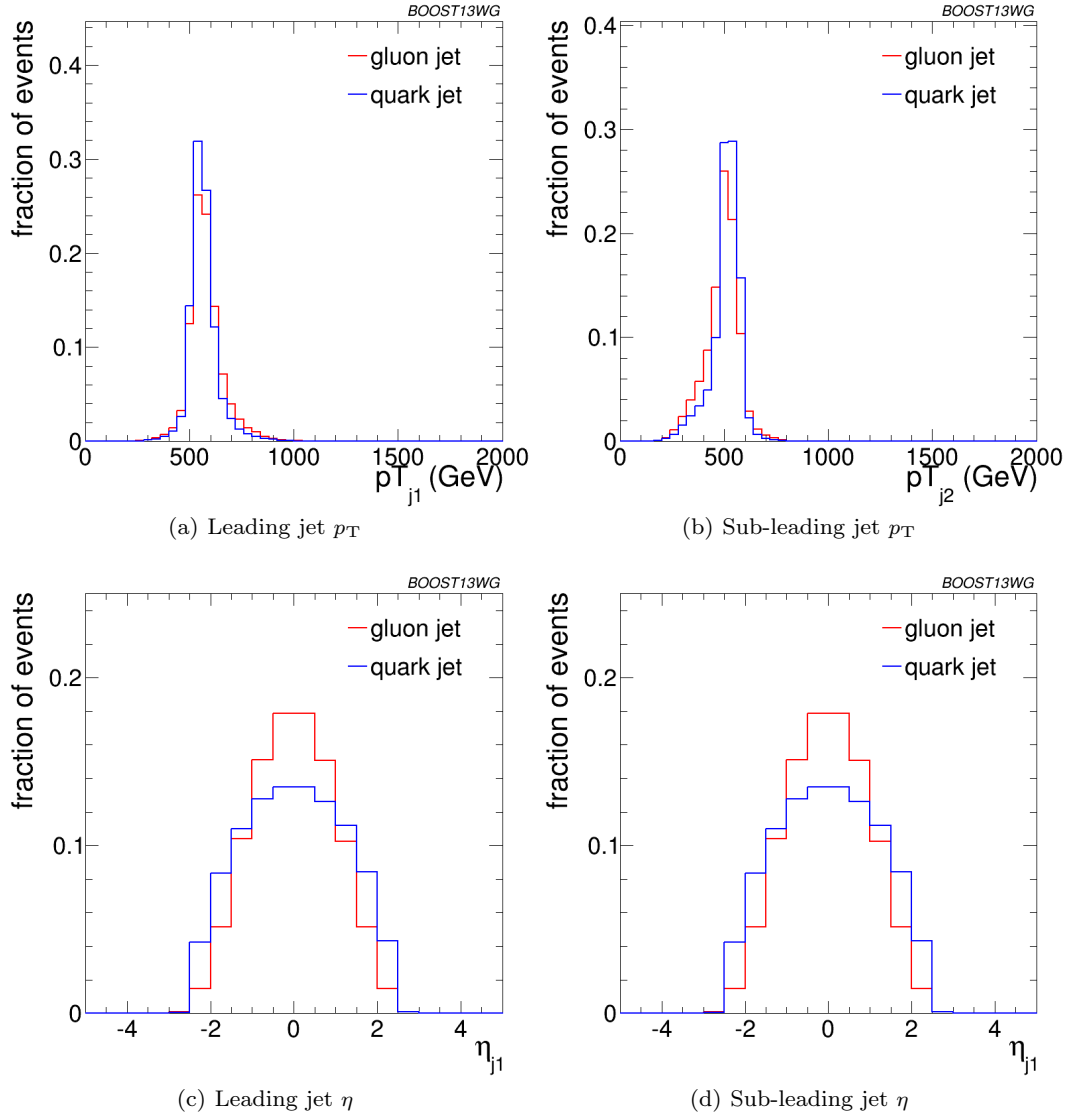


**Fig. 4** Comparisons of quark and gluon  $p_T$  and  $\eta$  distributions in the sample used for the jets of  $p_T = 500 - 600$  GeV bin using the anti- $k_T$   $R=0.8$  algorithm.

$p_T$  bin also apply to the higher  $p_T$  bins. This statement is quantified in the next section.

### 5.3 Correlations and Combined Performance

The combined performance displayed in Fig. 8 is not much better than that of single variables. However, that improvement in performance can be critical for certain analyses requiring a quark/gluon tagger, and potentially larger in data than in Monte Carlo simulation. Furthermore, insight can be gained into the features allowing for quark/gluon discrimination if how that improvement arises is understood. It is therefore worthwhile investigating quantitatively the improvements in per-

formance: to do so, quark/gluon taggers are built from every pair-wise combination of variables studied in the previous section, as well as the full set of variables using a boosted decision tree.

In order to quantitatively study the value of each variable for quark/gluon tagging, the gluon rejection, defined as  $1/\epsilon_{\text{gluon}}$ , is studied at a fixed quark selection efficiency of 50%. Figure 9 shows the rejection for each individual variable (along the diagonal of the plots) and for each pair-wise combination. The rejection for the BDT combining all variables is also shown on the bottom right of each plot. Results are shown for jets with  $p_T = 1 - 1.2$  TeV and for different  $R$  parameters. As already observed in the previous section,  $n_{\text{constits}}$  is the



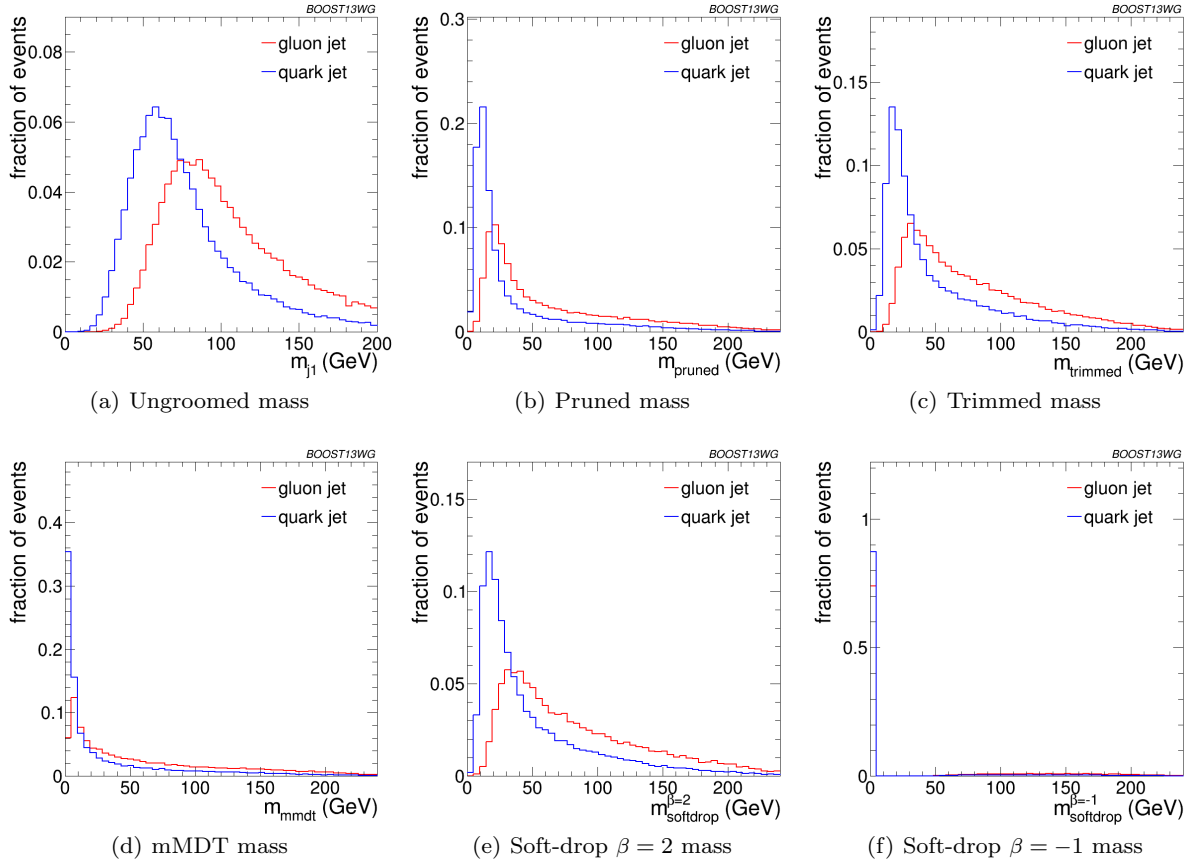


**Fig. 5** Comparisons of ungroomed and groomed quark and gluon mass distributions for leading jets in the  $p_T = 500 - 650$  GeV bin using the anti- $k_T$   $R=0.8$  algorithm.

most powerful single variable and  $C_1^{(\beta=0)}$  follows closely. The combination of the two variables is also one of the most powerful combinations for the two large- $R$  collections. Performance is generally better at small  $R$ , and in this case other pair-wise combinations are more powerful. In particular, the combinations of  $\tau_1^{\beta=1}$  or  $C_1^{(\beta=1)}$  with  $n_{\text{constits}}$  are capable of getting very close to the rejection achievable through the use of all variables.

The overall loss in performance with increasing  $R$  can be observed in all single variables studied, except for  $C_1^{(\beta=0)}$  and the Q-jet volatility, which are quite resilient to increasing  $R$ . This is expected, since their distributions were observed to be also quite insensitive to  $R$  in the previous section. Their combination, however, does lose performance significantly as  $R$  is increased. [do we understand this?] Of all the variables studied,  $\beta = 2$  1-subjettiness and energy correlation variables are particularly sensitive to increasing  $R$ . This is understandable, because for  $\beta = 2$  a larger weight is put in large-angle emissions. However, from other variables, it is understood that most of the discrimination

power comes from analyzing a small- $R$  jet, or the center of the large- $R$  jet.

These observations are qualitatively similar across all ranges of  $p_T$ . Quantitatively, however, there is a loss of rejection power for the taggers made of a combination of variables as the  $p_T$  decreases. This can be observed in Fig. 10 for anti- $k_T$   $R=0.4$  jets of different  $p_T$ s. Clearly, most single variables retain their gluon rejection potential at lower  $p_T$ s. However, when combined with other variables, the highest performing pairwise combinations lose ground with respect to other pairwise combinations. This is also reflected in the rejection of the tagger that uses a combination of all variables, which is lower at lower  $p_T$ s. [do we understand this?]

(BS: Do we want to explicitly mention some aspects of the correlation, namely quantifying which observables seem to be most correlated and that it seems that the all-variable performance is not much better than some of the pair-wise combinations, and so there seem to be  $\sim 2$  independent observables? Also, I remember Nhan had some tables that showed some variable rankings in

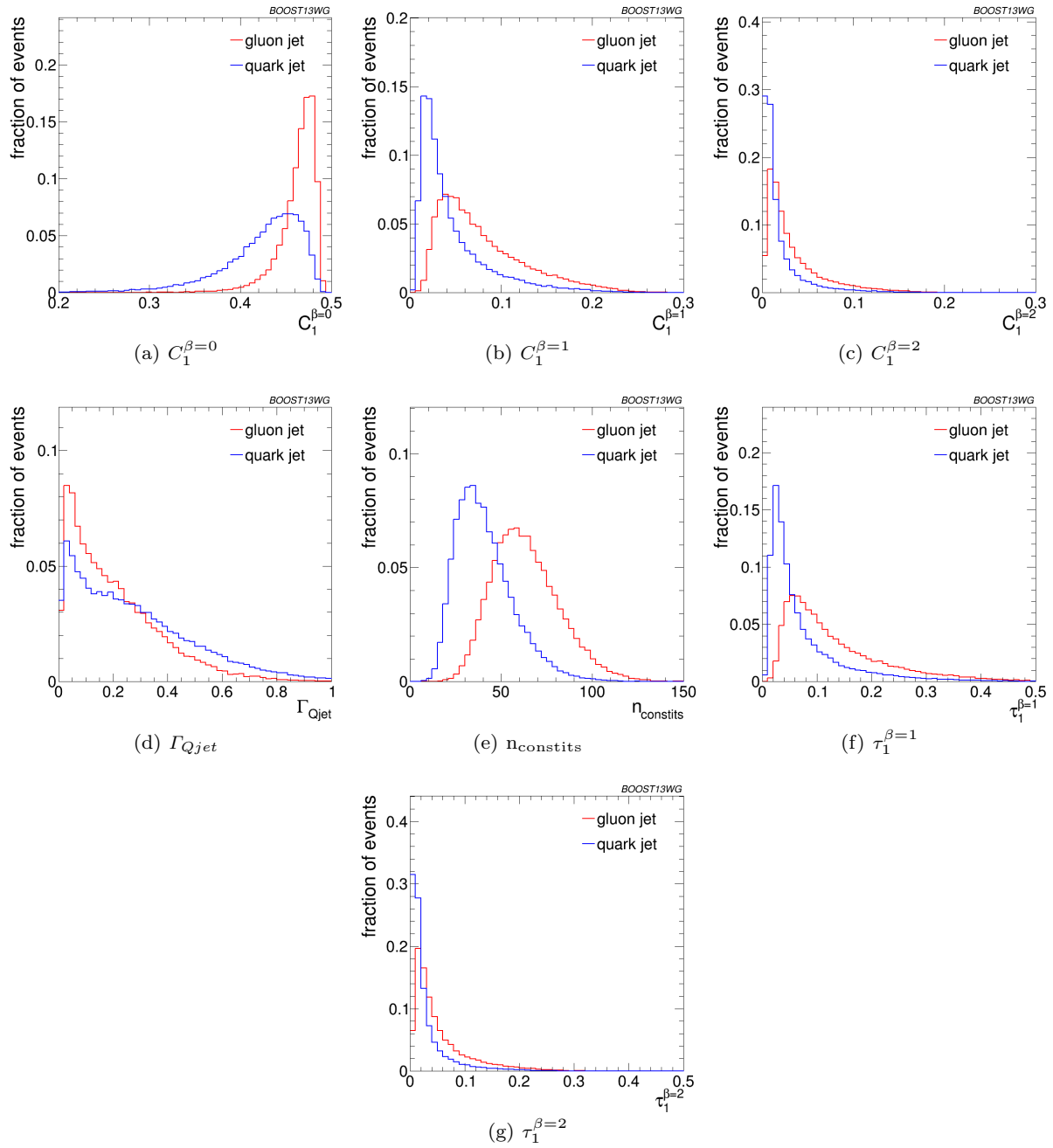


**Fig. 6** Comparisons of quark and gluon distributions of different substructure variables for leading jets in the  $p_T = 500 - 650$  GeV bin using the anti- $k_T$   $R=0.8$  algorithm.

486 terms of how (un)correlated they were; not sure if we  
 487 want to show these.

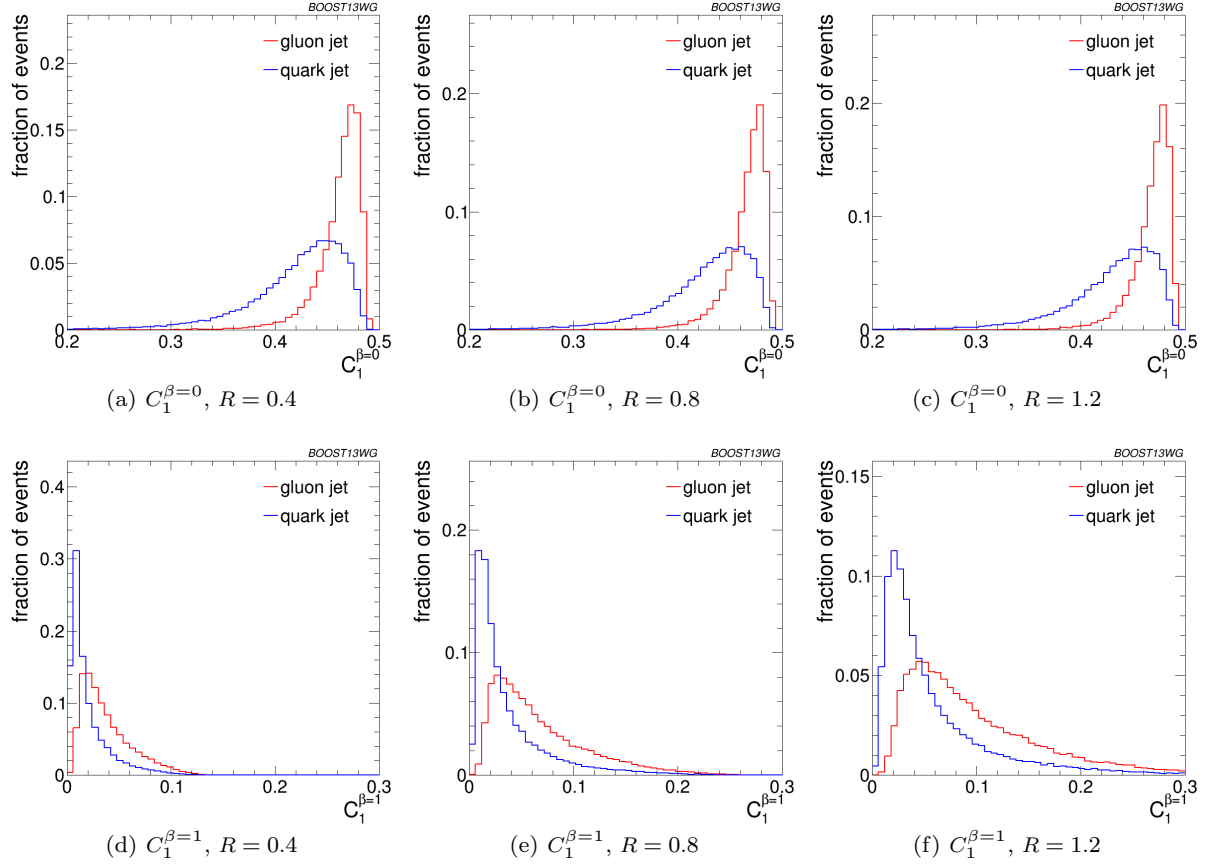


**Fig. 7** Comparisons of quark and gluon distributions of  $C_1^{\beta=0}$  (top) and  $C_1^{\beta=1}$  (bottom) for leading jets in the  $p_T = 1 - 1.2$  TeV bin using the anti- $k_T$  algorithm with  $R=0.4, 0.8$  and  $1.2$ .

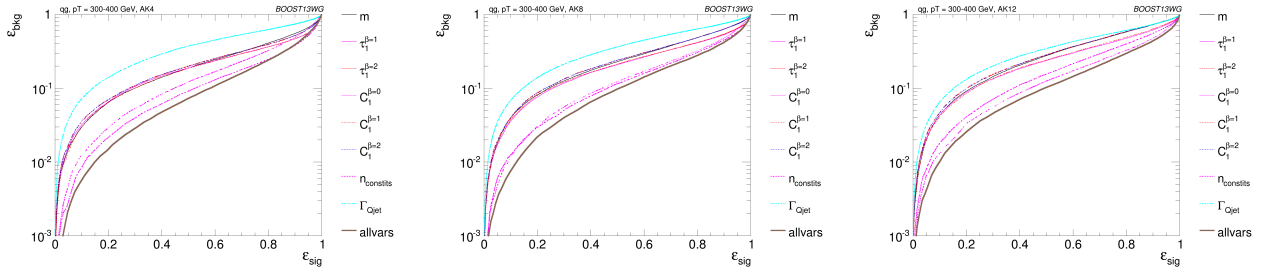


**Fig. 8** The ROC curve for all single variables considered for quark-gluon discrimination in the  $p_T = 500$  GeV bin using the anti- $k_T$   $R=0.8$  algorithm.

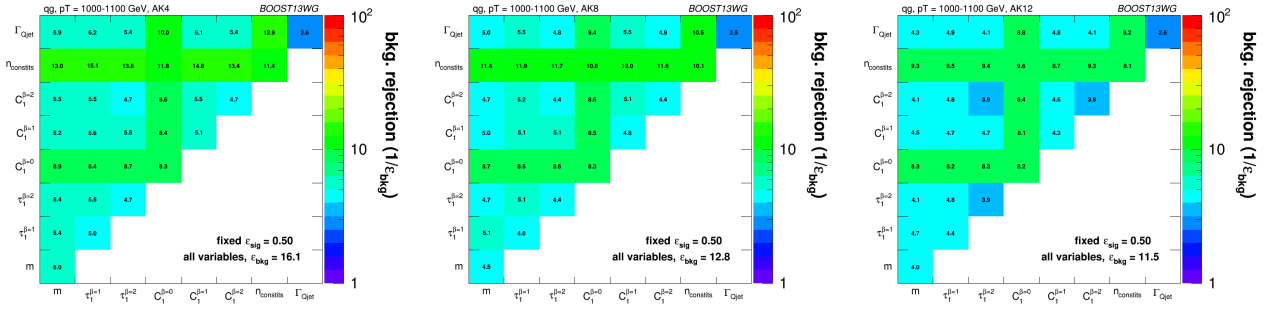


**Fig. 9** Gluon rejection defined as  $1/\epsilon_{\text{gluon}}$  when using each 2-variable combination as a tagger with 50% acceptance for quark jets. Results are shown for jets with  $p_T = 1 - 1.2$  TeV and for different  $R$  parameters. The rejection obtained with a tagger that uses all variables is also shown in the plots.

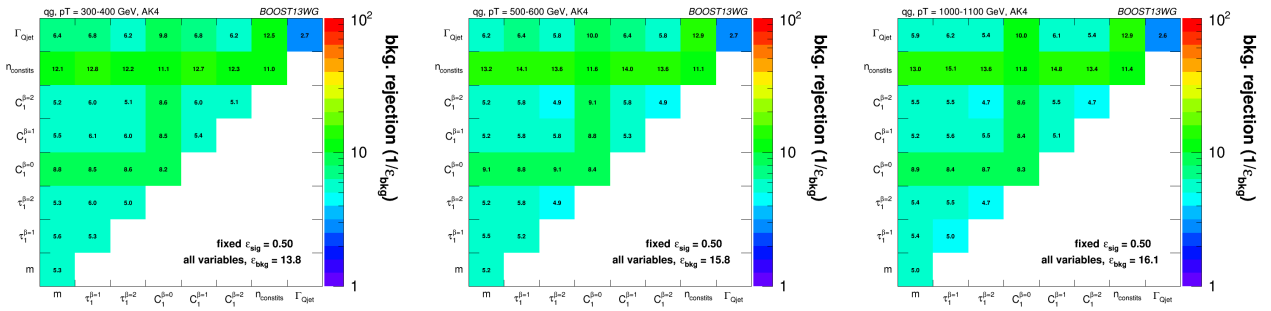


**Fig. 10** Gluon rejection defined as  $1/\epsilon_{\text{gluon}}$  when using each 2-variable combination as a tagger with 50% acceptance for quark jets. Results are shown for  $R=0.4$  jets with  $p_T = 300 - 400$  GeV,  $p_T = 500 - 600$  GeV and  $p_T = 1 - 1.2$  TeV. The rejection obtained with a tagger that uses all variables is also shown in the plots.

## 6 Boosted $W$ -Tagging

algorithm are explored, as well as a variety of kinematic regimes (lead jet  $p_T$  300-400 GeV, 500-600 GeV, 1.0-1.1 TeV). This allows us to determine the performance of observables as a function of jet radius and jet boost, and to see where different approaches may break down. The groomed mass and substructure variables are then combined in a BDT as described in Section 4, and the performance of the resulting BDT discriminant explored through ROC curves to understand the degree to which variables are correlated, and how this changes with jet boost and jet radius.

### 6.1 Methodology

These studies use the  $X \rightarrow WW$  samples as signal and the dijet  $gg$  samples to model the QCD background, described previously in Section 2. Whilst only gluonic backgrounds are explored here, the conclusions as to the dependence of the performance and correlations on the jet boost and radius have been verified to hold also for  $qq$  backgrounds. **ED: To be checked!**

Jets are reconstructed using the anti- $k_T$  algorithm, and have various jet grooming approaches applied as described in Section 3.4. The following event selection is then applied to these samples...(presumably this will vary depending on which kinematic bin is used, as will the actual samples used - maybe summarize in a table).

Figure 11 shows a comparison of the leading jet  $p_T$  for the signal and background in the  $p_T$  300-400 GeV bin, for the two different anti- $k_T$  jet algorithm distance parameters explored in this bin ( $R=0.8$  and  $R=1.2$ ). Figures 12 and 13 show the same for the  $p_T = 500$ -600 GeV bin and  $p_T = 1.0$ -1.1 TeV bin respectively, where for the  $p_T = 1.0$ -1.1 TeV bin the distance parameter  $R=0.4$  is also explored because the  $W$  radiation at this boost is typically confined to a cone of this size.

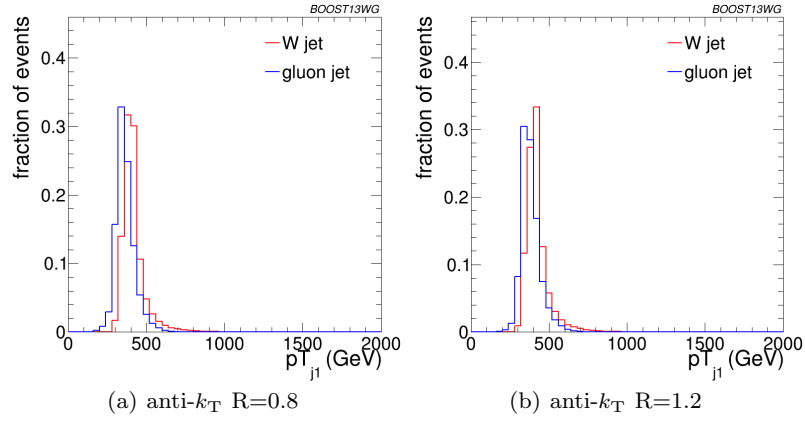
**(ED: Do we need to show the  $p_T$  spectra? Since we end up cutting in a narrow bin, it hopefully shouldn't make a difference.)**

### 6.2 Single Variable Performance

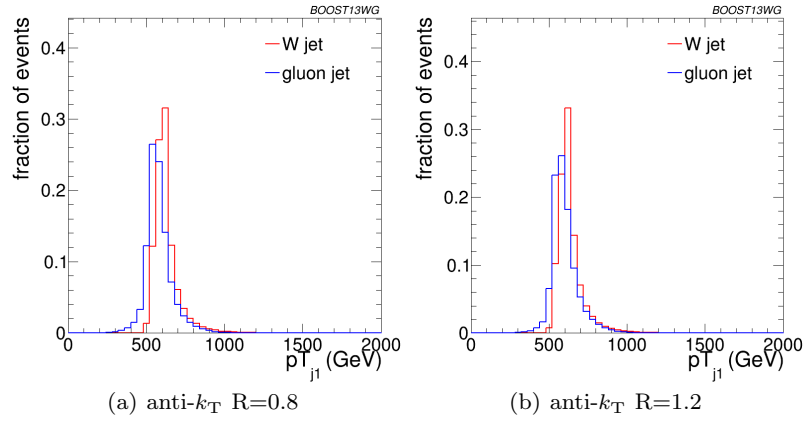
In this section we will explore the performance of the various groomed jet mass and substructure variables in terms of discriminating signal and background, and how this performance changes depending on the kinematic bin and jet radius considered.

Figure 14 compares the signal and background in terms of the different groomed masses explored for the anti- $k_T$   $R=0.8$  algorithm in the  $p_T$  500-600 bin. One can clearly see that in terms of separating signal and background the groomed masses will be significantly

In this section, we study the discrimination of a boosted hadronically decaying  $W$  signal against a gluon background, comparing the performance of various groomed jet masses, substructure variables, and BDT combinations of groomed mass and substructure. We produce ROC curves that elucidate the performance of the various groomed mass and substructure variables. A range of different distance parameters  $R$  for the anti- $k_T$  jet



**Fig. 11** Comparisons of the leading jet  $p_T$  spectrum of the  $gg$  background to the  $WW$  signal in the  $p_T$  300-400 GeV bin using the different  $\text{anti-}k_T$  jet distance parameters explored.



**Fig. 12** Comparisons of the leading jet  $p_T$  spectrum of the  $gg$  background to the  $WW$  signal in the  $p_T$  500-600 GeV bin using the different  $\text{anti-}k_T$  jet distance parameters explored.

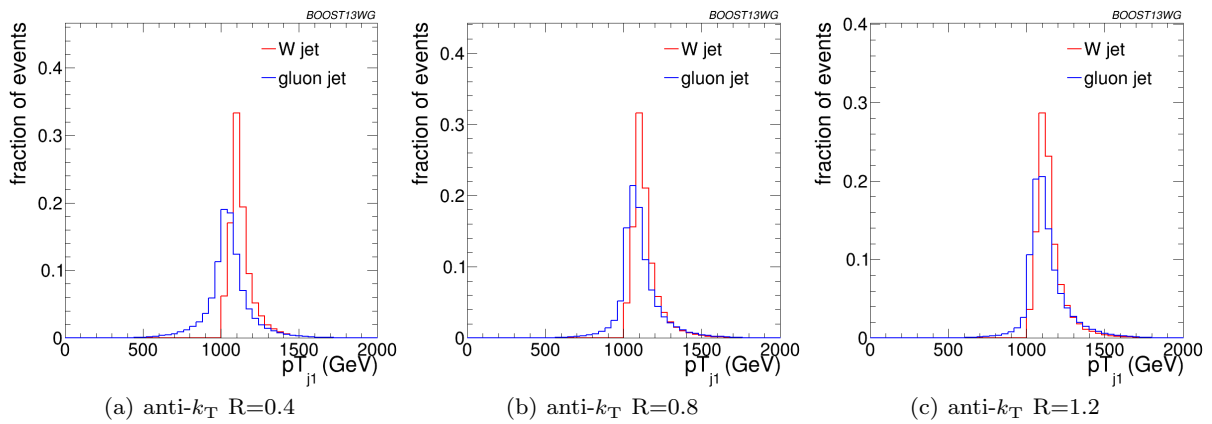


**Fig. 13** Comparisons of the leading jet  $p_T$  spectrum of the  $gg$  background to the  $WW$  signal in the  $p_T$  1.0-1.1 TeV bin using the different  $\text{anti-}k_T$  jet distance parameters explored.

more performant than the ungroomed anti- $k_T$   $R=0.8$  mass. Figure 15 compares signal and background in the different substructure variables explored for the same jet radius and kinematic bin.

Figures 16, 17 and 18 show the single variable ROC curves compared to the ROC curve for a BDT combination of all the variables (labelled “allvars”), for each of the anti- $k_T$  distance parameters considered in each of the kinematic bins. One can see that, in all cases, the “allvars” option is considerably better performant than any of the individual single variables considered, indicating that there is considerable complementarity between the variables, and this will be explored further in the next section.

Although the ROC curves give all the relevant information, it is hard to compare performance quantitatively. In Figures 19, 20 and 21 are shown matrices which give the background rejection for a signal efficiency of 70% when two variables (that on the x-axis and that on the y-axis) are combined in a BDT. These are shown separately for each  $p_T$  bin and jet radius considered. The diagonal of these plots correspond to the background rejections for a single variable BDT, and can thus be examined to get a quantitative measure of the individual single variable performance, and to study how this changes with jet radius and momenta.

One can see that in general the most performant single variables are the groomed masses. However, in certain kinematic bins and for certain jet radii,  $C_2^{\beta=1}$  has a background rejection that is comparable to or better than the groomed masses.

By comparing Figures 19(a), 20(a) and 21(b), we can see how the background rejection performance evolves as we increase momenta whilst keeping the jet radius fixed to  $R=0.8$ . Similarly, by comparing Figures 19(b), 20(b) and 21(c) we can see how performance evolves with  $p_T$  for  $R=1.2$ . For both  $R=0.8$  and  $R=1.2$  the background rejection power of the groomed masses increases with increasing  $p_T$ , with a factor 1.5-2.5 increase in rejection in going from the 300-400 GeV to 1.0-1.1 TeV bins. **ED: Add some of the 1-D plots comparing signal and bkgd in the different masses and  $p_T$  bins here?** However, the  $C_2^{\beta=1}$ ,  $\Gamma_{Qjet}$  and  $\tau_{21}^{\beta=1}$  substructure variables behave somewhat differently. The background rejection power of the  $\Gamma_{Qjet}$  and  $\tau_{21}^{\beta=1}$  variables both decrease with increasing  $p_T$ , by up to a factor two in going from the 300-400 GeV to 1.0-1.1 TeV bins. Conversely the rejection power of  $C_2^{\beta=1}$  dramatically increases with increasing  $p_T$  for  $R=0.8$ , but does not improve with  $p_T$  for the larger jet radius  $R=1.2$ . **ED: Can we explain this? Again, should we add some of the 1-D plots?**

By comparing the individual sub-figures of Figures 19, 20 and 21 we can see how the background rejection performance depends on jet radius within the same  $p_T$  bin. To within  $\sim 25\%$ , the background rejection power of the groomed masses remains constant with respect to the jet radius. However, we again see rather different behaviour for the substructure variables. In all  $p_T$  bins considered the most performant substructure variable,  $C_2^{\beta=1}$ , performs best for an anti- $k_T$  distance parameter of  $R=0.8$ . The performance of this variable is dramatically worse for the larger jet radius of  $R=1.2$  (a factor seven worse background rejection in the 1.0-1.1 TeV bin), and substantially worse for  $R=0.4$ . For the other jet substructure variables considered,  $\Gamma_{Qjet}$  and  $\tau_{21}^{\beta=1}$ , their background rejection power also reduces for larger jet radius, but not to the same extent. **ED: Insert some nice discussion/explanation of why jet substructure power generally gets worse as we go to large jet radius, but groomed mass performance does not. Probably need the 1-D figures for this.**

### 6.3 Combined Performance

The off-diagonal entries in Figures 19, 20 and 21 can be used to compare the performance of different BDT two-variable combinations, and see how this varies as a function of  $p_T$  and  $R$ . By comparing the background rejection achieved for the two-variable combinations to the background rejection of the “all variables” BDT, one can understand how much more discrimination is possible by adding further variables to the two-variable BDTs.

One can see that in general the most powerful two-variable combinations involve a groomed mass and a non-mass substructure variable ( $C_2^{\beta=1}$ ,  $\Gamma_{Qjet}$  or  $\tau_{21}^{\beta=1}$ ). Two-variable combinations of the substructure variables are not powerful in comparison. Which particular mass + substructure variable combination is the most powerful depends strongly on the  $p_T$  and  $R$  of the jet, as discussed in the sections that follow.

There is also modest improvement in the background rejection when different groomed masses are combined, compared to the single variable groomed mass performance, indicating that there is complementary information between the different groomed masses. In addition, there is an improvement in the background rejection when the groomed masses are combined with the ungroomed mass, indicating that grooming removes some useful discriminatory information from the jet. These observations are explored further in the section below.

Generally one can see that the  $R=0.8$  jets offer the best two-variable combined performance in all  $p_T$  bins

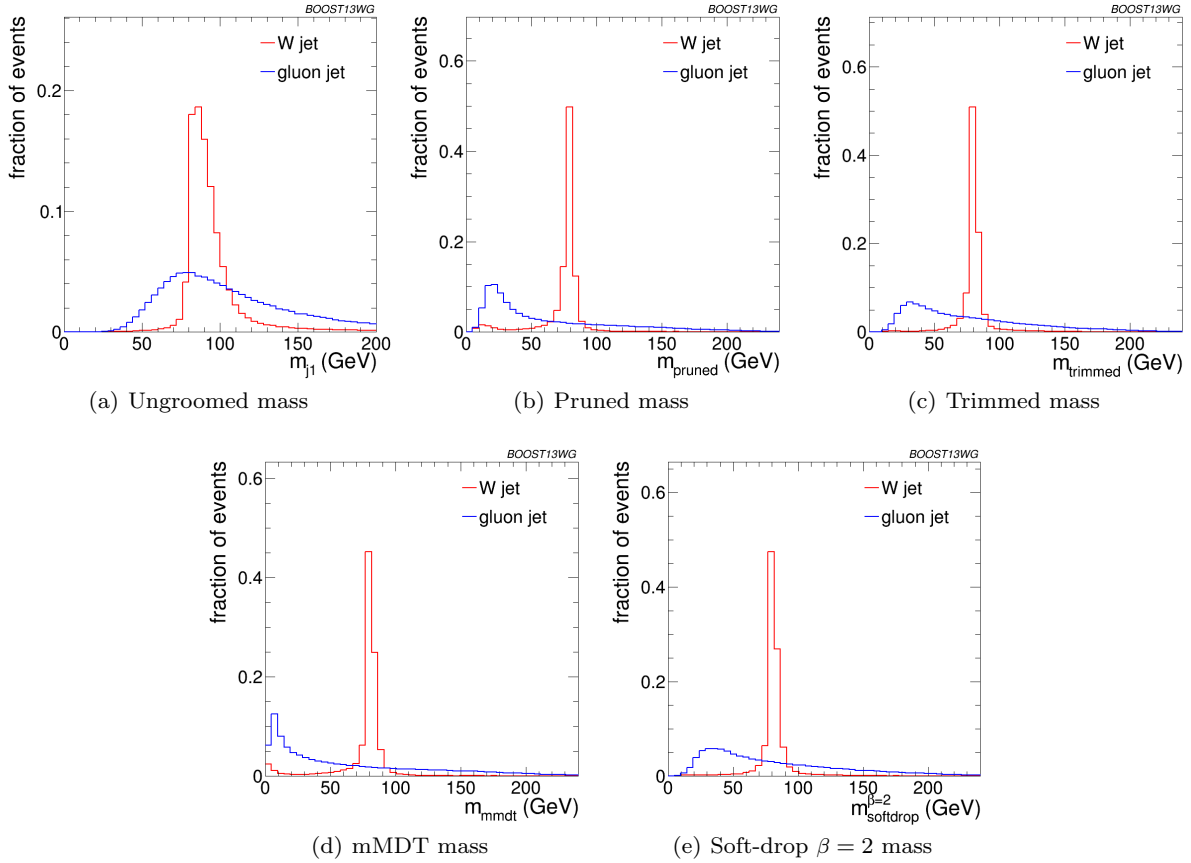


**Fig. 14** Comparisons of the QCD background to the WW signal in the  $p_T$  500-600 GeV bin using the anti- $k_T$   $R=0.8$  algorithm: leading jet mass distributions.

explored here. This is despite the fact that in the high- $p_T$  bin the average separation of the quarks from the W decay is much smaller than 0.8 and well within 0.4. This conclusion could of course be susceptible to pile-up, which is not considered in this study.

### 6.3.1 Mass + Substructure Performance

As already noted, the largest background rejection at 70% signal efficiency are in general achieved using those two variable BDT combinations which involve a groomed mass and a non-mass substructure variable. For both  $R=0.8$  and  $R=1.2$  jets, the rejection power of these two variable combinations increases substantially with increasing  $p_T$ , at least within the  $p_T$  range considered here.

For a jet radius of  $R=0.8$ , across the full  $p_T$  range considered, the groomed mass + substructure variable combinations with the largest background rejection are those which involve  $C_2^{\beta=1}$ . For example, in combination with  $m_{sd}^{\beta=2}$ , this produces a five-, eight- and fifteen-fold

increase in background rejection compared to using the groomed mass alone. In Figure 22 the low degree of correlation between  $m_{sd}^{\beta=2}$  versus  $C_2^{\beta=1}$  that leads to these large improvements in background rejection can be seen. One can also see that what little correlation exists is rather non-linear in nature, changing from a negative to a positive correlation as a function of the groomed mass, something which helps to improve the background rejection in the region of the W mass peak.

However, when we switch to a jet radius of  $R=1.2$  the picture for  $C_2^{\beta=1}$  combinations changes dramatically. These become significantly less powerful, and the most powerful variable in groomed mass combinations becomes  $\tau_{21}^{\beta=1}$  for all jet  $p_T$  considered. Figure 23 shows the correlation between  $m_{sd}^{\beta=2}$  and  $C_2^{\beta=1}$  in the  $p_T$  1.0 - 1.2 TeV bin for the various jet radii considered. Figure 24 is the equivalent set of distributions for  $m_{sd}^{\beta=2}$  and  $\tau_{21}^{\beta=1}$ . One can see from Figure 23 that, due to the sensitivity of the observable to soft, wide-angle radiation, as the jet radius increases  $C_2^{\beta=1}$  increases and becomes more and more smeared out for both signal and background, leading to worse discrimination power.



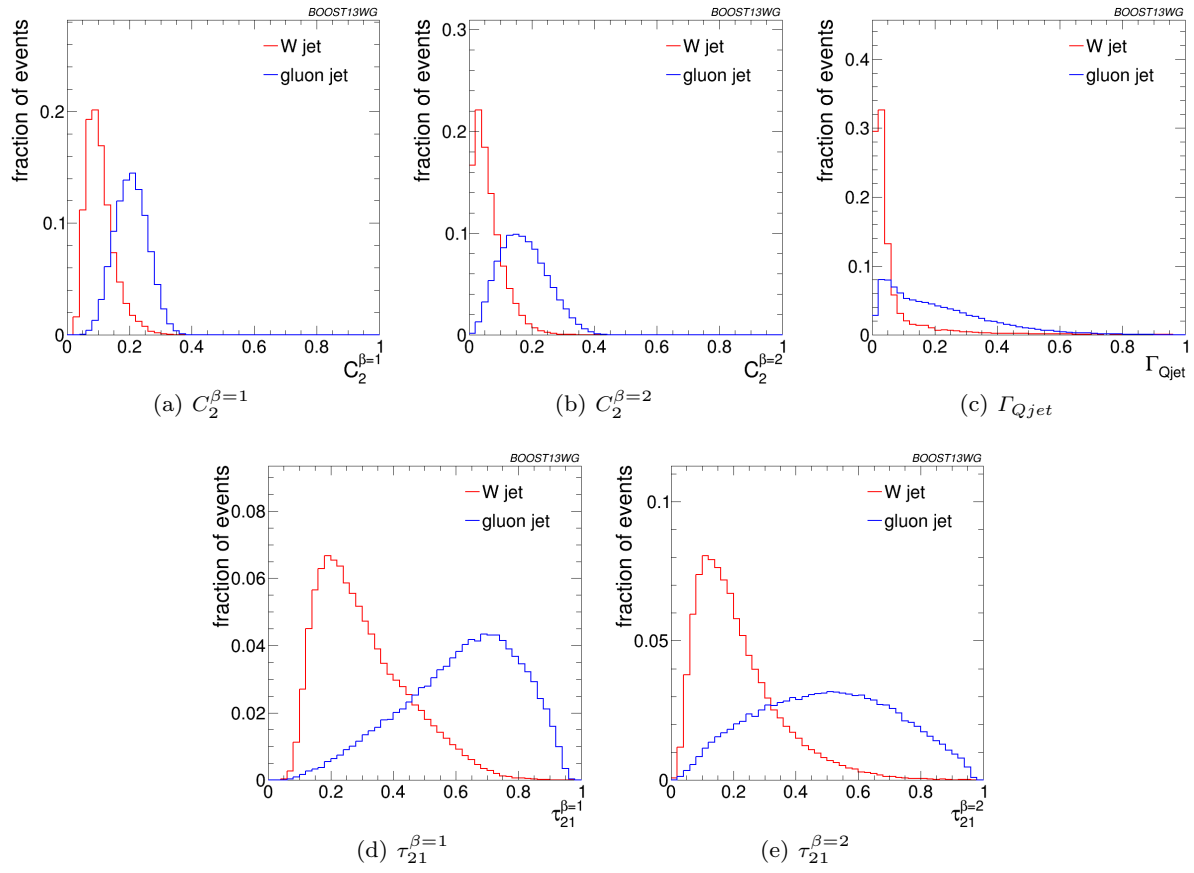


**Fig. 15** Comparisons of the QCD background to the WW signal in the  $p_T$  500-600 GeV bin using the anti- $k_T$   $R=0.8$  algorithm: substructure variables.

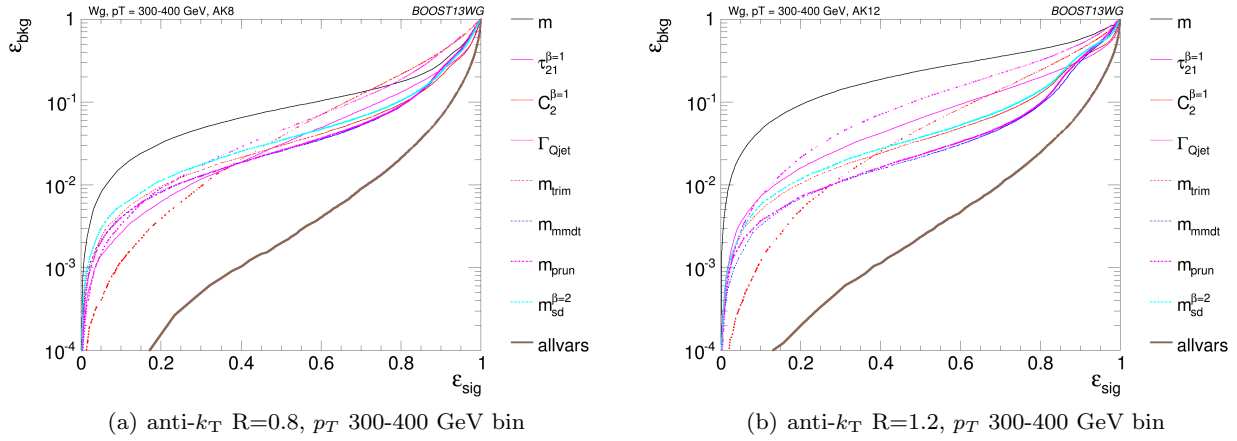


**Fig. 16** The ROC curve for all single variables considered for  $W$  tagging in the  $p_T$  300-400 GeV bin using the anti- $k_T$   $R=0.8$  algorithm and  $R=1.2$  algorithm.

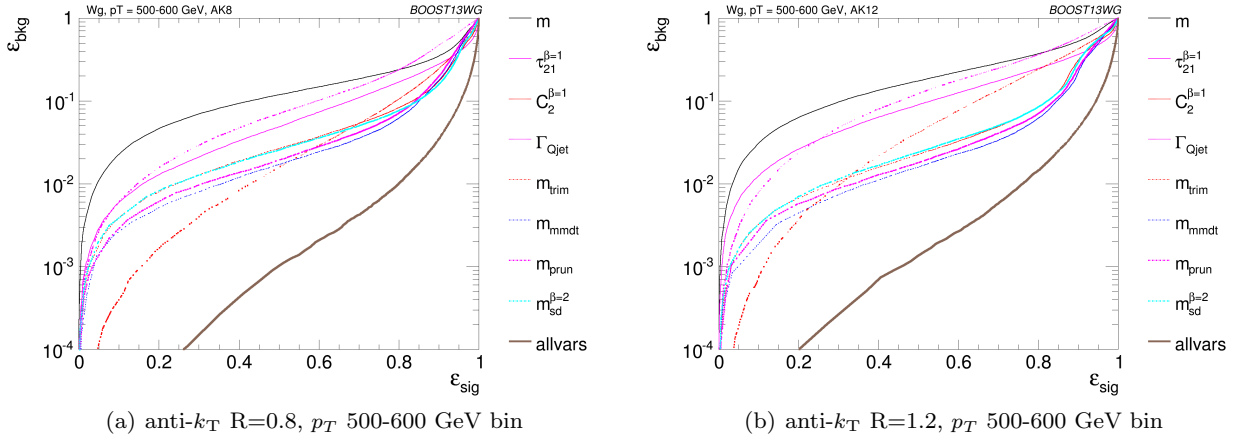


**Fig. 17** The ROC curve for all single variables considered for  $W$  tagging in the  $p_T$  500-600 GeV bin using the anti- $k_T$   $R=0.8$  algorithm and  $R=1.2$  algorithm.

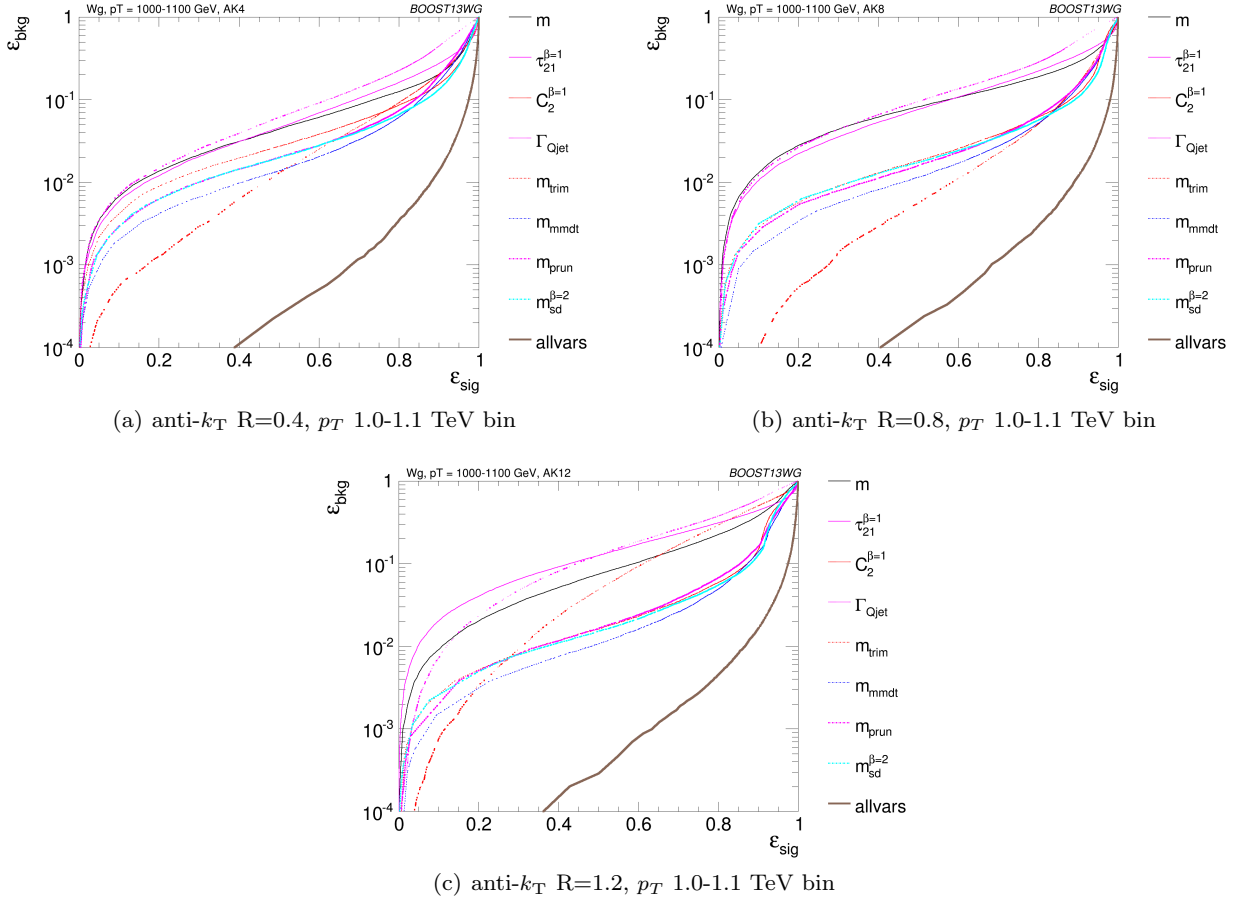


**Fig. 18** The ROC curve for all single variables considered for  $W$  tagging in the  $p_T$  1.0-1.1 TeV bin using the anti- $k_T$   $R=0.4$  algorithm, anti- $k_T$   $R=0.8$  algorithm and  $R=1.2$  algorithm.

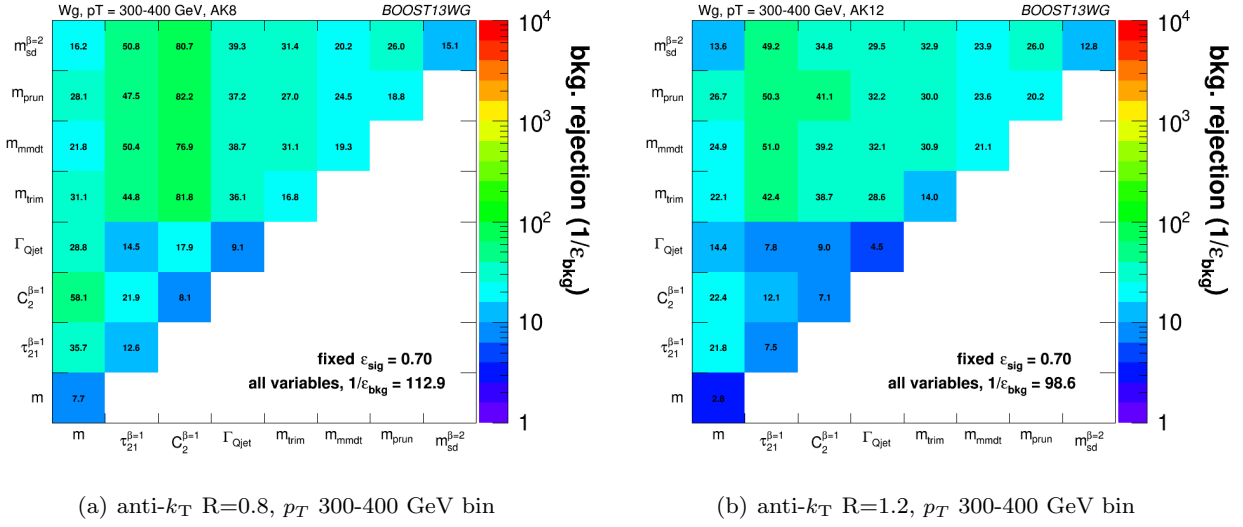


**Fig. 19** The background rejection for a fixed signal efficiency (70%) of each BDT combination of each pair of variables considered, in the  $p_T$  300-400 GeV bin using the anti- $k_T$  R=0.8 algorithm and R=1.2 algorithm. Also shown is the background rejection for a BDT combination of all of the variables considered.

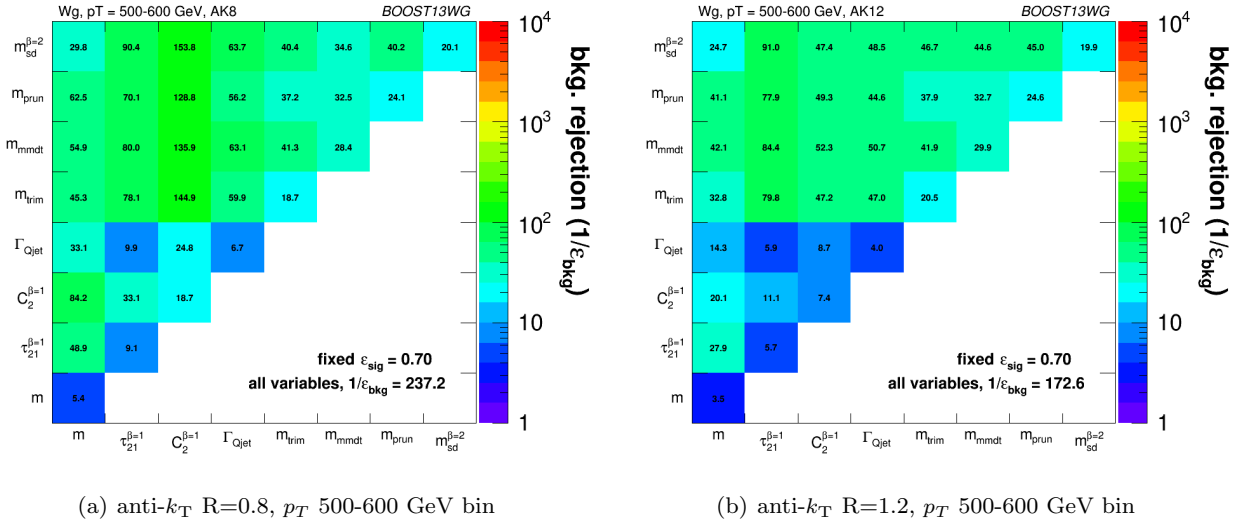


**Fig. 20** The background rejection for a fixed signal efficiency (70%) of each BDT combination of each pair of variables considered, in the  $p_T$  500-600 GeV bin using the anti- $k_T$  R=0.8 algorithm and R=1.2 algorithm. Also shown is the background rejection for a BDT combination of all of the variables considered.

This does not happen to the same extent for  $\tau_{21}^{\beta=1}$ . We can see from Figure 24 that the negative correlation between  $m_{\text{sd}}^{\beta=2}$  and  $\tau_{21}^{\beta=1}$  that is clearly visible for R=0.4 decreases for larger jet radius, such that the groomed mass and substructure variable are far less correlated and  $\tau_{21}^{\beta=1}$  offers improved discrimination within a  $m_{\text{sd}}^{\beta=2}$  mass window.

### 6.3.2 Mass + Mass Performance

The different groomed masses and the ungroomed mass are of course not fully correlated, and thus one can always see some kind of improvement in the background rejection (relative to the single mass performance) when two different mass variables are combined in the BDT. However, in some cases the improvement can be dramatic, particularly at higher  $p_T$ , and particularly for combinations with the ungroomed mass. For example, in Figure 21 we can see that in the  $p_T$  1.0-1.1 TeV bin

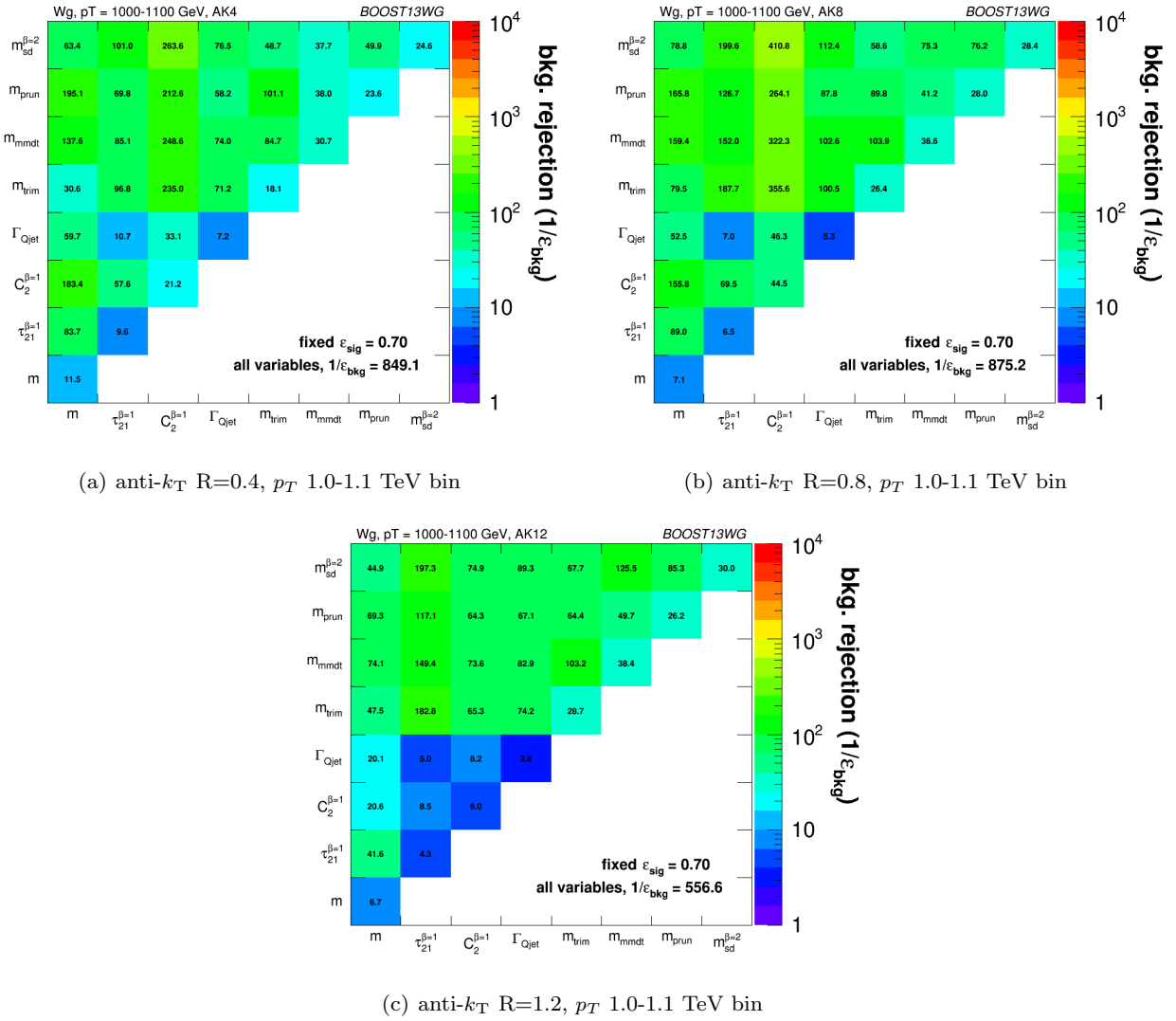


**Fig. 21** The background rejection for a fixed signal efficiency (70%) of each BDT combination of each pair of variables considered, in the  $p_T$  1.0-1.1 TeV bin using the anti- $k_T$   $R=0.4$ ,  $R=0.8$  and  $R=1.2$  algorithm. Also shown is the background rejection for a BDT combination of all of the variables considered.

the combination of pruned mass with ungroomed mass produces a greater than eight-fold improvement in the background rejection for  $R=0.4$  jets, a greater than five-fold improvement for  $R=0.8$  jets, and a factor  $\sim$ two improvement for  $R=1.2$  jets. A similar behaviour can be seen for mMDT mass. In Figures 25, 26 and 27 is shown the 2-D correlation plots of the pruned mass versus the ungroomed mass separately for the WW and  $gg$  background samples in the  $p_T$  1.0-1.1 TeV bin, for various jet radii considered. For comparison, the correlation of the trimmed mass with the ungroomed mass, a combination that does not improve on the single mass as dramatically, is shown. In all cases one can see that there is a much smaller degree of correlation between the pruned mass and the ungroomed mass in the back-

grounds sample than for the trimmed mass and the ungroomed mass. This is most obvious in Figure 25, where the high degree of correlation between the trimmed and ungroomed mass is expected, since with the parameters used (in particular  $R_{trim} = 0.2$ ) we cannot expect trimming to have a significant impact on an  $R=0.4$  jet. The reduced correlation with ungroomed mass for pruning in the background means that, once we have made the requirement that the pruned mass is consistent with a W (i.e.  $\sim 80$  GeV), a relatively large difference between signal and background in the ungroomed mass still remains, and can be exploited to improve the background rejection further. In other words, many of the background events which pass the pruned mass requirement do so because they are shifted to lower mass (to

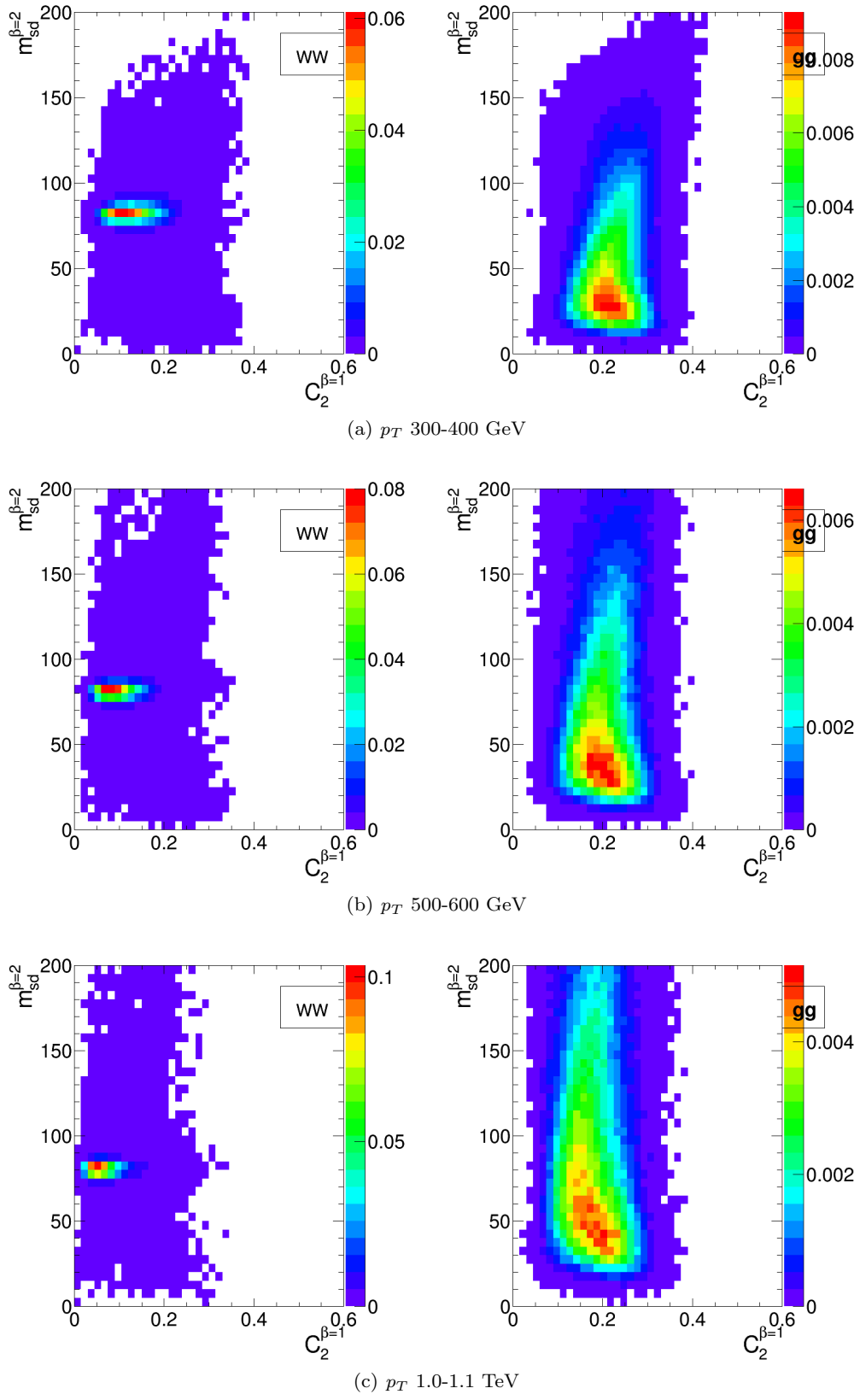


**Fig. 22** 2-D plots showing  $m_{sd}^{\beta=2}$  versus  $C_2^{\beta=1}$  for  $R=0.8$  jets in the various  $p_T$  bins considered.

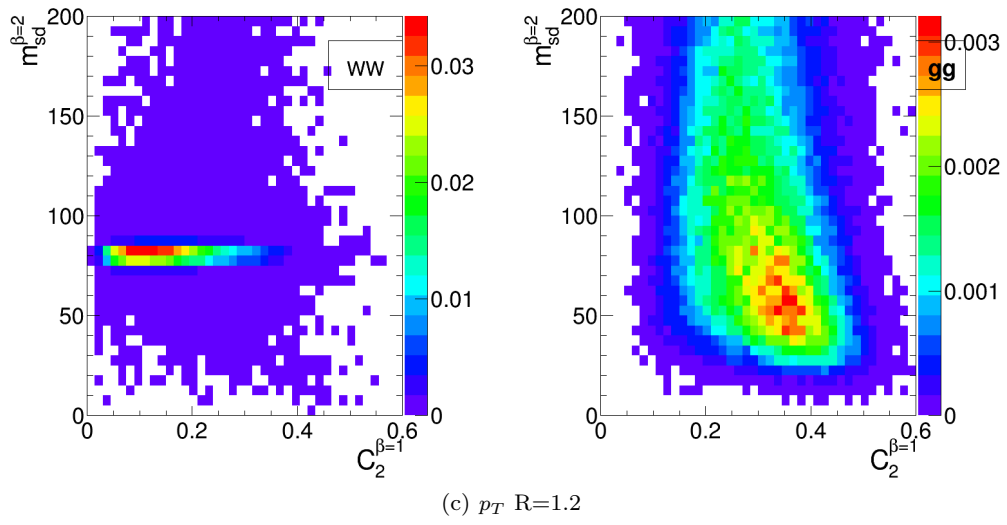
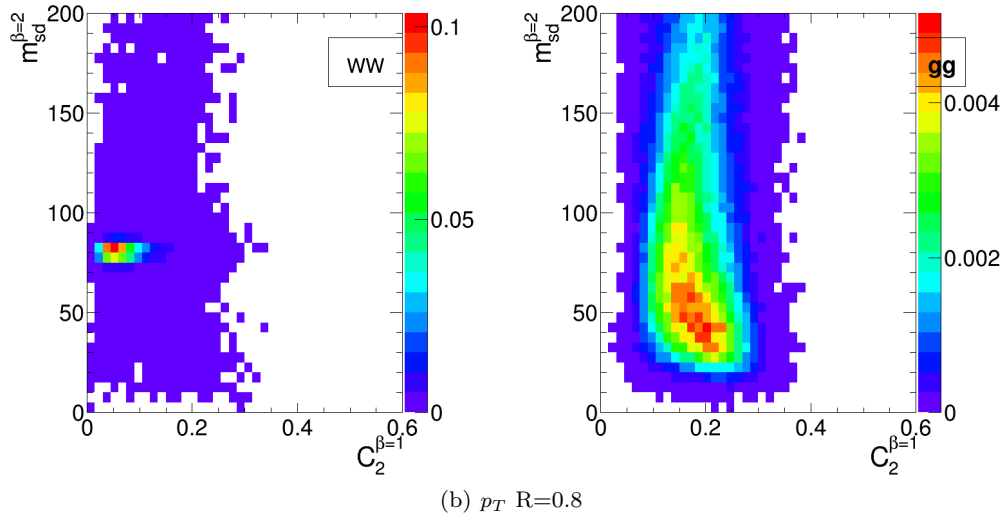
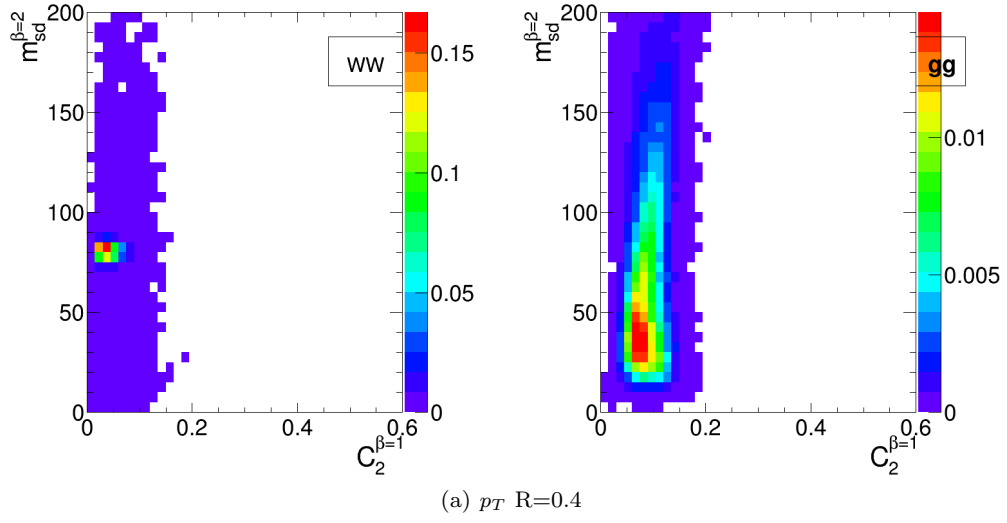


**Fig. 23** 2-D plots showing  $m_{sd}^{\beta=2}$  versus  $C_2^{\beta=1}$  for R=0.4, 0.8 and 1.2 jets in the  $p_T$  1.0-1.1 TeV bin.

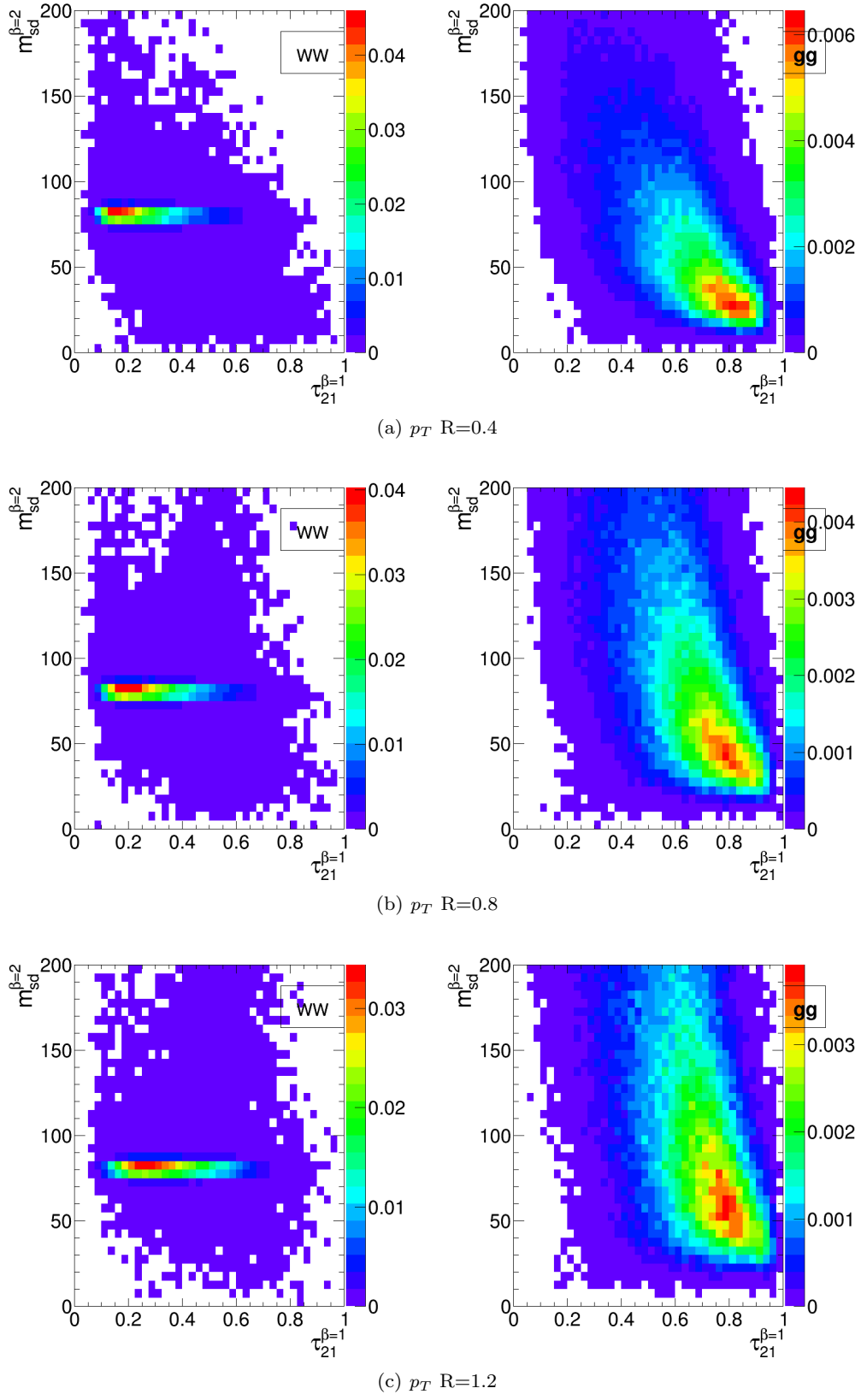


**Fig. 24** 2-D plots showing  $m_{sd}^{\beta=2}$  versus  $\tau_{21}^{\beta=1}$  for  $R=0.4, 0.8$  and  $1.2$  jets in the  $p_T$  1.0-1.1 TeV bin.

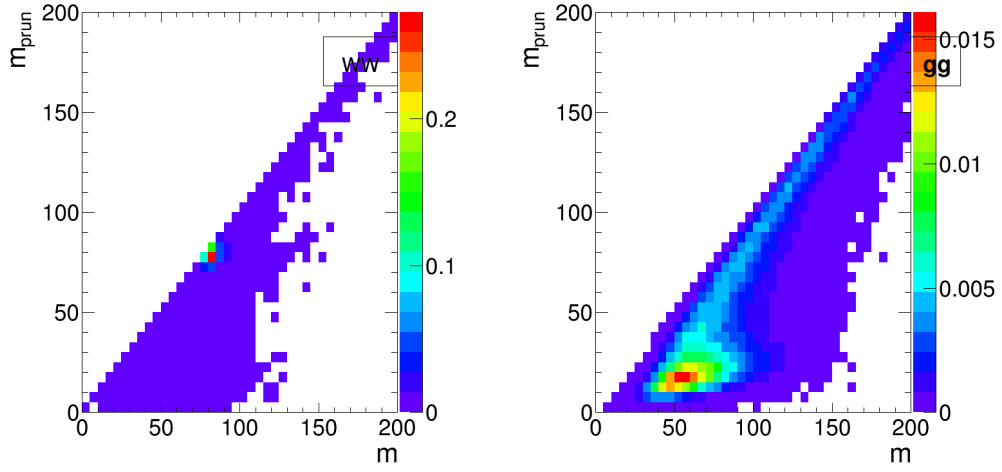
be within a signal mass window) by the grooming, but these events still have the property that they look very much like background events before the grooming. A single requirement on the groomed mass only does not exploit this. Of course, the impact of pile-up, not considered in this study, could significantly limit the degree to which the ungroomed mass could be used to improve discrimination in this way.

### 6.3.3 “All Variables” Performance

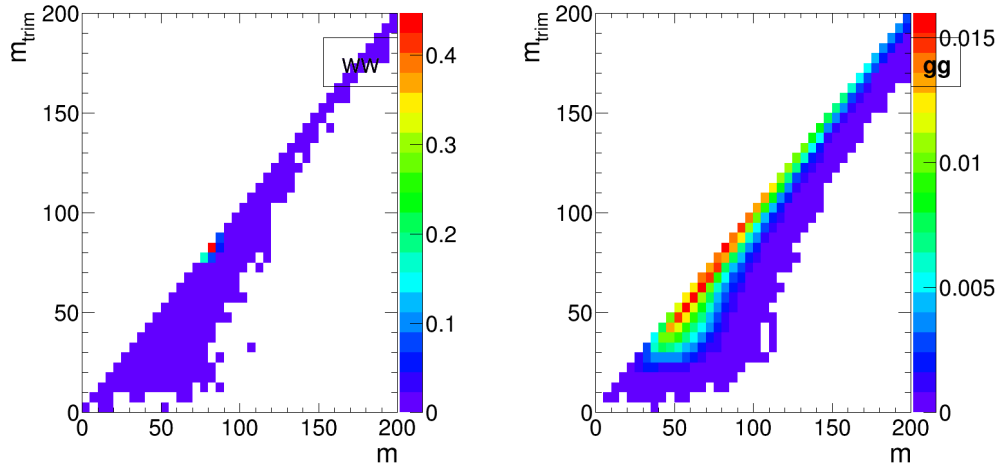
As well as the background rejection at a fixed 70% signal efficiency for two-variable combinations, Figures 19, 20 and 21 also report the background rejection achieved by a combination of all the variables considered into a single BDT discriminant. One can see that, in all cases, the rejection power of this “all variables” BDT is significantly larger than the best two-variable combination, by between a factor 2-3. This indicates that beyond the best two-variable combination there is still significant complementary information available in the remaining variables in order to improve the discrimination of signal and background.

**ED: This section will be filled in when we have got the 3-variable combination studies, so we have a better idea where the dramatic increase in rejection power with “all variables” is coming from. Would also be good to show perhaps some of the “all variables” BDT discriminants in 1-D plots.**



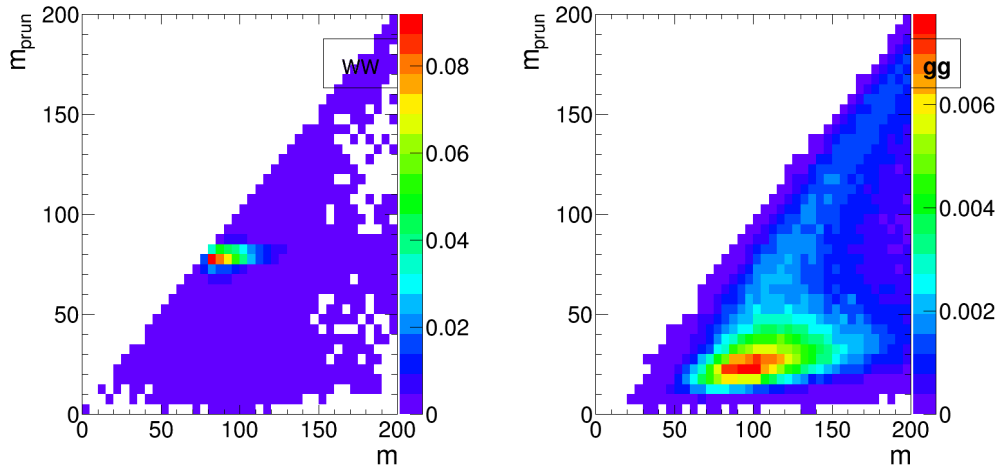


(a) Pruned mass vs ungroomed mass

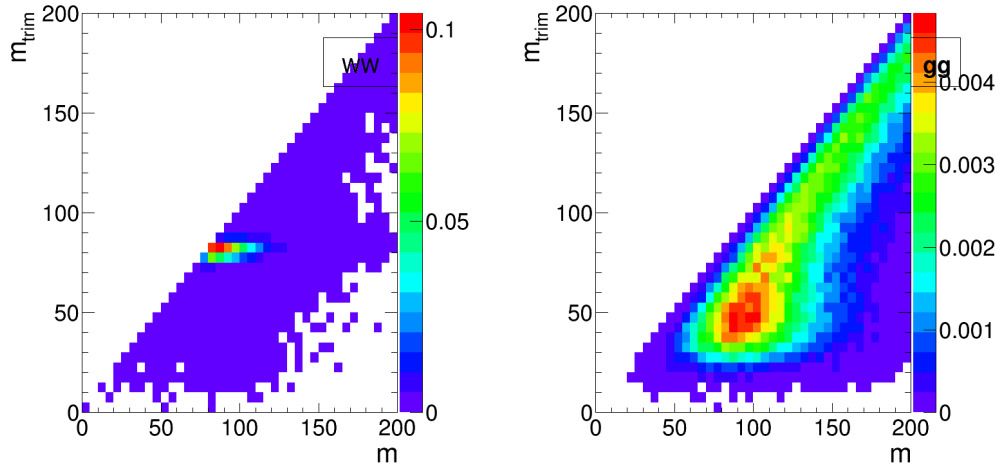


(b) Trimmed mass vs ungroomed mass

**Fig. 25** 2-D plots showing the correlation between groomed and ungroomed mass for  $WW$  and  $gg$  events in the  $p_T$  1.0-1.1 TeV bin using the anti- $k_T$   $R=0.4$  algorithm.

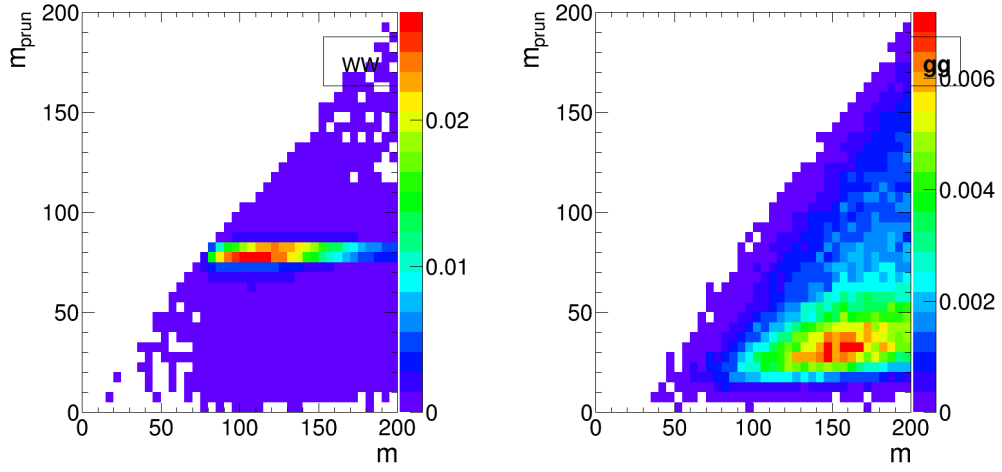


(a) Pruned mass vs ungroomed mass

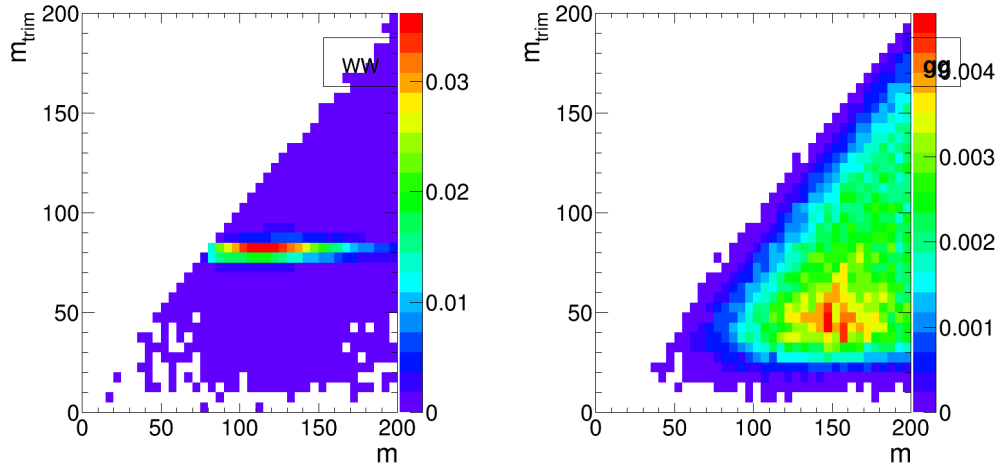


(b) Trimmed mass vs ungroomed mass

**Fig. 26** 2-D plots showing the correlation between groomed and ungroomed mass for  $WW$  and  $gg$  events in the  $p_T$  1.0-1.1 TeV bin using the anti- $k_T$   $R=0.8$  algorithm.



(a) Pruned mass vs ungroomed mass



(b) Trimmed mass vs ungroomed mass

**Fig. 27** 2-D plots showing the correlation between groomed and ungroomed mass for  $WW$  and  $gg$  events in the  $p_T$  1.0-1.1 TeV bin using the anti- $k_T$   $R=1.2$  algorithm.

## 7 Top Tagging

In this section, we study the identification of boosted top quarks at Run II of the LHC. Boosted top quarks result in large-radius jets with complex substructure, containing a  $b$ -subjett and a boosted  $W$ . The additional kinematic handles coming from the reconstruction of the  $W$  mass and  $b$ -tagging allows a very high degree of discrimination of top quark jets from QCD backgrounds.

We consider top quarks with moderate boost (600–1000 GeV), and perhaps most interestingly, at high boost ( $\gtrsim 1500$  GeV). Top tagging faces several challenges in the high- $p_T$  regime. For such high- $p_T$  jets, the  $b$ -tagging efficiencies are no longer reliably known. Also, the top jet can also be accompanied by additional

radiation with  $p_T \sim m_t$ , leading to combinatoric ambiguities of reconstructing the top and  $W$ , and the possibility that existing taggers or observables shape the background by looking for subjet combinations that reconstruct  $m_t/m_W$ . To study this, we examine the performance of both mass-reconstruction variables, as well as shape observables that probe the three-pronged nature of the top jet and the accompanying radiation pattern.

### 7.1 Methodology

We study a number of top-tagging strategies, in particular:

1. HEPTopTagger
2. Johns Hopkins Tagger (JH)
3. Trimming
4. Pruning

The top taggers have criteria for reconstructing a top and  $W$  candidate, while the grooming algorithms (trimming and pruning) do not incorporate a  $W$ -identification step. For a level playing field, we construct a  $W$  candidate from the three leading subjets by taking the pair of subjets with the smallest invariant mass; in the case that only two subjets are reconstructed, we take the mass of the leading subjet. All of the above taggers and groomers incorporate a step to remove pile-up and other soft radiation.

We also consider the performance of jet shape observables. In particular, we consider the  $N$ -subjettiness ratios  $\tau_{32}^{\beta=1}$  and  $\tau_{21}^{\beta=1}$ , energy correlation function ratios  $C_3^{\beta=1}$  and  $C_2^{\beta=1}$ , and the Qjet mass volatility  $\Gamma$ . In addition to the jet shape performance, we combine the jet shapes with the mass-reconstruction methods listed above to determine the optimal combined performance.

For determining the performance of multiple variables, we combine the relevant tagger output observables and/or jet shapes into a boosted decision tree (BDT), which determines the optimal cut. Additionally, because each tagger has two inputs (list, or maybe refer back to Section 3), we scan over reasonable values of the inputs to determine the optimal value for each top tagging signal efficiency. This allows a direct comparison of the optimized version of each tagger. The input values scanned for the various algorithms are:

- **HEPTopTagger:**  $m \in [30, 100]$  GeV,  $\mu \in [0.5, 1]$
- **JH Tagger:**  $\delta_p \in [0.02, 0.15]$ ,  $\delta_R \in [0.07, 0.2]$
- **Trimming:**  $f_{\text{cut}} \in [0.02, 0.14]$ ,  $R_{\text{trim}} \in [0.1, 0.5]$
- **Pruning:**  $z_{\text{cut}} \in [0.02, 0.14]$ ,  $R_{\text{cut}} \in [0.1, 0.6]$

## 7.2 Single-observable performance

We start by investigating the behaviour of individual jet substructure observables. Because of the rich, three-pronged structure of the top decay, it is expected that combinations of masses and jet shapes will far outperform single observables in identifying boosted tops. However, a study of the top-tagging performance of single variables facilitates a direct comparison with the  $W$  tagging results in Section 6, and also allows a straightforward examination of the performance of each observable for different  $p_T$  and jet radius.

Fig. 28 shows the ROC curves for each of the top-tagging observables, with the bare jet mass also plotted for comparison. Unlike  $W$  tagging, the jet shape observables perform more poorly than jet mass. As an example illustrating why this is the case, consider  $N$ -subjettiness. The  $W$  is two-pronged and the top is three-pronged; therefore, we expect  $\tau_{21}$  and  $\tau_{32}$  to be the best-performing  $N$ -subjettiness ratio, respectively. However,  $\tau_{21}$  also contains an implicit cut on the denominator,  $\tau_1$ , which is strongly correlated with jet mass. Therefore,  $\tau_{21}$  combines both mass and shape information to some extent. By contrast, and as is clear in Fig. 28(a), the best shape for top tagging is  $\tau_{32}$ , which contains no information on the mass. Therefore, it is unsurprising that the shapes most useful for top tagging are less sensitive to the jet mass, and under-perform relative to the corresponding observables for  $W$  tagging.

Of the two top tagging algorithms, the Johns Hopkins (JH) tagger out-performs the HEPTopTagger in its signal-to-background separation of both the top and  $W$  candidate masses, with larger discrepancy at higher  $p_T$  and larger jet radius. In Fig. 29, we show the histograms for the top mass output from the JH and HEPTopTagger for different  $R$  (Fig. 29) and  $p_T$  (30), optimized at a signal efficiency of 30%. The likely reason for this behavior is that, in the HEPTopTagger algorithm, the jet is filtered to select the five hardest subjects, and then three subjects are chosen which reconstruct the top mass. This requirement tends to shape a peak in the QCD background around  $m_t$  for the HEPTopTagger, while the JH tagger has no such requirement. It has been suggested by Anders *et al.* [?] that performance in the HEPTopTagger may be improved by selecting three subjects reconstructing the top only among those that pass the  $W$  mass constraints, which somewhat reduces the shaping of the background. Note that both the JH tagger and the HEPTopTagger are superior using the  $W$  candidate inside of the top for signal discrimination; this is because the pruning and trimming algorithms do not have inherent  $W$ -identification steps and are not optimized for this purpose.

We also directly compare the performance of top mass and jet shape observables for different jet  $p_T$  and radius. The input parameters of the taggers, groomers, and shape variables are separately optimized for each  $p_T$  and radius:

**$p_T$  comparison:** We compare various top tagging observables for jets in different  $p_T$  bins and  $R = 0.8$  in Figs. 31 and 34. The tagging performance of jet shapes do not change substantially with  $p_T$ .  $\tau_{32}^{(\beta=1)}$  and the Qjet volatility  $\Gamma$  have the most variation and tend to degrade with higher  $p_T$  (see Fig. 32-33). This makes sense, as higher- $p_T$  QCD jets have more, harder emissions within the jet, giving rise to substructure that fakes the signal. By contrast, most of the top mass observables have superior performance at higher  $p_T$  due to the radiation from the top quark becoming more collimated. The notable exception is the HEPTopTagger, which degrades at higher  $p_T$ , likely in part due to the background-shaping effects discussed earlier.

**$R$  comparison:** We compare various top tagging observables for jets of different  $R$  and  $p_T = 1.5 - 1.6$  TeV in Figs. 35-39. Most of the top-tagging parameters perform best for smaller radius; this is because, at such high  $p_T$ , most of the radiation from the top quark is confined within  $R = 0.4$ , and having a larger jet radius makes the observable more susceptible to contamination from the underlying event and other uncorrelated radiation. As we show in Figs. 36-38, the distributions for both signal broaden with increasing  $R$ , degrading the discriminating power. For  $C_2^{(\beta=1)}$  and  $C_3^{(\beta=1)}$ , the background distributions are shifted upward as well. Therefore, the discriminating power generally gets worse with increasing  $R$ . The main exception is for  $C_3^{(\beta=1)}$ , which performs optimally at  $R = 0.8$ ; in this case, the signal and background coincidentally happen to have the same distribution around  $R = 0.4$ , and so  $R = 0.8$  gives better discrimination.

## 7.3 Performance of multivariable combinations

We now consider various combinations of the observables from Section 7.2. In particular, we consider the performance of individual taggers such as the JH tagger and HEPTopTagger, which output information about the  $t$  and  $W$  candidate masses and the helicity angle; groomers, such as trimming and pruning, which remove soft, uncorrelated radiation from the top candidate to improve mass reconstruction, and to which we have added a  $W$  reconstruction step; and the combination of the above taggers/groomers with shape variables such

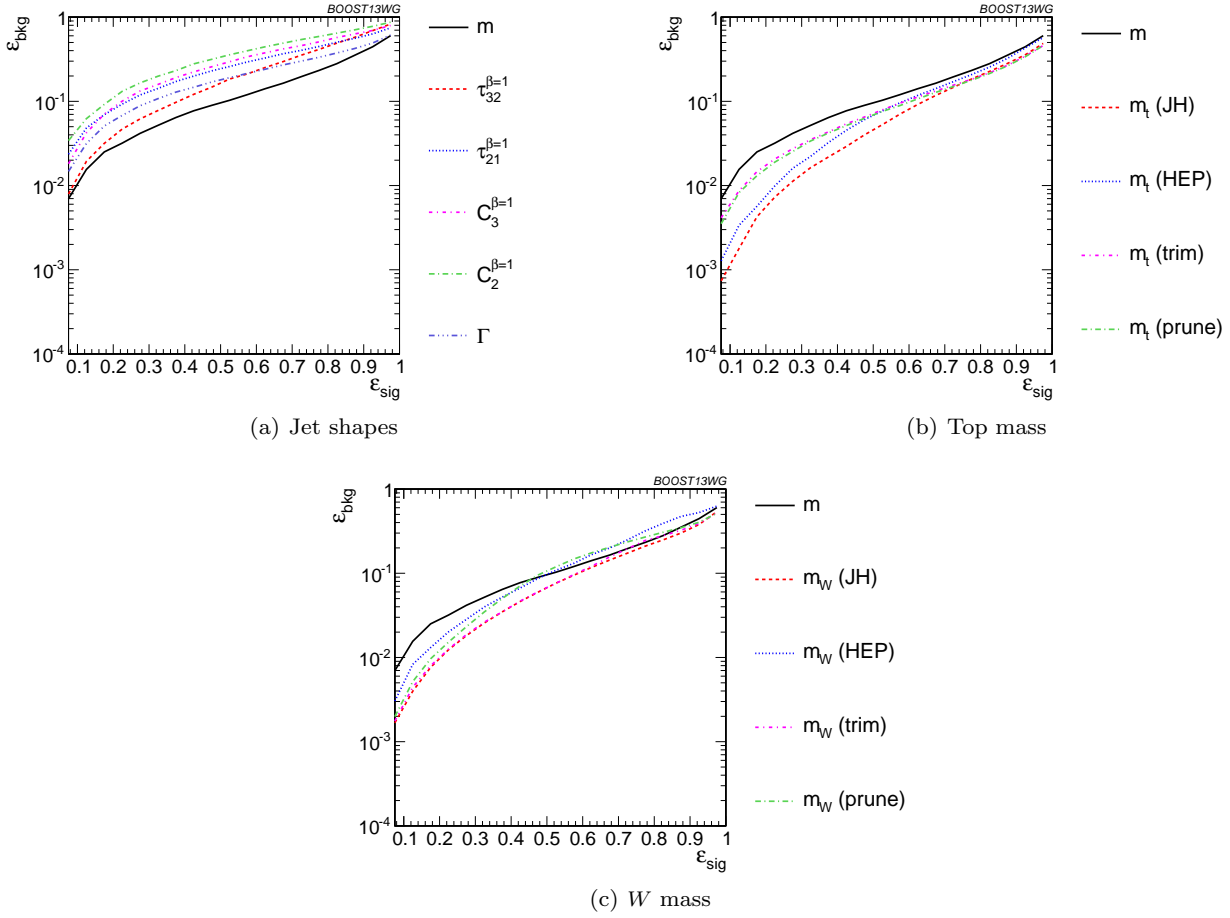


**Fig. 28** Comparison of single-variable top-tagging performance in the  $p_T = 1 - 1.1$  GeV bin using the anti- $k_T$ ,  $R=0.8$  algorithm.

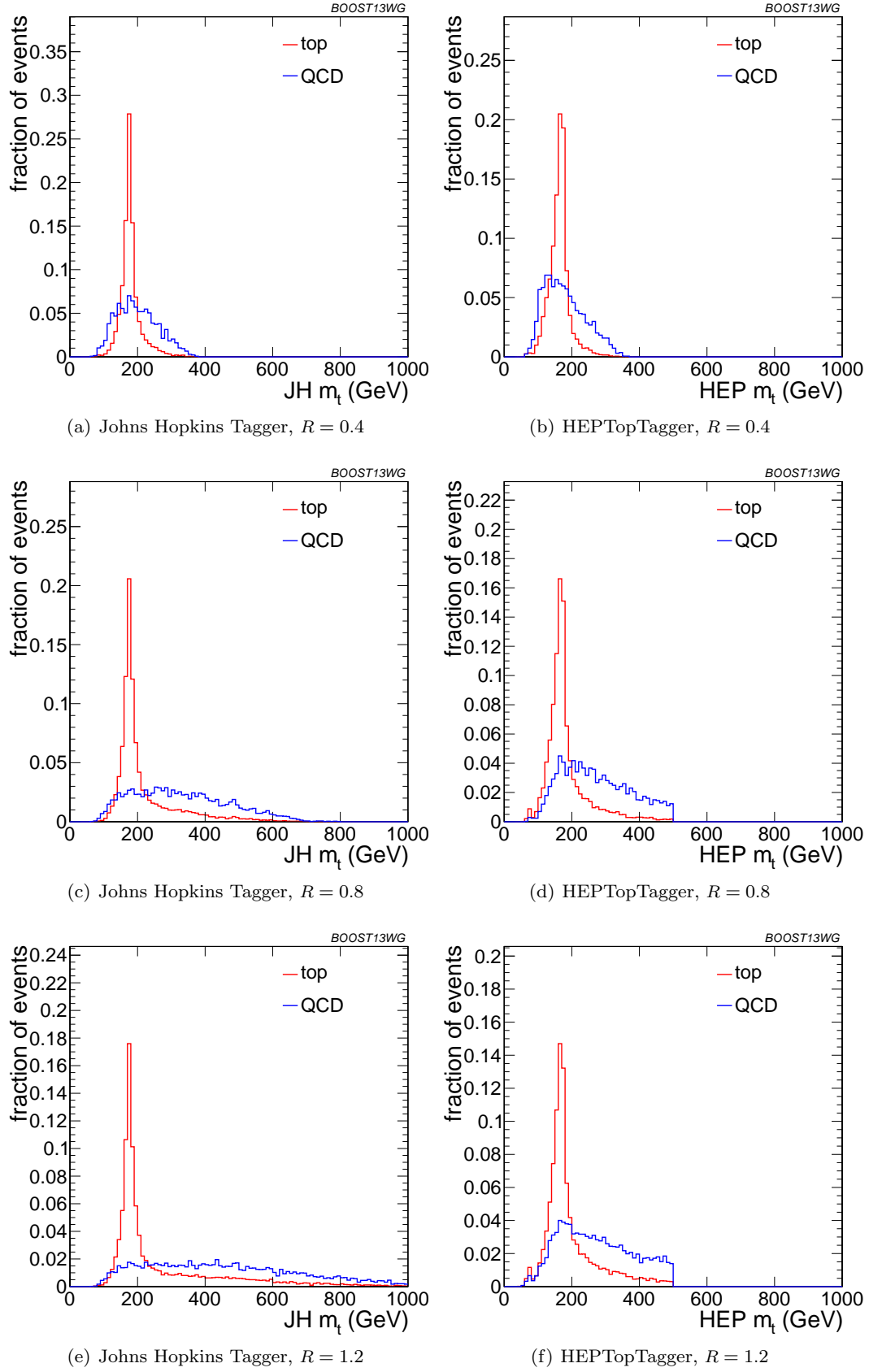
as  $N$ -subjettiness ratios and energy correlation ratios. For all observables with tuneable input parameters, we scan and optimize over realistic values of such parameters. Our multivariate techniques are discussed in Section 4.

Fig. 40 shows our main results for the multivariable combinations; in all cases, we also show the ungroomed jet mass as a baseline comparison. In Fig. 40(a), we directly compare the performance of the HEPTopTagger, the JH tagger, trimming, and grooming. Generally, we find that pruning, which does not naturally incorporate subjets into the algorithm, does not perform as well as the others. Interestingly, trimming, which does include a subjet-identification step, performs comparably to the HEPTopTagger over much of the range, possibly due to the background-shaping observed in Section 7.2. By contrast, the JH tagger outperforms the other algorithms.

To determine whether there is complementary information in the mass outputs from different top taggers, we also consider a multivariable combination of all

of the JH and HEPTopTagger outputs. The maximum efficiency of the combined JH and HEPTopTaggers is limited, as some fraction of signal events inevitably fails either one or other of the taggers. We do see a 20-50% improvement in performance when combining all outputs, which suggests that the different algorithms used to identify the  $t$  and  $W$  for different taggers contains complementary information.

In Fig. 40(b)-(d), we present the results for multivariable combinations of top tagger outputs with and without shape variables. We see that, for both the HEPTopTagger and the JH tagger, the shape observables contain additional information uncorrelated with the masses and helicity angle, and give on average 2-3 improvement in signal discrimination. We see that, when combined with the tagger outputs, both the energy correlation functions  $C_2 + C_3$  and the  $N$ -subjettiness ratios  $\tau_{21} + \tau_{32}$  give comparable performance, while the Qjet mass volatility is slightly worse; this is unsurprising, as Qjets accesses shape information in a more indirect way from other shape observables. Combining all shape ob-



**Fig. 29** Comparison of top mass reconstruction with the JH and HEPTopTaggers at different  $R$  using the anti- $k_T$  algorithm,  $p_T = 1.5 - 1.6$  TeV. Each histogram is shown for the working point optimized for best performance with  $m_t$  in the  $0.3 - 0.35$  signal efficiency bin, and is normalized to the fraction of events passing the tagger.

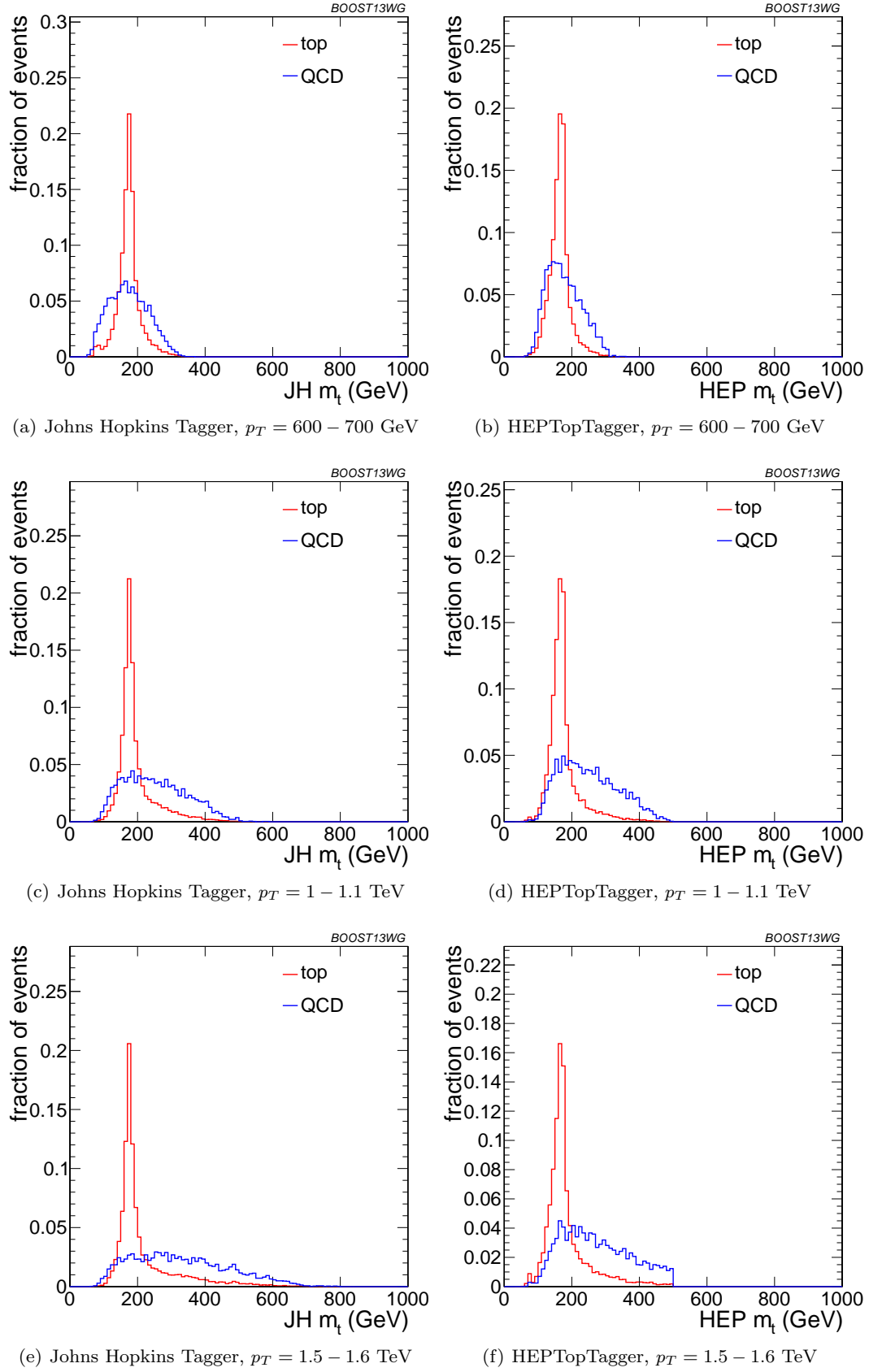


**Fig. 30** Comparison of top mass reconstruction with the JH and HEPTopTaggers at different  $p_T$  using the anti- $k_T$  algorithm,  $R = 0.8$ . Each histogram is shown for the working point optimized for best performance with  $m_t$  in the  $0.3 - 0.35$  signal efficiency bin, and is normalized to the fraction of events passing the tagger.



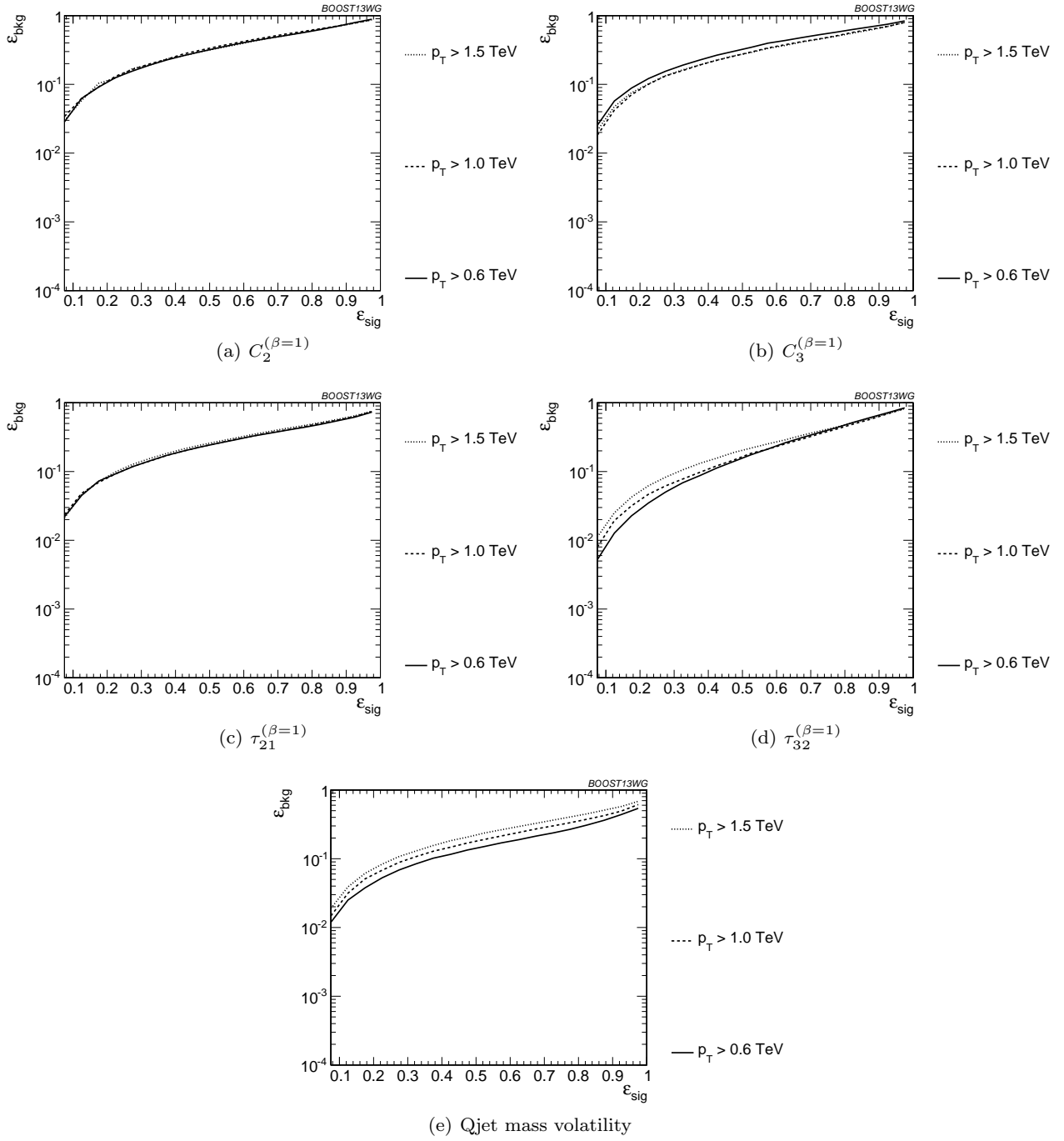


**Fig. 31** Comparison of individual jet shape performance at different  $p_T$  using the anti- $k_T$   $R=0.8$  algorithm.

servables with a single top tagger provides even more enhancement in discrimination power.

We directly compare the performance of the JH and HEPTopTaggers in Fig. 40(d). Combining the taggers with shape information nearly erases the difference between the tagging methods observed in Fig. 40(a); this indicates that combining the shape information with the HEPTopTagger identifies the differences between

signal and background missed by the tagger alone. This also suggests that further improvement to discriminating power may be minimal, as various multivariable combinations are converging to within a factor of 20% or so.

In Fig. 40(e)-(g), we present the results for multivariable combinations of groomer outputs with and without shape variables. As with the tagging algorithms,

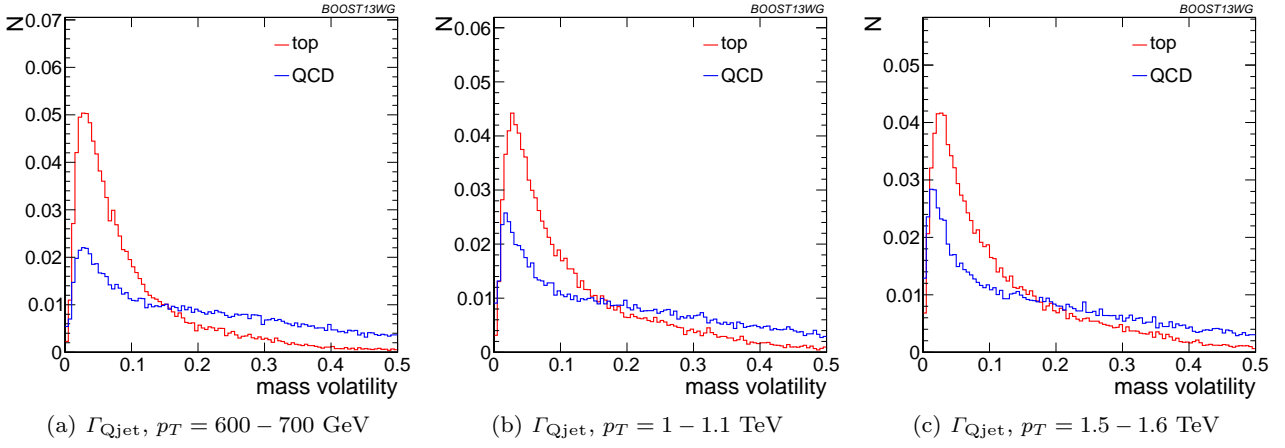


**Fig. 32** Comparison of  $\Gamma_{Qjet}$  at  $R = 0.8$  and different values of the  $p_T$ .

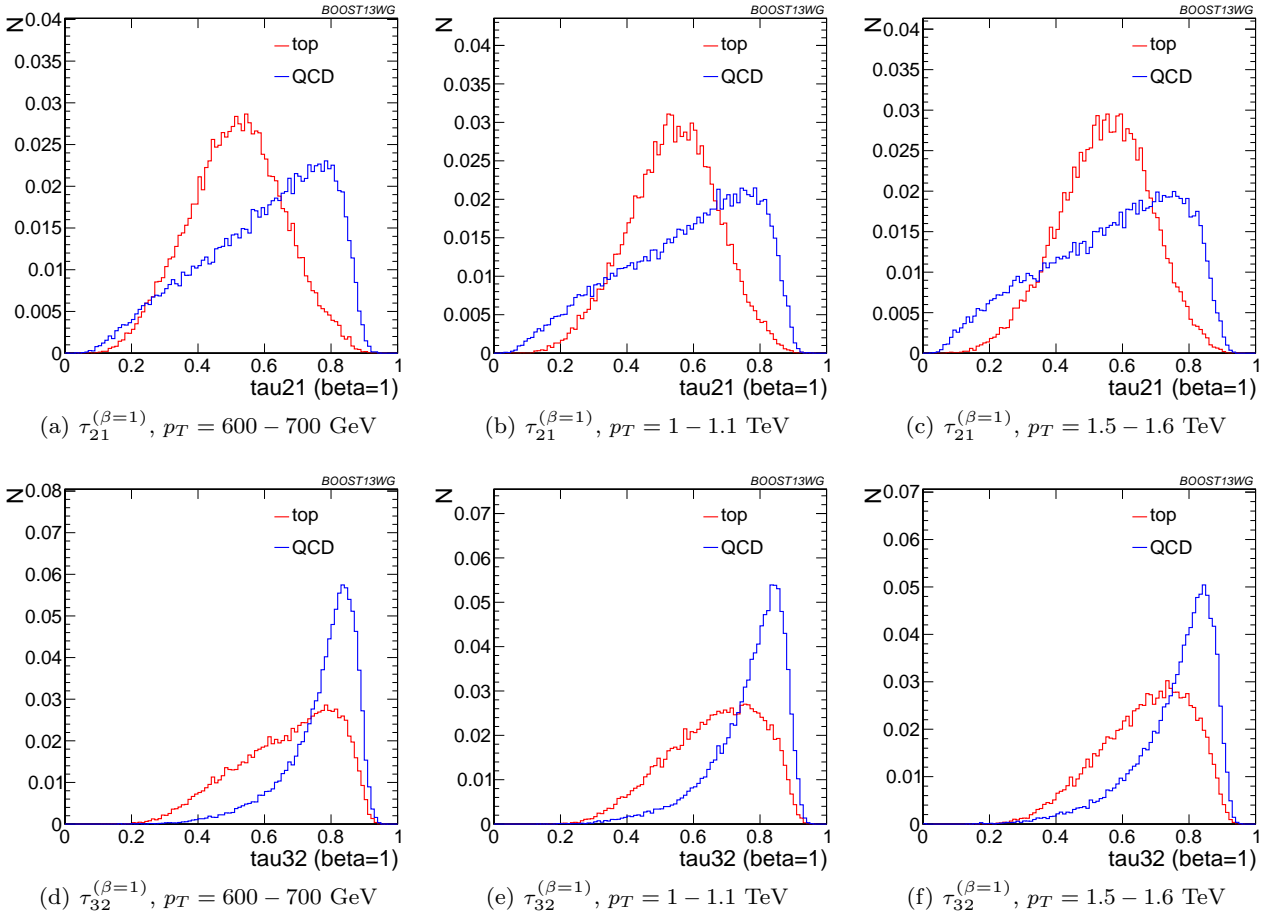


**Fig. 33** Comparison of  $\tau_{21}^{\beta=1}$  and  $\tau_{32}^{\beta=1}$  with  $R = 0.8$  and different values of the  $p_T$ .

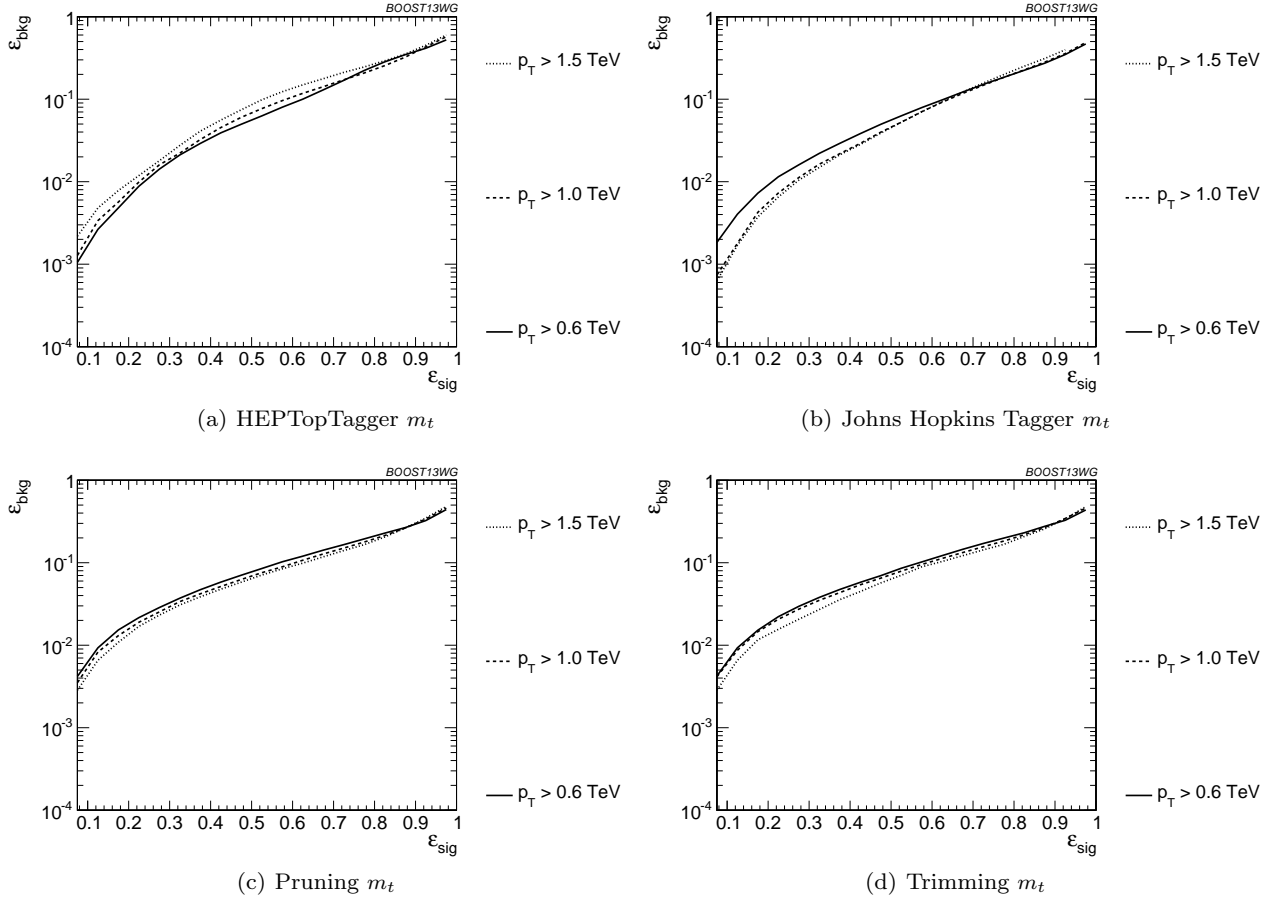


**Fig. 34** Comparison of top mass performance of different taggers at different  $p_T$  using the anti- $k_T$   $R=0.8$  algorithm.

combinations of groomers with shape observables improves their discriminating power; combinations with  $\tau_{32} + \tau_{21}$  perform comparably to those with  $C_3 + C_{21}$  and both of these are superior to combinations with the mass volatility,  $\Gamma$ . Substantial improvement is further possible by combining the groomers with all shape observables. Not surprisingly, the taggers that lag behind in performance enjoy the largest gain in signal-background discrimination with the addition of shape observables. Once again, in 40(g), we find that the differences between pruning and trimming are erased when combined with shape information.

**$p_T$  comparison:** We now compare the BDT combinations of tagger outputs, with and without shape variables, at different  $p_T$ . The taggers are optimized over all input parameters for each choice of  $p_T$  and signal efficiency. As with the single-variable study, we consider anti- $k_T$  jets clustered with  $R = 0.8$  and compare the outcomes in the  $p_T = 500-600$  GeV,  $p_T = 1-1.1$  TeV and  $p_T = 1.5-1.6$  TeV bins. The comparison of the taggers/groomers is shown in Fig. 41. The behaviour with

$p_T$  is qualitatively similar to the behaviour of the  $m_t$  observable for each tagger/groomer shown in Fig. 34; this suggests that the  $p_T$  behaviour of the taggers is dominated by the top mass reconstruction. As before, the HEPTopTagger performance degrades slightly with increased  $p_T$  due to the background shaping effect, while the JH tagger and groomers modestly improve in performance.

In Fig. 42, we show the  $p_T$  dependence of BDT combinations of the JH tagger output combined with shape observables. We find that the curves look nearly identical: the  $p_T$  dependence is dominated by the top mass reconstruction, and combining the tagger outputs with different shape observables does not substantially change this behaviour. The same holds true for trimming and pruning. By contrast, HEPTopTagger ROC curves, shown in Fig. 43, do change somewhat when combined with different shape observables; due to the suboptimal performance of the HEPTopTagger at high  $p_T$ , we find that combining the HEPTopTagger with  $C_3^{(\beta=1)}$ , which in Fig. 31(b) is seen to have some modest improvement at high  $p_T$ , can improve its perfor-

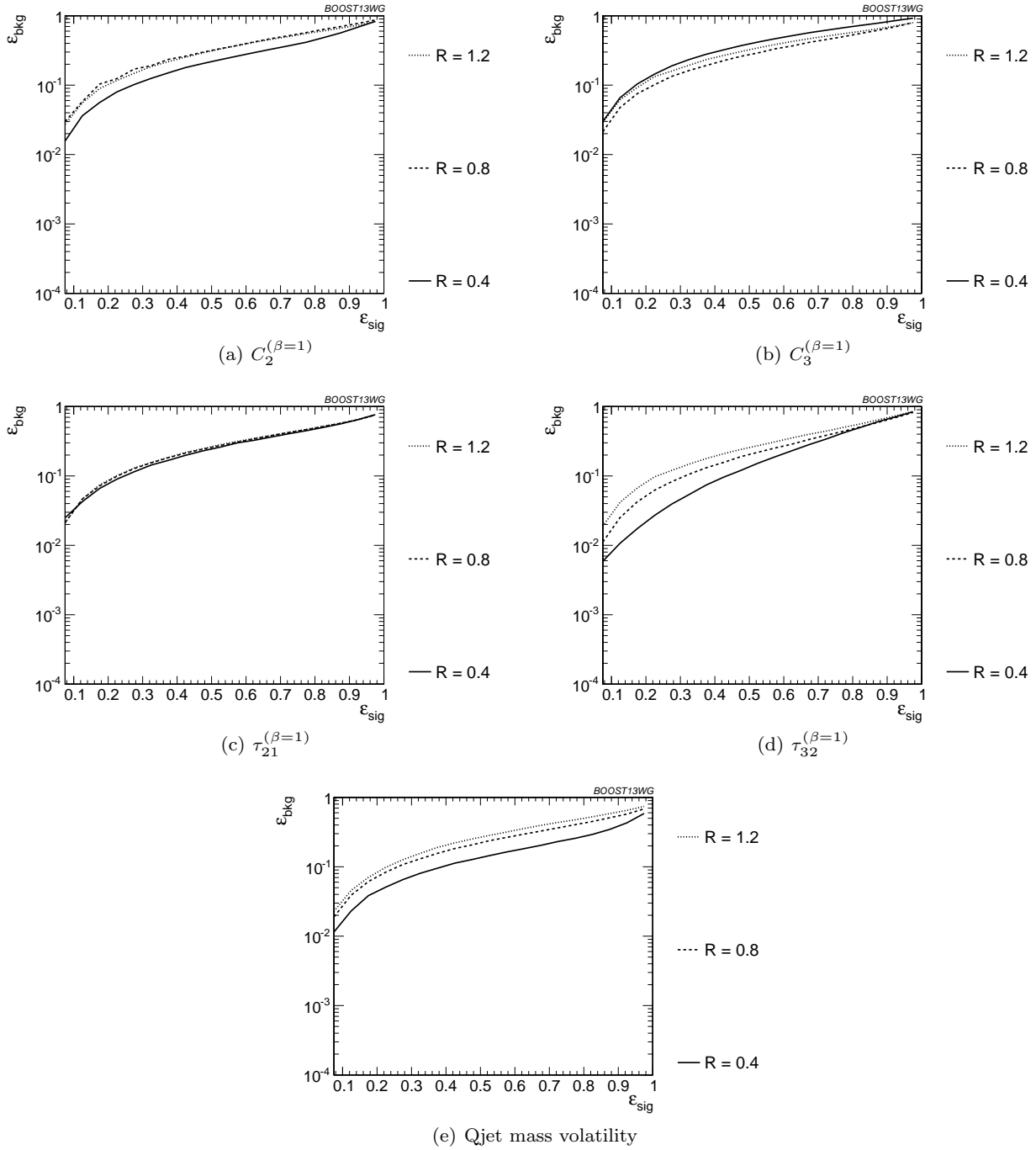


**Fig. 35** Comparison of individual jet shape performance at different  $R$  in the  $p_T = 1.5 - 1.6$  TeV bin.

mance. Combining the HEPTopTagger with multiple shape observables gives the maximum improvement in performance at high  $p_T$  relative to at low  $p_T$ .

**$R$  comparison:** We now compare the BDT combinations of tagger outputs, with and without shape variables, at different  $R$  and  $p_T = 1.5 - 1.6$  TeV. The taggers are optimized over all input parameters for each

choice of  $R$  and signal efficiency, with the results shown in Fig. 44. We find that, for all taggers and groomers, the performance is always best at small  $R$ ; the choice of  $R$  is sufficiently large to admit the full top quark decay at such high  $p_T$ , but is small enough to suppress contamination from additional radiation. This is not altered when the taggers are combined with shape observables; for example, in the case of the JH tagger

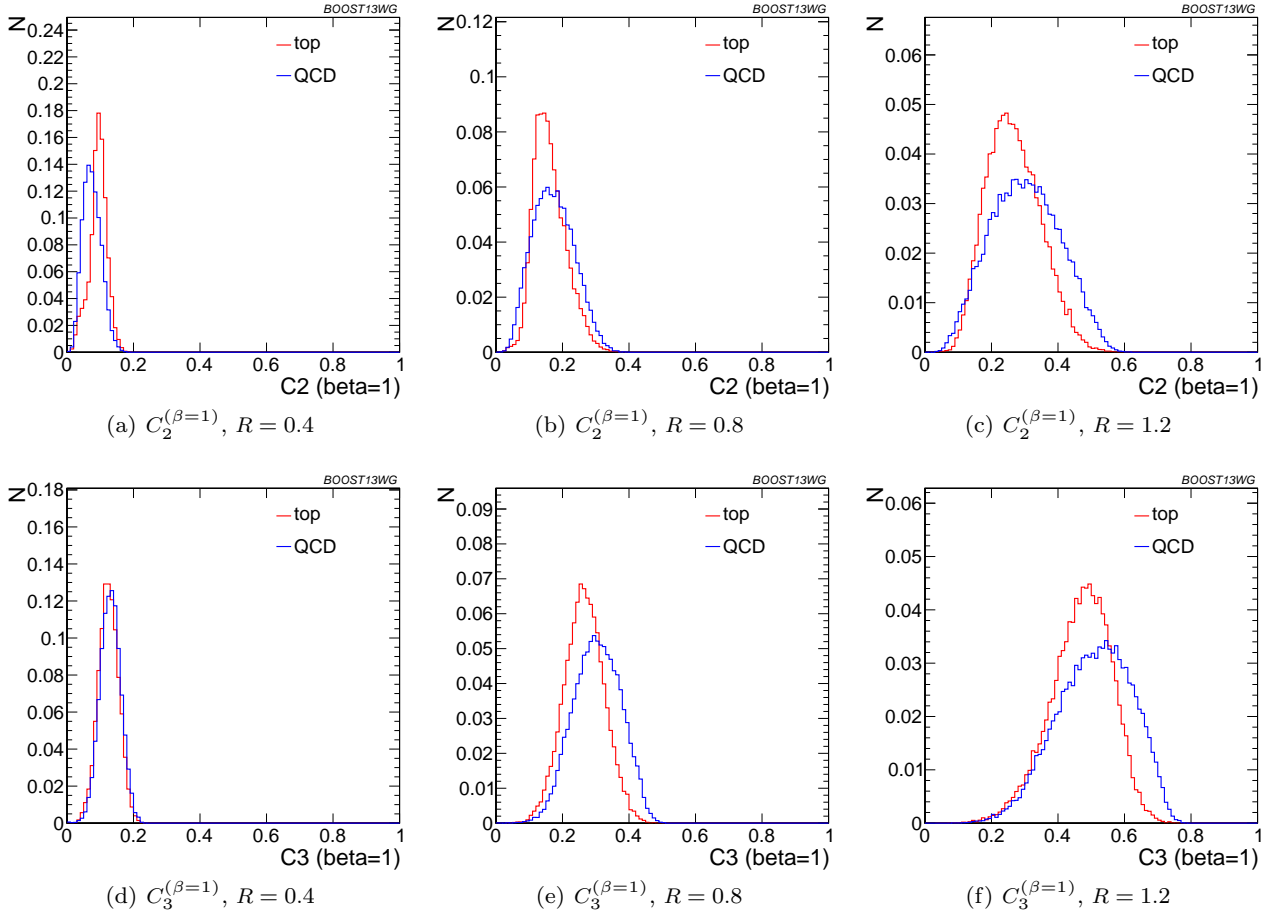


**Fig. 36** Comparison of  $C_2^{\beta=1}$  and  $C_3^{\beta=1}$  in the  $p_T = 1.5 - 1.6$  TeV bin and different values of the anti- $k_T$  radius  $R$ .

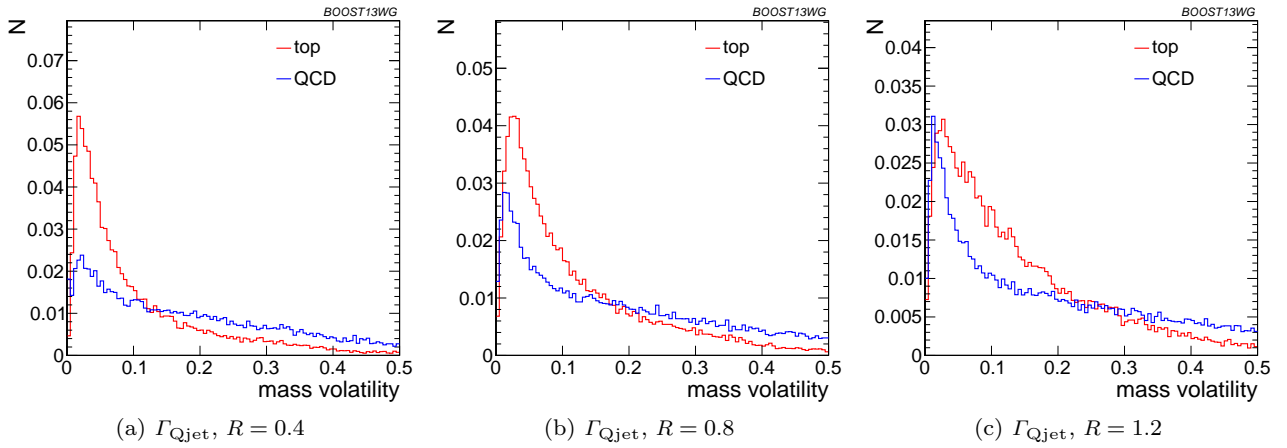


**Fig. 37** Comparison of  $\Gamma_{Qjet}$  in the  $p_T = 1.5 - 1.6$  TeV bin and different values of the anti- $k_T$  radius  $R$ .

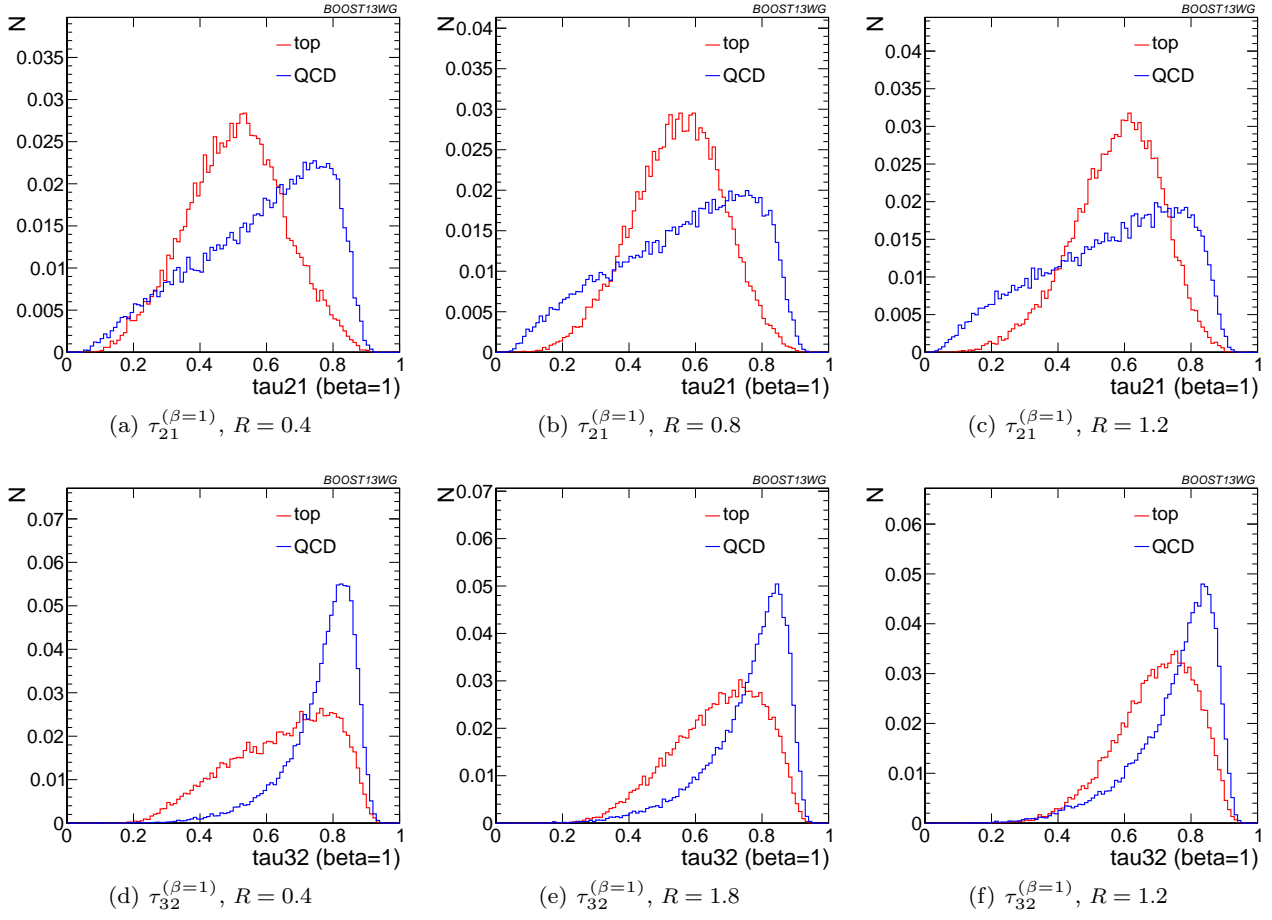


**Fig. 38** Comparison of  $\tau_{21}^{\beta=1}$  and  $\tau_{32}^{\beta=1}$  in the  $p_T = 1.5 - 1.6$  TeV bin and different values of the anti- $k_T$  radius  $R$ .

1047 (Fig. 45), the  $R$ -dependence is identical for all combi-  
 1048 nations. The same holds true for the HEPTopTagger,  
 1049 trimming, and pruning.

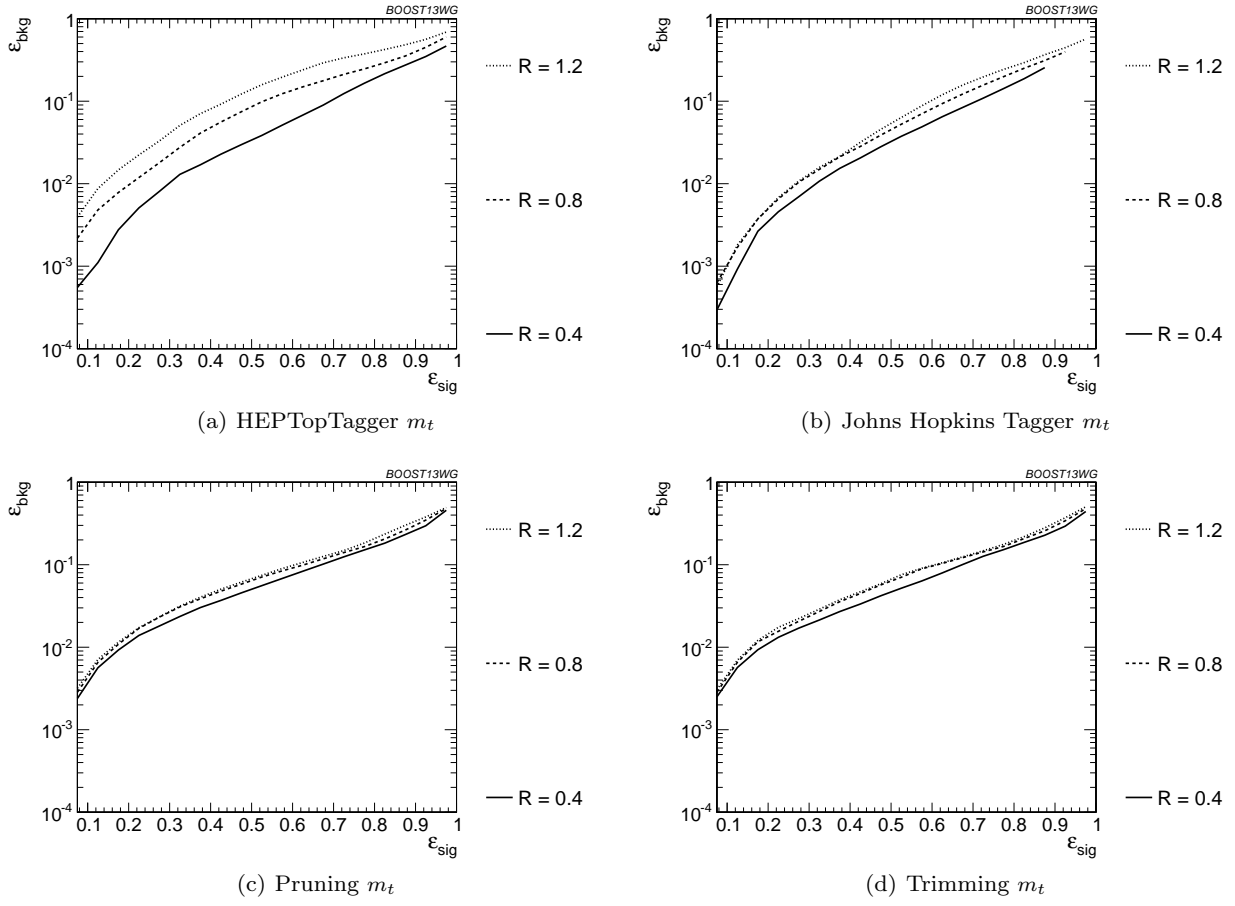


**Fig. 39** Comparison of top mass performance of different taggers at different  $R$  in the  $p_T = 1.5 - 1.6$  TeV bin.

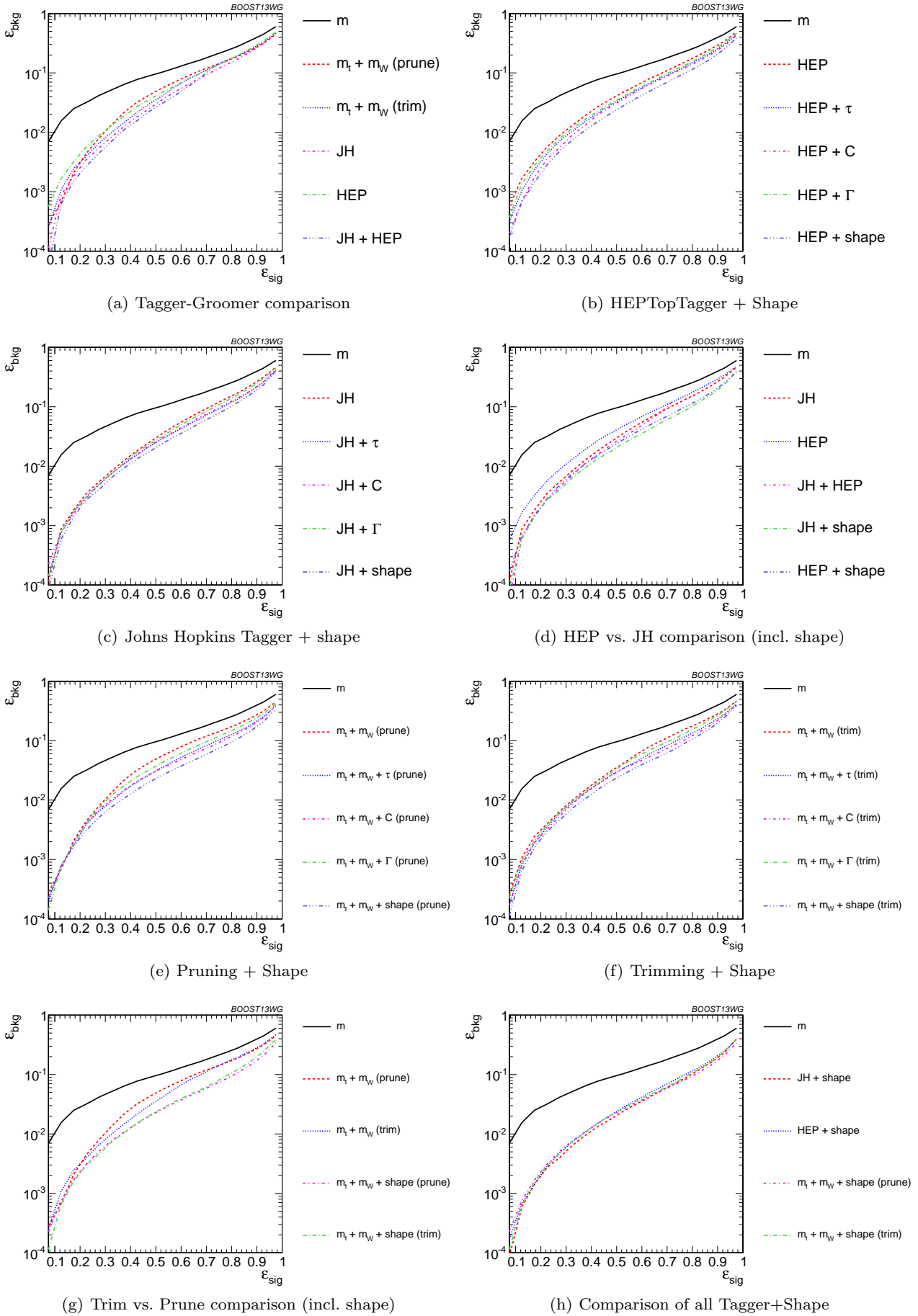


**Fig. 40** The BDT combinations in the  $p_T = 1 - 1.1$  TeV bin using the anti- $k_T$   $R=0.8$  algorithm. Taggers are combined with the following shape observables:  $\tau_{21}^{(\beta=1)} + \tau_{32}^{(\beta=1)}$ ,  $C_2^{(\beta=1)} + C_3^{(\beta=1)}$ ,  $\Gamma_{Qjet}$ , and all of the above (denoted “shape”).



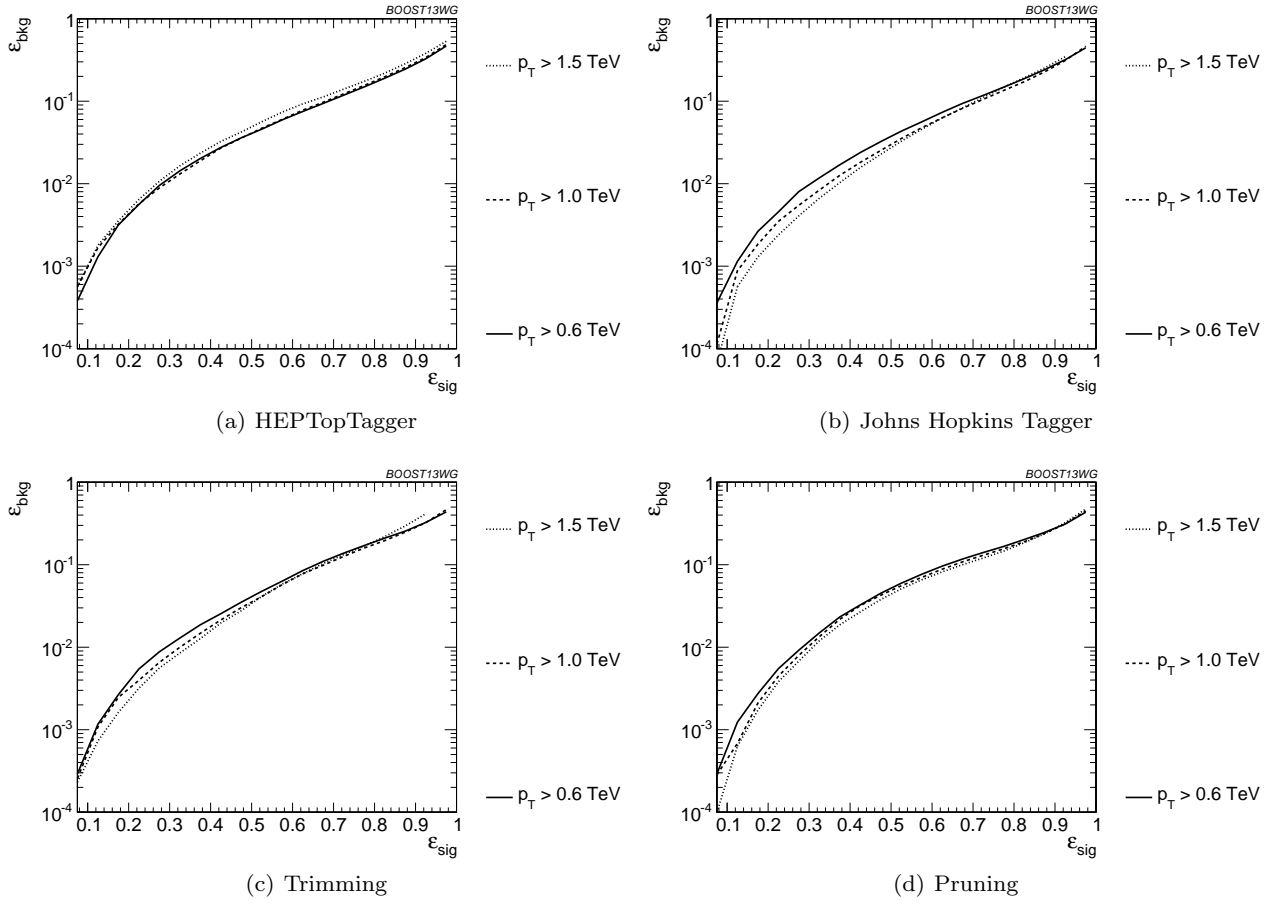


**Fig. 41** Comparison of BDT combination of tagger performance at different  $p_T$  using the anti- $k_T$   $R=0.8$  algorithm.

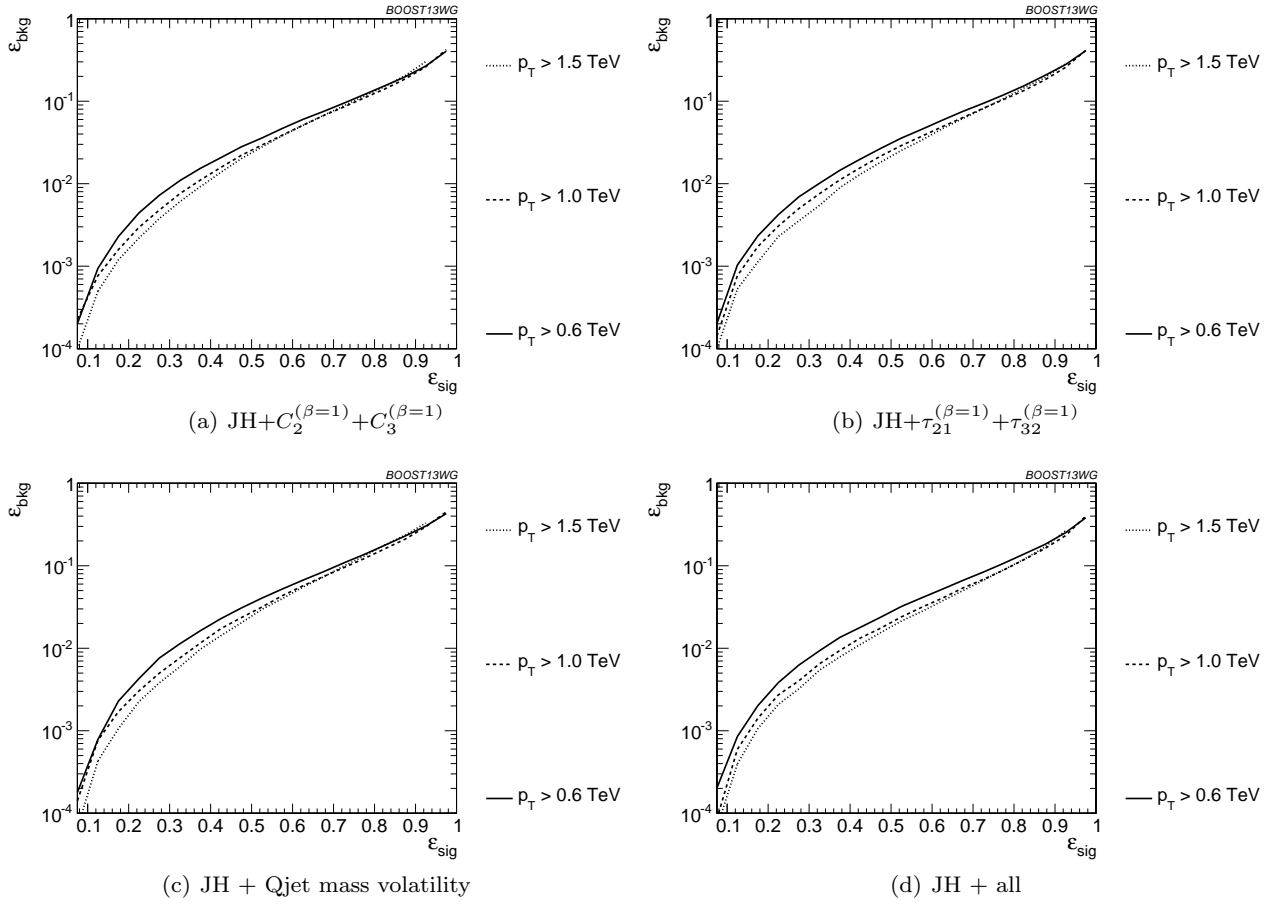


**Fig. 42** Comparison of BDT combination of JH tagger + shape at different  $p_T$  using the anti- $k_T$   $R=0.8$  algorithm.

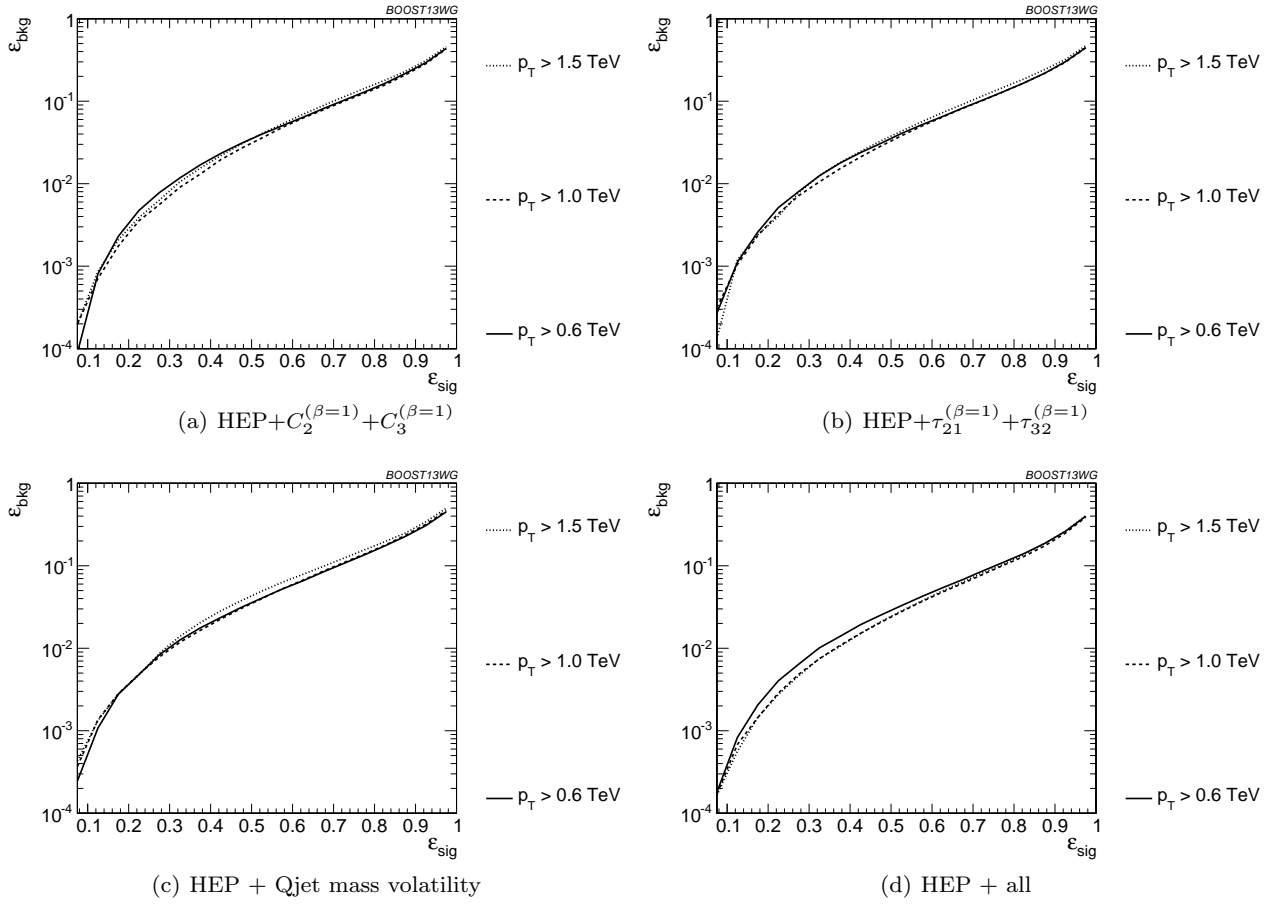


**Fig. 43** Comparison of BDT combination of HEP tagger + shape at different  $p_T$  using the anti- $k_T$   $R=0.8$  algorithm.

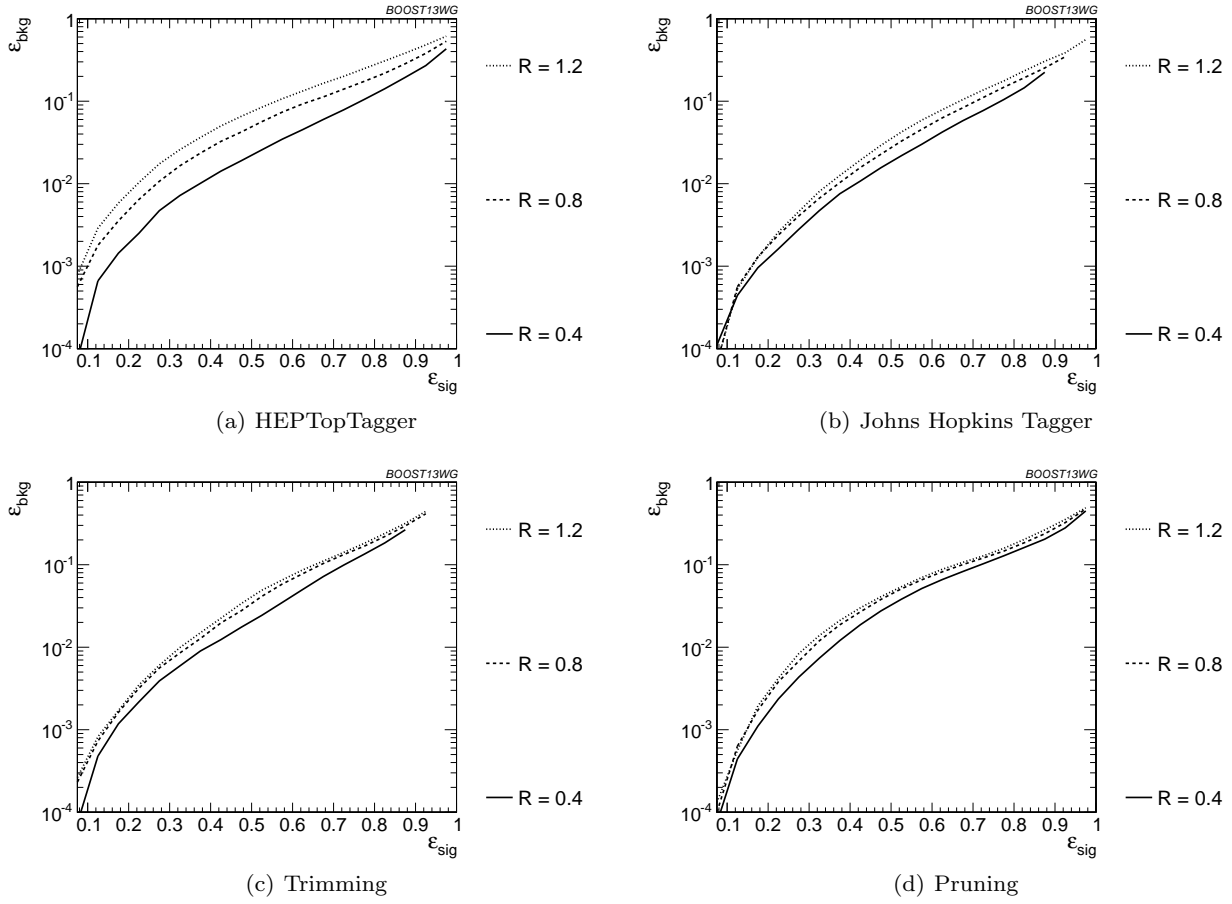


**Fig. 44** Comparison of tagger and jet shape performance at different radius at  $p_T = 1.5\text{-}1.6$  TeV.

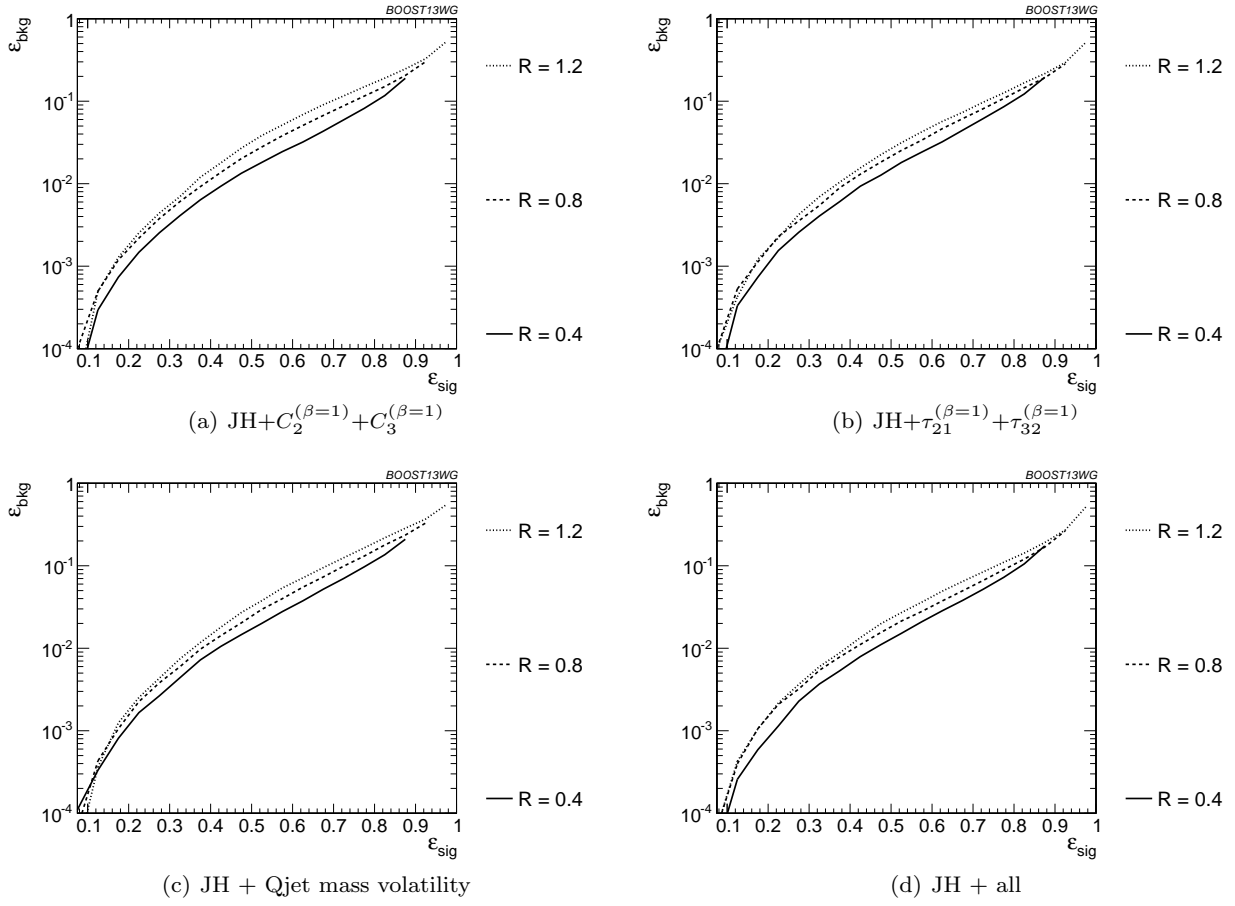


**Fig. 45** Comparison of BDT combination of JH tagger + shape at different radius at  $p_T = 1.5-1.6$  TeV.

## 7.4 Performance at Sub-Optimal Working Points

Up until now, we have re-optimized our tagger and groomer parameters for each  $p_T$ ,  $R$ , and signal efficiency working point. In reality, experiments will choose a finite set of working points to use. How do our results hold up when this is taken into account?

To address this concern, we replicate our analyses, but only optimize the top taggers for a particular  $p_T/R/\text{efficiency}$  and apply the same parameters to other scenarios. This allows us to determine the extent to which re-optimization is necessary to maintain the high signal-background discrimination power seen in the top tagging algorithms we study.

The shape observables typically do not have any input parameters to optimize. Therefore, we focus on the taggers and groomers, and their combination with shape observables, in this section.

**Optimizing at a single  $p_T$  :** We show in Fig. 46 the performance of the top taggers with all input parameters optimized to the  $p_T = 1.5 - 1.6$  TeV relative to the

performance optimized at each  $p_T$ . We see that while the performance degrades by about 50% when the high- $p_T$  optimized points are used at other momenta, this is only an  $O(1)$  adjustment of the tagger performance, with trimming and the Johns Hopkins tagger degrading the most. The jagged behaviour of the points is due to the finite resolution of the scan. We also observe a particular effect associated with using suboptimal taggers: since taggers sometimes fail to return a top candidate, parameters optimized for a particular efficiency  $\varepsilon_S$  at  $p_T = 1.5 - 1.6$  TeV may not return enough signal candidates to reach the same efficiency at a different  $p_T$ . Consequently, no point appears for that  $p_T$  value. This is not often a practical concern, as the largest gains in signal discrimination and significance are for smaller values of  $\varepsilon_S$ , but it is something that must be considered when selecting benchmark tagger parameters and signal efficiencies.

The degradation in performance is more pronounced for the BDT combinations of the full tagger outputs (see Fig. 47), particularly at very low signal efficiency where the optimization picks out a cut on the tail of some distribution that depends precisely on the  $p_T/R$  of the jet. Once again, trimming and the Johns Hopkins tagger degrade more markedly.

Similar behaviour holds for the BDT combinations of taggers + shape observables, although we do not show the plots here because they look similar to Fig. 47.

### Optimizing at a single $R$ :

We perform a similar analysis, optimizing tagger parameters for each signal efficiency at  $R = 1.2$ , and then use the same parameters for smaller  $R$ . We show the ratio of the performance of the top taggers with all input parameters optimized to the  $R = 1.2$  values compared to input parameters optimized separately at each radius, in Fig. 48. While the performance of each observable degrades at small  $\epsilon_{\text{sig}}$  compared to the optimized search, the HEPTopTagger fares the worst as the observed is quite sensitive to the selected value of  $R$ . It is not surprising that a tagger whose top mass reconstruction is susceptible to background-shaping at large  $R$  and  $p_T$  would require a more careful optimization of parameters to obtain the best performance.

The same holds true for the BDT combinations of the full tagger outputs (see Fig. 49). The performance for the sub-optimal taggers is still within an  $O(1)$  factor of the optimized performance, and the HEPTopTagger performs better with the combination of all of its outputs relative to the performance with just  $m_t$ . The same behaviour holds for the BDT combinations of tagger outputs and shape observables.

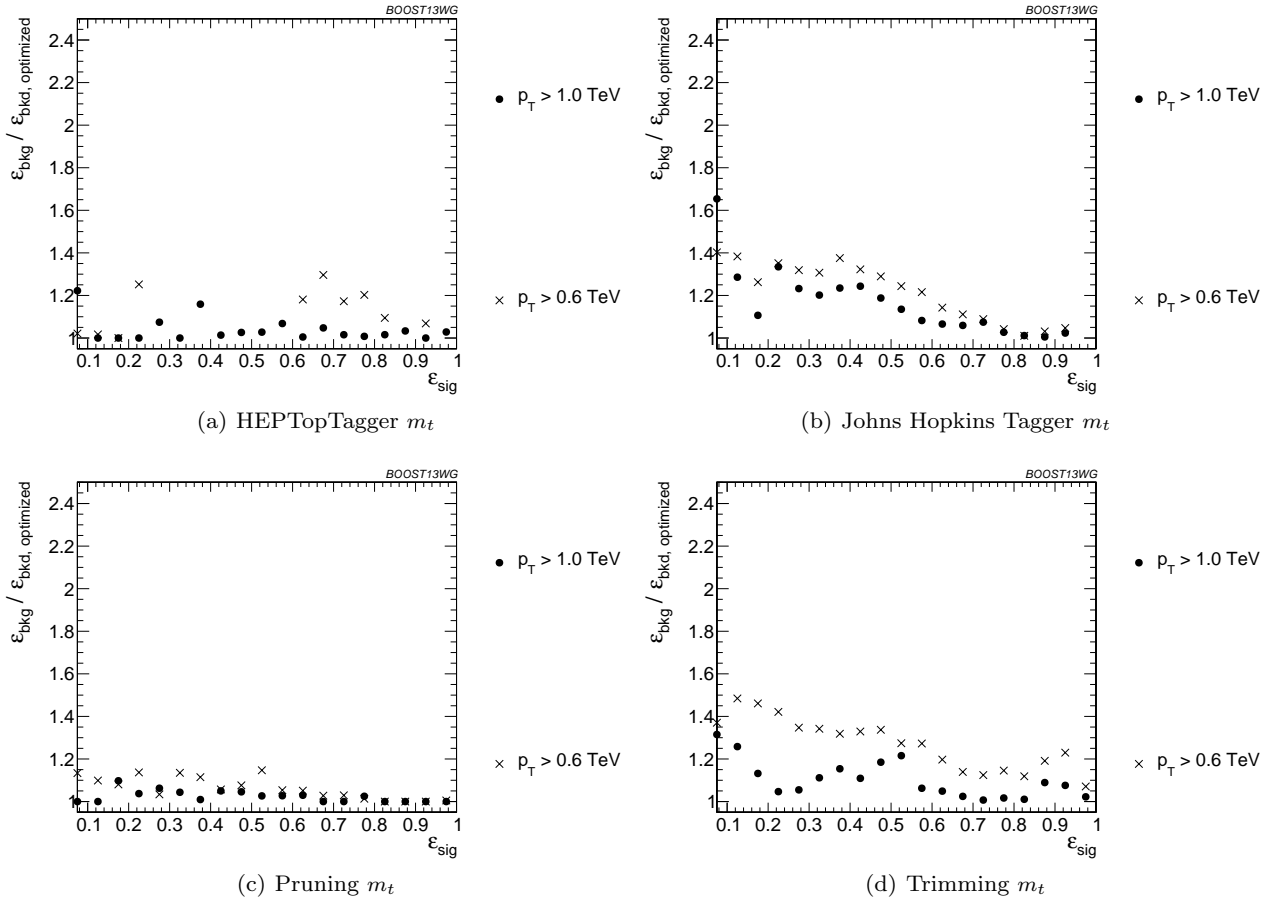


**Fig. 46** Comparison of top mass performance of different taggers at different  $p_T$  using the anti- $k_T$   $R=0.8$  algorithm; the tagger inputs are set to the optimum value for  $p_T = 1.5 - 1.6$  TeV.

### Optimizing at a single efficiency:

The strongest assumption we have made so far is that the taggers can be reoptimized for each signal efficiency point. This is useful for making a direct comparison of different top tagging algorithms, but is not particularly practical for the LHC analyses. We now consider the effects when the tagger inputs are optimized once, in the  $\varepsilon_S = 0.3 - 0.35$  bin, and then used to determine the full ROC curve. We do this at  $p_T = 1 - 1.1$  TeV and with  $R = 0.8$ .

The performance of each tagger, normalized to its performance optimized in each bin, is shown in Fig. 50 for cuts on the top mass and W mass, and in Fig. 51 for BDT combinations of tagger outputs and shape variables. In both plots, it is apparent that optimizing the taggers in the 0.3-0.35 efficiency bin gives comparable performance over efficiencies ranging from 0.2-0.5, although performance degrades at small and large signal efficiencies. Pruning appears to give especially robust signal/background discrimination without re-optimization, possibly due to the fact that there are no absolute

distance or  $p_T$  scales that appear in the algorithm. Figs. 50-51 suggest that, while optimization at all signal efficiencies is a useful tool for comparing different algorithms, it is not crucial to achieve good top-tagging performance in experiments.

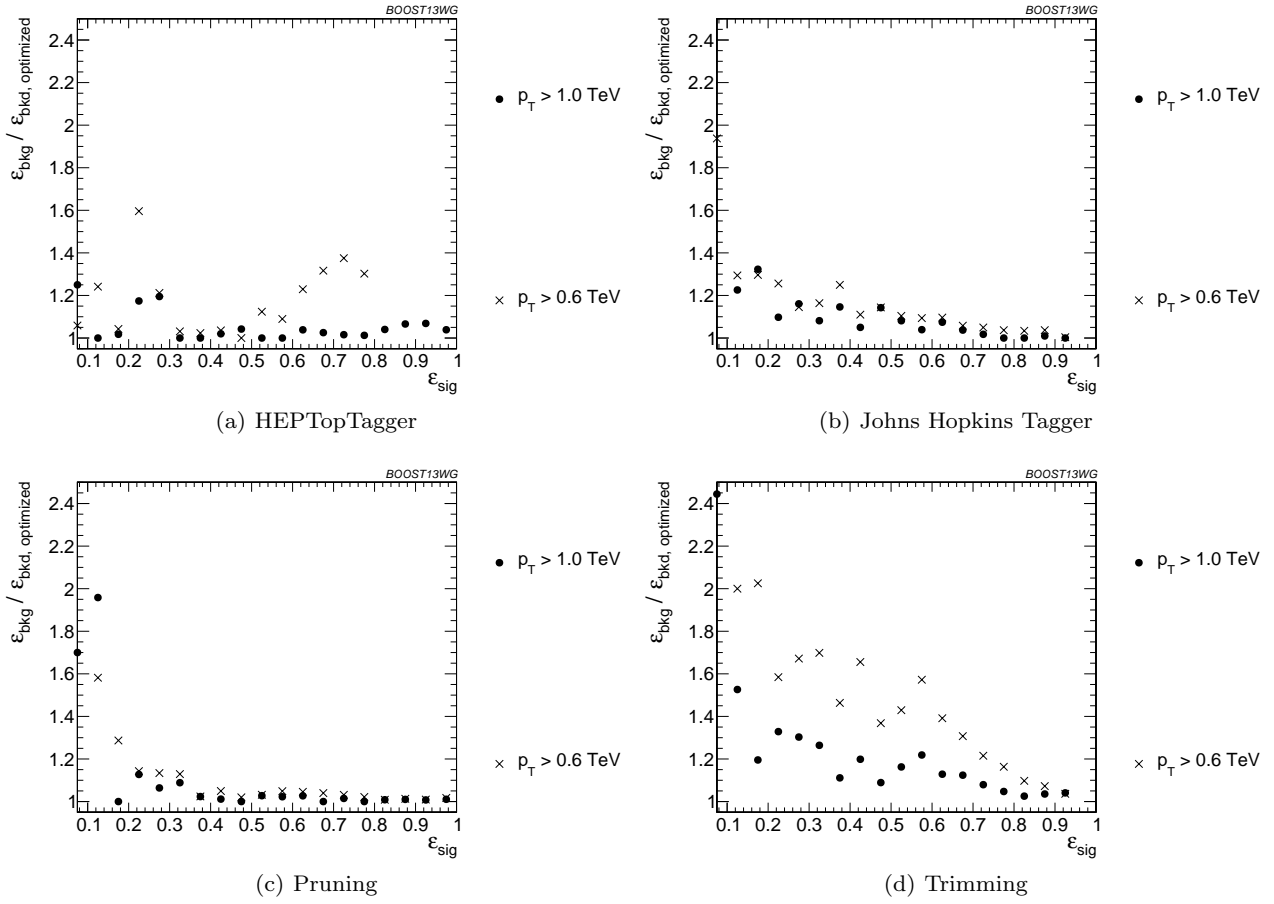


**Fig. 47** Comparison of BDT combination of tagger performance at different  $p_T$  using the anti- $k_T$   $R=0.8$  algorithm; the tagger inputs are set to the optimum value for  $p_T = 1.5 - 1.6$  TeV.



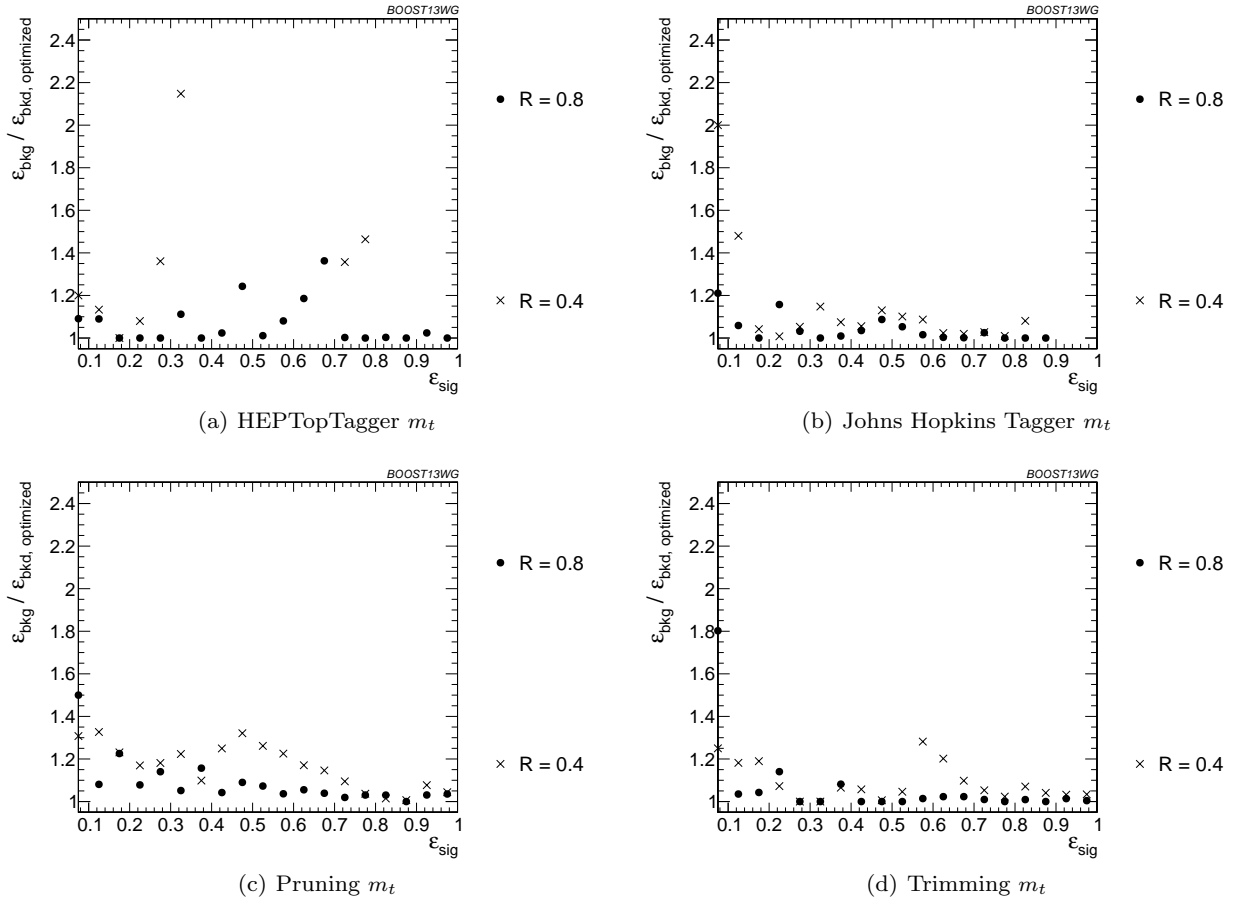


**Fig. 48** Comparison of top mass performance of different taggers at different  $R$  in the  $p_T = 1500 - 1600$  GeV bin; the tagger inputs are set to the optimum value for  $R = 1.2$ .

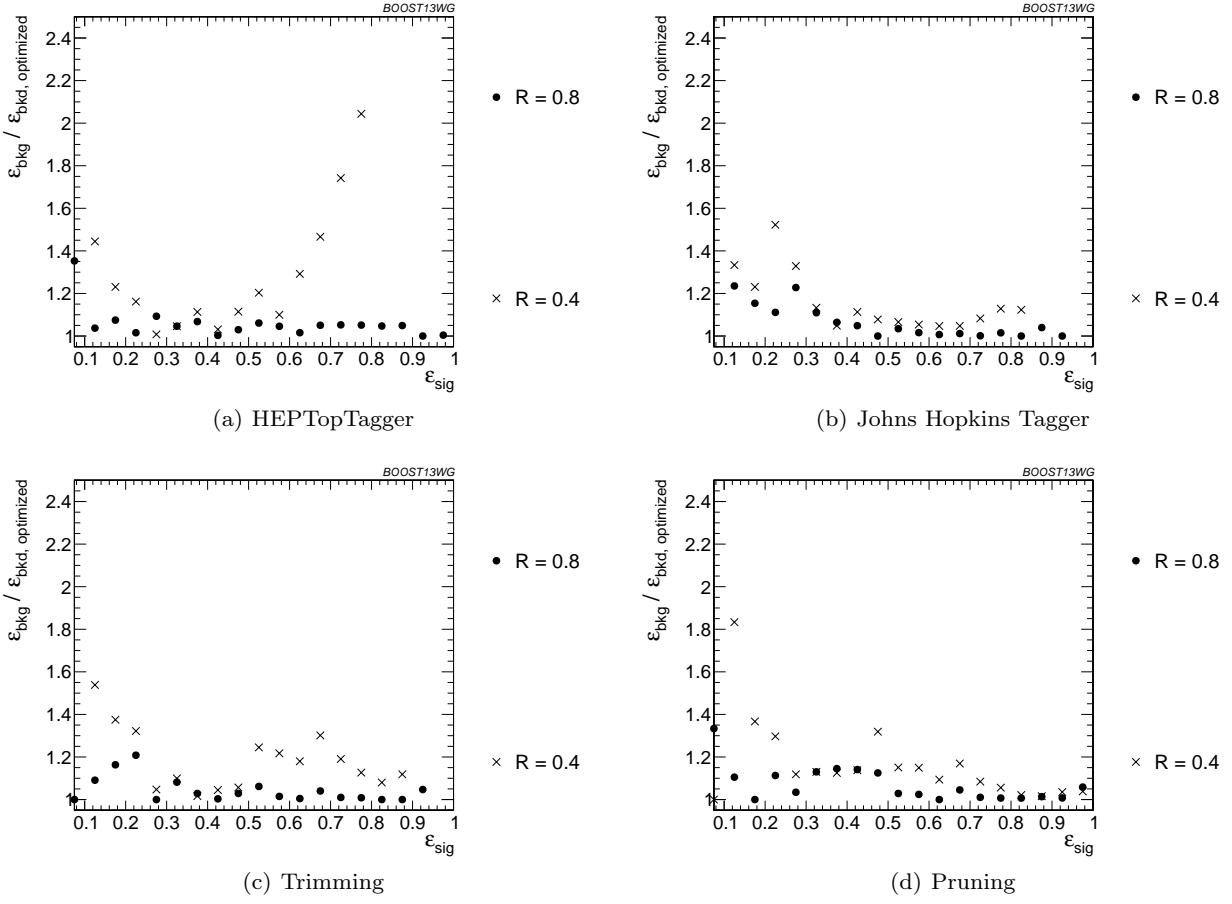


**Fig. 49** Comparison of tagger and jet shape performance at different radius at  $p_T = 1.5-1.6$  TeV; the tagger inputs are set to the optimum value for  $R = 1.2$ .

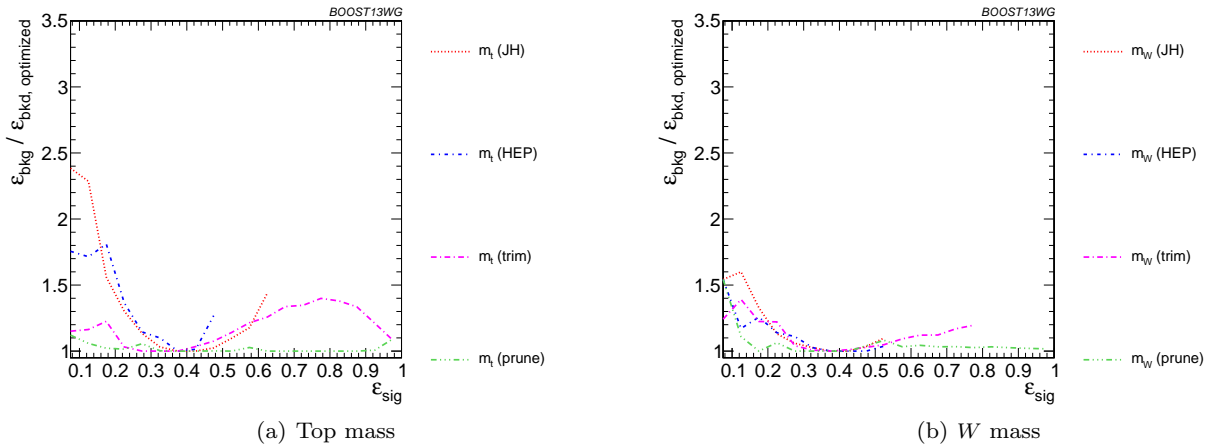


**Fig. 50** Comparison of single-variable top-tagging performance in the  $p_T = 1-1.1$  GeV bin using the anti- $k_T$ ,  $R=0.8$  algorithm; the inputs for each tagger are optimized for the  $\epsilon_{\text{sig}} = 0.3 - 0.35$  bin.

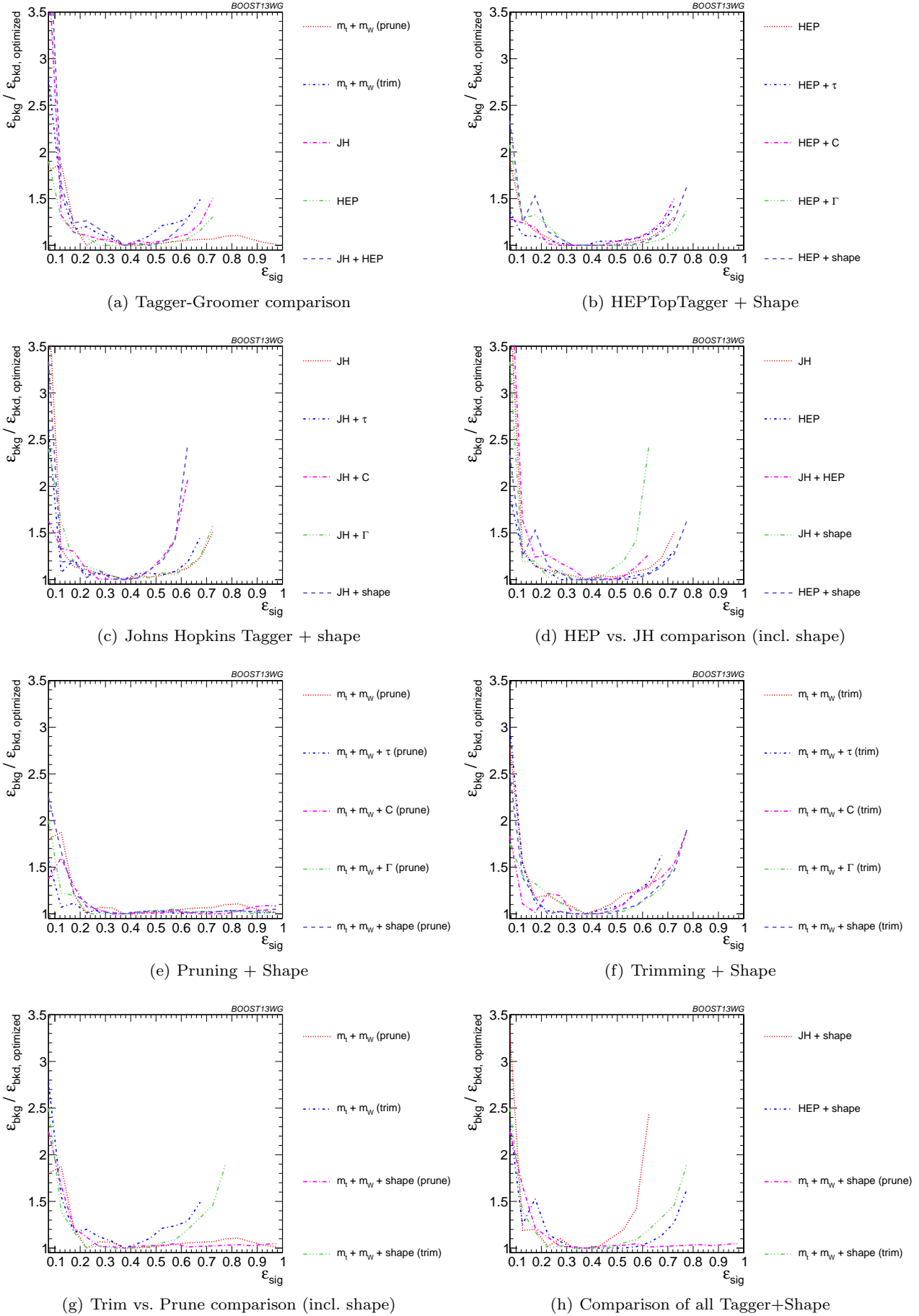


**Fig. 51** The BDT combinations in the  $p_T = 1 - 1.1$  TeV bin using the anti- $k_T$   $R=0.8$  algorithm. Taggers are combined with the following shape observables:  $\tau_{21}^{(\beta=1)} + \tau_{32}^{(\beta=1)}$ ,  $C_2^{(\beta=1)} + C_3^{(\beta=1)}$ ,  $\Gamma_{Qjet}$ , and all of the above (denoted “shape”). The inputs for each tagger are optimized for the  $\epsilon_{sig} = 0.3 - 0.35$  bin.

## 8 Summary & Conclusions

This report discussed the correlations between observables and looked forward to jet substructure at Run II of the LHC at 14 TeV center-of-mass collisions energies.

## References

1. A. Abdesselam, E. B. Kuutmann, U. Bitenc, G. Brooijmans, J. Butterworth, et al., *Boosted objects: A Probe of beyond the Standard Model physics*, *Eur.Phys.J. C* **71** (2011) 1661, [[arXiv:1012.5412](#)].
2. A. Altheimer, S. Arora, L. Asquith, G. Brooijmans, J. Butterworth, et al., *Jet Substructure at the Tevatron and LHC: New results, new tools, new benchmarks*, *J.Phys. G* **39** (2012) 063001, [[arXiv:1201.0008](#)].
3. A. Altheimer, A. Arce, L. Asquith, J. Backus Mayes, E. Bergeas Kuutmann, et al., *Boosted objects and jet substructure at the LHC*, [arXiv:1311.2708](#).
4. A. Hoecker, P. Speckmayer, J. Stelzer, J. Therhaag, E. von Toerne, and H. Voss, *TMVA: Toolkit for Multivariate Data Analysis*, *PoS ACAT* (2007) 040, [[physics/0703039](#)].
5. C. Anders, C. Bernaciak, G. Kasieczka, T. Plehn, and T. Schell, *Benchmarking an Even Better HEPTopTagger*, *Phys.Rev. D* **89** (2014) 074047, [[arXiv:1312.1504](#)].

## Acknowledgements

We thank the Department of Physics at the University of Arizona and for hosting the conference at the Little America Hotel. We also thank Harvard University for hosting the event samples used in this report. This work was made possible in part by the facilities of the Shared Hierarchical Academic Research Computing Network (SHARCNET) and Compute/Calcul Canada. We also thank Hallie Bolonkin for the BOOST2013 poster design and Jackson Boelts' ART465 class (fall 2012) at the University of Arizona School of Arts VisCom program. (NEED TO ASK PETER LOCH FOR MORE ACKNOWLEDGEMENTS)